DISSIPATION AND DYNAMICS IN QUANTUM MANY-BODY SYSTEMS

By

Brent Wendolyn Barker

A DISSERTATION

Submitted to
Michigan State University
in partial fulfillment of the requirements
for the degree of

Physics—Doctor of Philosophy

2014

ABSTRACT

DISSIPATION AND DYNAMICS IN QUANTUM MANY-BODY SYSTEMS

By

Brent Wendolyn Barker

In this thesis, we simulate the time evolution of quantum many-body systems and use comparisons to experimental data in order to learn more about the properties of nuclear matter and understand better the dynamical processes in central nuclear collisions. We further advance the development of a nonequilibrium Green's function description of both central nuclear collisions and Bose-Einstein Condensates.

First in the thesis, we determine the viscosity of nuclear matter by adjusting the in-medium nucleon-nucleon cross section in our BUU transport model until the simulation results match experimental data on nuclear stopping in central nuclear collisions at intermediate energies. Then we use that cross section to calculate the viscosity self-consistently. We also calculate the ratio of shear viscosity to entropy density to determine how close the system is to the proposed universal quantum lower limit.

Next, we use the same BUU transport model to isolate the protons emitted early in a central nuclear collision at intermediate energy, as predicted in the model, using a filter on high transverse momentum, and we show the effect on the source function. We predict a recontraction of protons at late times in the central collision of ^{112}Sn $+^{112}$Sn at $50\,\mathrm{MeV/nucleon}$ that results in a resurgence of emission of protons and show how to use the transverse momentum filter and the source function to test this prediction in experiment.

Next, we develop an early implementation of a more fully quantal transport model than the BUU equations, with our sights set on solving central nuclear collisions in 3D using

nonequilibrium Green's functions. In our 1D, mean field, density matrix model, we demonstrate the initial state preparation and collision of 1D nuclear "slabs". With the aim of reducing the computational cost of the calculation, we show that we can neglect far off-diagonal elements in the density matrix without affecting the one-body observables.

Further, we describe a method of recasting the density matrix in a rotated coordinate system, enabling us to not only ignore the irrelevant matrix elements in the time evolution, but also avoid computing them completely, reducing the computational cost. As an added benefit, we find that the rotation allows us to partially decouple the position and momentum discretization, permitting access to arbitrary regimes of kinetic energy without altering the resolution and range of the 1D box in position space.

Finally, we exhibited the wide applicability of this density matrix approach by applying it to a system of 2000 ultracold ^{87}Rb atoms in a Bose-Einstein condensate, as described by the Gross-Pitaevskii equation, successfully acheiving a stable state in a harmonic oscillator trap.

Dedicated to my parents, Arlene and Phil. Without their encouragement from a young age, I would never have come so far.

ACKNOWLEDGMENTS

There have been so many with whom I shared part of this journey, and who have been instrumental in one part or another of my joy, fulfillment, and success during my time at MSU. I can only hope to thank a small fraction of them, and even then, the list will inevitably be biased towards those who have influenced me more recently. That said, I'd like to acknowledge at least these folks:

- My advisor, Pawel Danielewicz, whose patience is as legendary as his insight, and whose availability is exceedingly convenient, allowing for swift collaboration, even while he spends half of his time on the other side of the world.

- Professional mentors: Brian O'Shea for our discussions about teaching and physics education research. Morten Hjorth-Jensen, for his eternal optimism, compassion, and humility. Filomena Nunes, for assisting with time management skills.

- My longterm officemate family Jun Hong and Ngoc Bic Nguyen, for providing a supportive environment in which to work. In particular, I want to thank Jun for her unyielding, compassionate support and encouragement during our daily meetings, and Bic for our walks and long and fruitful discussions.

- Micha Kilburn, a mentor and friend.

- My found family: Matt DeNinno, Sofia Maystrenko, and Katie Thompson. We've grown so much together, and they've helped to keep me sane and grounded in my durance, and have been absolutely vital to my continued success.

TABLE OF CONTENTS

LIST OF TABLES

LIST OF FIGURES

Chapter 1

Introduction

Central collisions between heavy nuclei are complex phenomena that involve many different types of processes. These collisions are a means to learn about properties of high density, hot, strongly interacting matter. The learning is contingent on proper modelling of the collisions. The proper modelling is difficult because of the simultaneous effects of different processes. Most often, it involves semiclassical approaches, and methods are often sourced from other fields. In this work, we attempt to progress in several different directions in understanding and modelling of the collisions.

To solve the full time-dependent, N-body wavefunction for the motion of $N \gtrsim 30$ particles interacting quantally would take far more time and resources than the world's current computing facilities have available. Instead, we use approximations. The quest, then, of quantum many-body physics is to find those approximations that preserve enough of the physics to give accurate predictions, and to use intuition and persistent random walks of investigation to guide us to those approximations.

For central nuclear collisions, there are generally 2 approaches, microscopic and macroscopic. Macroscopically, the system can be modeled hydrodynamically, with the equation of state and transport coefficients, like viscosity and heat conduction, as inputs to the calculation that determine how the matter interacts as it evolves forward in time. However, the hydrodynamic approximation is strictly valid only when the particle mean free path is much smaller than the size of the system. In nuclear systems, though, the mean free path

is comparable to the size of the system, and the hydrodynamic limit is not strictly valid. Calculations have been performed using hydrodynamic models, and they do provide a coarse description of the dynamics, but they do not provide as accurate a description as microscopic models.

In the microscopic approach, the particles are modelled individually, and their interaction with each other determines the dynamics. For example, in the Boltmann-Uehling-Uhlenbeck (BUU) model, particles move in classical trajectories under the influence of a mean field potential, and they undergo binary collisions with each other. The scattering cross sections and mean field have parameters that are fit to experimental data, so these sorts of approaches are phenomenological. From this formalism, we can still derive, within the model, the macroscopic quantities used as inputs for hydrodynamics. In particular, in Chapter 2, we determine the viscosity of nuclear matter by adjusting the in-medium nucleon-nucleon cross section within a BUU model until the simulations match data from nuclear stopping, which is a good observable of how quickly momentum is transferred across the system, and, hence, the viscosity.

As a macroscopic quantity, viscosity is defined for a bulk system, not for individual particles. In particular, viscosity becomes useful for describing a system when there are many particles interacting repeatedly in a small space. In nuclear collisions, this occurs early in the collision, as the nuclei interpenetrate and mix with each other. To learn about the evolution of the collision as particles spread out and start acting more like a gas than a liquid, we must use other, microscopically-based methods. As the particles leave the high density overlap region, if they are traveling close enough to each other, they attract or repel each other, forming a correlation (or anti-correlation) between the momenta of those particles. We use that correlation signature to learn about the shape of the particle emission region

in Chapter 3. Further, we use the shape of the resulting function, called a source function, and compare it with the detailed dynamics in our microscopic model, to distinguish between qualitatively different dynamics at late times in the collision. This gives us a closer look into the actual timescale of these femtosecond processes.

The simulation mentioned in the previous few paragraphs, the BUU model, is semi-classical in nature. Since most nuclear collision simulations are semi-classical, it is difficult to determine the validity of the approximation. In Chapter 4, we introduce the first steps of an implementation of a fully quantal time evolution model for nuclear collisions, and we show how we can smoothly approach the classical limit of the theory and explore the effect on the dynamics. What's more, since fully quantal approaches have a much greater computational cost, in both time and storage, we demonstrate how to exploit the semi-classical nature of the physical system to reduce that cost.

Finally, towards the end of Chapter 4, we use this new implementation to also describe a 1D Bose-Einstein Condensate, a system of particles, in our case a gas of ultracold atoms, all in the same, lowest energy state, and discuss some stability constraints and issues. Thus, our model describes quantum phenomena across an energy range from GeV to neV.

1.1 Dynamics of central collisions

In a central ($b_\text{red} \lesssim 0.3$) collision[1] between heavy nuclei (A $\gtrsim$ 10) at intermediate energy ($E_\text{beam} \approx 50\text{--}2000\,\text{MeV/nucleon}$), the two nuclei approach each other and interpenetrate, forming a hot, dense region in the middle. The part of each nuclei whose cross-sectional

---

[1]The centers of the nuclei are offset by a displacement b, called the impact parameter, illustrated in Fig. 1.1. For comparison across different collision system sizes, we use a reduced impact parameter, $b_\text{red} \equiv b/b_\text{max}$, where b_max is the sum of the radii of the colliding nuclei.

area does not overlap with the other nucleus continues forward and is called the "specta-tor", shearing off from the "participant" region[2]. As the participant region compresses, the nucleons that comprise it interact repeatedly, partially equilibrating. Then, after enough longitudinal kinetic energy of the projectile is converted into internal degrees of freedom (tending to randomize the velocities of the particles inside), it then expands, emitting parti-cles and fragments. Those fragments and the spectators continue through freeze-out, when they no longer interact with other particles. Then, if they are excited, they still will decay or "evaporate", emitting other particles.

Emission from nucleus-nucleus collisions is generally divided into two regimes. The first is emission from the center of the collision very early in the time evolution, before the par-ticipant nucleons equilibrate. This is called nonequilibrium, pre-equilibrium, or dynamical emission in the literature. The second regime is after the equilibrium, where emission occurs as a result of decay of excited states. This is generally called slow, equilibrium, or evapo-rative emission. Since the entire collision event happens in $\sim 100\,\mathrm{fm}/c$ ($1\,\mathrm{fm}/c \sim 10^{-23}\,\mathrm{s}$), while the typical time resolution in experiment is $\sim 1\,\mathrm{ns}$, all particles from the event are perceived to be detected simultaneously, mixing emission from both fast and slow processes. Discerning fast versus slow decay requires comparison with a time-dependent theory, to see which experimental observables will select for a particular time or shape of emission. We implement a method for this in Chapter 3.

---

[2]For collisions with $E_{\mathrm{beam}} \gtrsim 50\,\mathrm{MeV/nucleon}$, the energy it takes to separate the pe-ripheral, spectator nucleons from the interpenetrating ones (less than the binding energy per nucleon, $8\,\mathrm{MeV}$) is less than the kinetic energy of each nucleon in the local rest frame. As a result, the spectator nucleons' trajectories are not very affected by the collision.
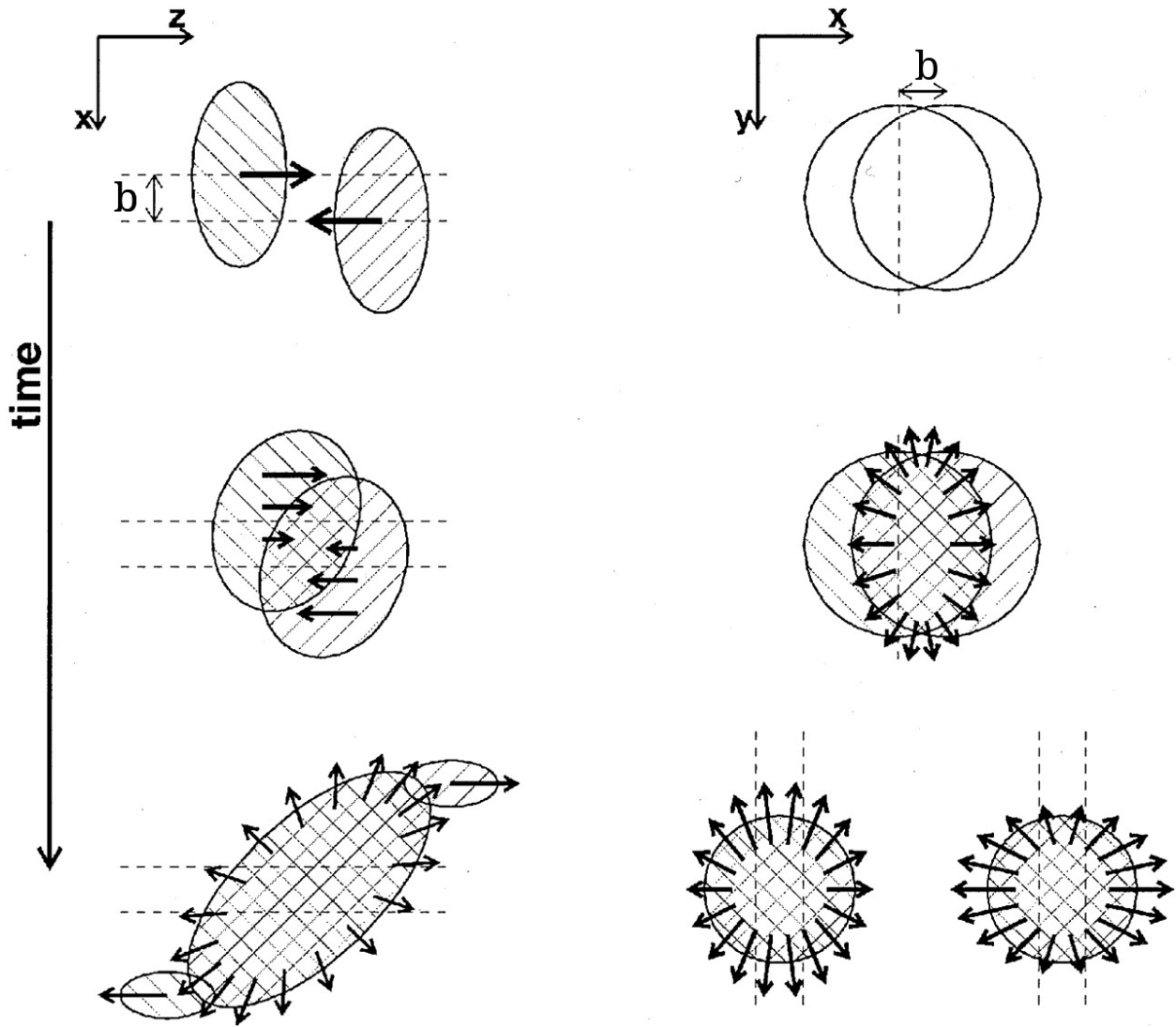
Figure 1.1: Stages of an intermediate-energy nuclear collision. From top to bottom: approach, compression, expansion (figure from Ref. [1]).

1.2 Boltmann-Uehling-Uhlenbeck equation

To describe central nuclear reactions, we use the Boltzmann-Uehling-Uhlenbeck (BUU) set of equations, describing the motion of a Wigner quasi-probability distribution in phase space, $f_1 \equiv (\mathbf{r}, \mathbf{p}_1, t)$:

$$\frac{\partial f_1}{\partial t} + \frac{\partial \epsilon_{\mathbf{p}_1}}{\partial \mathbf{p}_1} \frac{\partial f_1}{\partial \mathbf{r}} - \frac{\partial \epsilon_{\mathbf{p}_1}}{\partial \mathbf{r}} \frac{\partial f_1}{\partial \mathbf{p}_1} = \int \mathrm{d}\mathbf{p}_2 \, \mathrm{d}\Omega \, v_{12} \frac{\mathrm{d}\sigma}{\mathrm{d}\Omega} \left(\tilde{f}_1 \tilde{f}_2 f_{1'} f_{2'} - \tilde{f}_{1'} \tilde{f}_{2'} f_1 f_2 \right), \qquad (1.1)$$

where the subscript 1 is used only to avoid confusion with the other momenta under the integral.

This equation starts with the single-particle Liouville equation on the l.h.s., describing the single-particle evolution of a phase space density in a mean field. For clarity, note that $\frac{\partial \epsilon_{\mathbf{p}_1}}{\partial \mathbf{p}_1}$ is the single-particle velocity, and $\frac{\partial \epsilon_{\mathbf{p}_1}}{\partial \mathbf{r}}$ is the force due to the mean field. The r.h.s. takes into account the effect of binary collisions. The first term on the right describes particles with $\mathbf{p}_{1'}$ and $\mathbf{p}_{2'}$ scattering into particles with $\mathbf{p}$ and $\mathbf{p}_2$, thus increasing the occupancy of f (gain). The second term describes, correspondingly, a decrease in the occupancy f. Here, $\tilde{f}_a \equiv 1 - f_a$ represents the Pauli principle blocking scattering into the final state $\mathbf{p}_a$. The rate of scattering is governed by the NN cross section σ (here, a function of $\mathbf{p}_1$, $\mathbf{p}_2$, and Ω, the angle between the relative momenta before and after the collision). It is this cross section that is modified by in-medium effects in Section 2.1.

In Chapters 2 and 3, an implementation of a time-dependent solution to this equation by Danielewicz and collaborators [8–13] is used to describe nuclear collisions. In this implementation, for each nucleon, $\tilde{N}$ test particles are created in the simulation and tracked as particles. They move in classical trajectories under the influence of the mean field and encounter random binary collisions with other test particles that are close to them in position

space. With an increase of test particle number, the simulation converges on a more average, stable solution.

1.2.1 Impact parameter comparison

Throughout this work, we will be comparing our simulation results to experimental data. In experiment, a range of impact parameters is selected for analysis. In the transport simulation, the initial state is prepared with one specific impact parameter. To save computation time, an effective impact parameter, b_{eff}, is chosen that represents the average cross-section for the impact parameter range. For a given b_{min} and b_{max}, the effective impact parameter b_{eff} is given by

$$\pi b_{\text{eff}}^2 = \frac{\pi b_{\text{min}}^2 + \pi b_{\text{max}}^2}{2}$$

$$b_{\text{eff}} = \sqrt{\frac{1}{2}\left(b_{\text{min}}^2 + b_{\text{max}}^2\right)}$$

(1.2)

For studies of central collisions, often experimental ranges set $b_{\text{min}} = 0$, so $b_{\text{eff}} = b_{\text{max}}/\sqrt{2}$. This single impact parameter is used in many simulations.

Chapter 2

Dissipation

In this chapter, we focus on studying the transport of momentum through the equilibrated region, quantified by the shear viscosity, in order to learn more about the fundamental properties of nuclear matter.

Knowledge of the shear viscosity is important for understanding the stability of rotating neutron stars, the formation of black holes, and the evolution of supernovae. Additionally, there have been conjectures regarding a fundamental quantum lower limit on the ratio of shear viscosity to entropy density (η/s) in a substance [14], thought to be approached in the quark-gluon plasma and accessed in relativistic heavy ion collisions. The question remains as to whether quark degrees of freedom are needed to approach such a limit. We will be able to make a quantitative assessment of how close nuclear matter is to this "perfect liquid".

Many groups have used giant resonances to determine the viscosity of nuclear matter (see references in [15]). Several groups have studied the η/s ratio for nuclear collisions at intermediate energies using different models, including statistical multifragmentation [16] and quantum molecular dynamics (QMD) [17]. However, the group using QMD calculates viscosity using an approach that is valid strictly within BUU transport models, and neither group tunes their calculation to specifically reproduce observables directly related to viscosity.

In the present work, we use stopping, a phenomenom that is a measure of the degree to which the projectile nucleus transfers momentum to the target, to constrain the in-medium nucleon-nucleon cross section in a BUU transport model. We then use this

(model-dependent) cross section to calculate the viscosity of nuclear matter according to this same BUU model, thus determining this model-independent quantity in a consistent manner. Different cross section reductions can give the same amount of stopping, so we also test whether viscosity is, in fact, a quantity that matters for stopping, or whether the in-medium cross section matters while the viscosity is not as correlated with the stopping data.

Several groups (e.g. [18]) treat the in-medium cross section as half the free cross section [19], which gives approximately the same cross section reduction as effective mass scaling [20–22]. Gaitanos notes that this resolves some discrepancies with experimental data, but widens other differences. In the current work, we investigate in-medium cross section reductions that are dependent on density and/or energy.

2.1   The NN cross section in the nuclear medium

Looking ahead, it is clear that using the nucleon-nucleon (NN) cross section in the BUU equation (Eq. 1.2) overestimates the amount of stopping found in central collisions at intermediate energy. In this document, 3 approaches are explored. In practice, it is found that the NN cross section is reduced in the medium. For use in the BUU simulation, the in-medium NN cross section is applied as a reduced probability of each NN collision to occur. Thus, each reduced cross section is presented as a reduction factor multiplied by the free cross section.

2.1.1 Tempered

In the Tempered cross section reduction scheme [23], a limiting approach is considered. It assumes that some reduction happens as the local nucleon density, n, increases, and in the limit of high density, the resulting cross section radius should not exceed the interparticle distance. So the resulting cross section σ should follow

$$\sigma \lesssim \sigma_0 = \nu n^{-2/3}. \tag{2.1}$$

As this is a very schematic view, a tunable parameter $\nu \sim 1$ is used. Practically, to smoothly approach this limit, the following equation is used:

$$\sigma = \sigma_0 \tanh\left(\frac{\sigma_{\text{free}}}{\sigma_0}\right), \tag{2.2}$$

where σ_0 is defined in Eq. 2.1 (in principle, other smoothing functions could be used).

2.1.2 Rostock

The Rostock in-medium cross section, developed at Universität Rostock [24], was found using a thermodynamic T-matrix approach. In their calculation, the reduction was due to Pauli blocking and self-energy effects [25]. To capture the essence of it without reproducing the entire method, the resulting reduction is crudely parameterized, independent of isospin:

$$\sigma = \sigma_{\text{free}} \exp\left(-0.6 \frac{\rho/\rho_0}{1 + \left(\frac{T_{\text{c.m.}}}{150\,\text{MeV}}\right)^2}\right), \tag{2.3}$$

where $T_{\text{c.m.}}$ is the total kinetic energy of the two interacting particles, in the frame where the local medium is at rest. The Rostock cross section was derived assuming that the total momentum of the particles is zero, and the velocity of the local medium is also zero, to simplify the calculations. The cross section is used here in cases where, in the rest frame of the local medium, the total momentum of the particles is not zero.

2.1.3 Fuchs

Another group [26] notes that in the BUU equation (Eq. 1.2), the in-medium mean field that the matter is subject to on the l.h.s. should be derived consistent with the in-medium NN cross section σ used in the collision integral in the r.h.s. The basis for both of these alterations is the in-medium Dirac-Brueckner T-matrix. This cross section reduction is parameterized here:

$$\sigma_{\text{nn}} = \sigma_{\text{nn,free}} \exp\left(-1.7\frac{\rho/\rho_0}{1 + \left(\dfrac{T_{\text{c.m.}}}{12\,\text{MeV}}\right)^{3/2}}\right) \tag{2.4}$$

$$\sigma_{\text{np}} = \sigma_{\text{np,free}} \exp\left(-1.4\frac{\rho/\rho_0}{1 + \dfrac{T_{\text{c.m.}}}{33\,\text{MeV}}}\right). \tag{2.5}$$

Like the Rostock reduction, this cross section was derived for two particles with total momentum equal to zero in the rest frame of the local medium. Again, it is assumed that this can be applied to the case where the total momentum is not equal to zero.

2.2 Stopping observables

2.2.1 Linear momentum transfer

In a mass-asymmetric collision of a light projectile colliding with a heavy target, one can determine the amount of momentum per nucleon that is transferred to the target. As in the schematic in Fig. 2.1, one finds the momentum of the largest fragment emitted by the collision. Because of the high mass, that fragment is assumed to stem from the target (the "target-like residue"). The higher its momentum, the more momentum was transferred from the projectile. This corresponds to a higher degree of stopping. To compare the observable across reaction systems, this momentum is divided by the momentum of the center of mass. Since the velocities involved are non-relativistic, they can be used directly to find the linear momentum transfer (LMT). This observable was originally used to distinguish between direct and compound fission reactions in heavy nuclei [27, 28], then used more generally in nucleus-nucleus collisions [29]. The technique relies on a clear determination of the target-like fragment, and as the beam energy increases, there are more violent collisions and the largest fragment produced becomes smaller. Therefore, the practical energy range for this observable is from around the Coulomb barrier to around $150\,\mathrm{MeV/nucleon}$ or so. The observable LMT is defined as

$$\mathrm{LMT} = \left\langle \frac{v_\parallel}{v_\mathrm{c.m.}} \right\rangle, \tag{2.6}$$

where $v_\parallel$ is the velocity of the target-like residue in the beam direction, $v_\mathrm{c.m.}$ is the velocity of the reaction center of mass. A higher LMT corresponds to a higher degree of stopping.

Results of LMT for $^{40}\mathrm{Ar} + \mathrm{Cu}$, $+\mathrm{Ag}$, and $+\mathrm{Au}$ are shown in Figs. 2.2, 2.3, and 2.4, respectively. The experimental data was collected using the K1200 cyclotron at Michigan

12
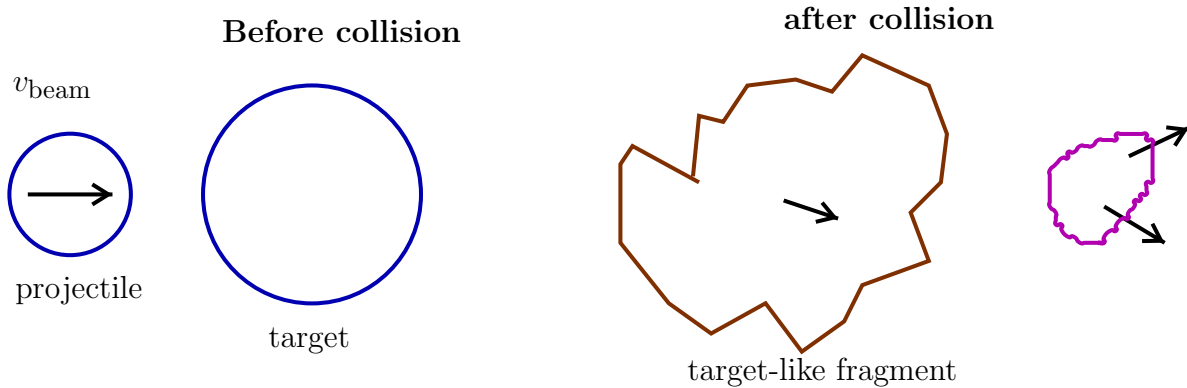
Figure 2.1: (For interpretation of the references to color in this and all other figures, the reader is referred to the electronic version of this dissertation.) Schematic of asymmetric collision. Projectile transfers momentum to the target. To measure linear momentum transfer, the longitudinal velocity of the target-like fragment is compared to the velocity of the center-of-mass of the collision.

State University's National Superconducting Cyclotron Laboratory to collide the beam with targets inside the 4π detector. A Si detector array was used to detect the time-of-flight and energy of emitted charged heavy fragments ($A \geq 10$), yielding the kinetic energy and masses of those fragments [30]. To determine $V_\parallel$ in the equation above, a filter on just the heaviest fragments was used. We assume that these heaviest fragments are a good estimate of the target-like fragment.

In the BUU calculation, the target-like residue is explicitly tracked throughout the collision, and its velocity is directly calculated from the constituent particles. The various cross section (CS) reductions described in Section 2.1 are tested, with the results shown with lines in Figs. 2.2–2.4. The Rostock and Fuchs reductions, as well as the case with no reduction ("free") are labeled, while the Tempered CS is marked by its tunable parameter ν.

It is clear from the LMT figures that the free cross section overestimates the stopping in all three reaction systems, and that the Tempered CS with $\nu = 0.2$ underestimates it. The Rostock and Fuchs reductions produce LMT values that are very close to each other in all
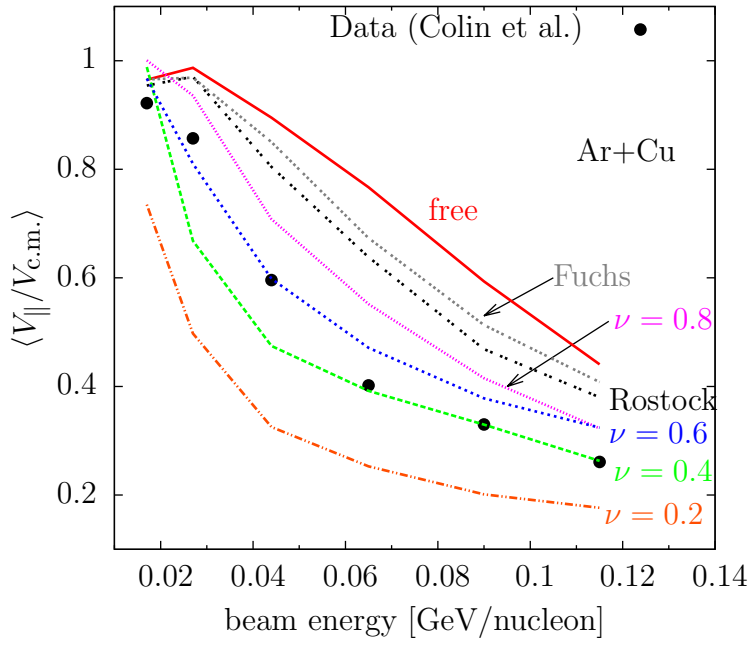
Figure 2.2: Linear momentum transfer for ^{40}Ar+Cu. Lines show the effects of different in-medium reductions of the NN cross section. The "Tempered" reductions are marked with their tunable parameter ν. Symbols are experimental data [2].
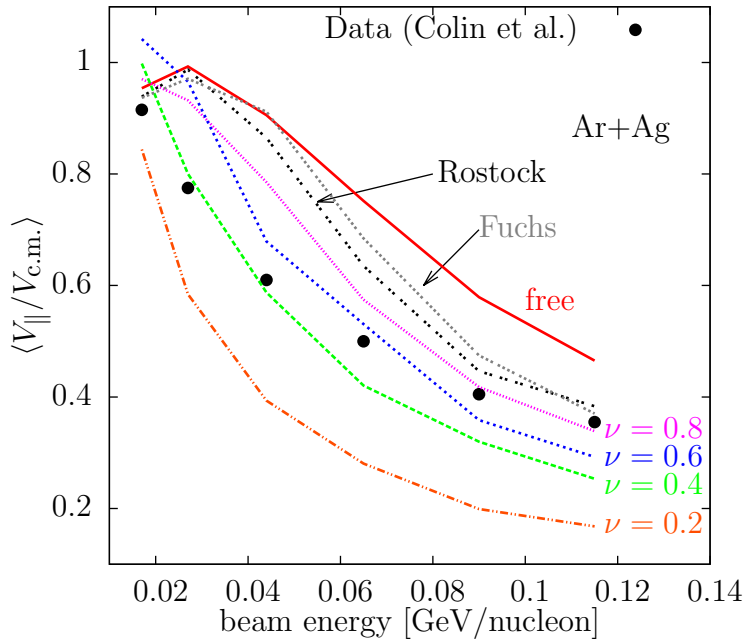
Figure 2.3: Linear momentum transfer for ^{40}Ar+Ag. Lines show the effects of different in-medium reductions of the NN cross section. The "Tempered" reductions are marked with their tunable parameter ν. Symbols are experimental data [2].
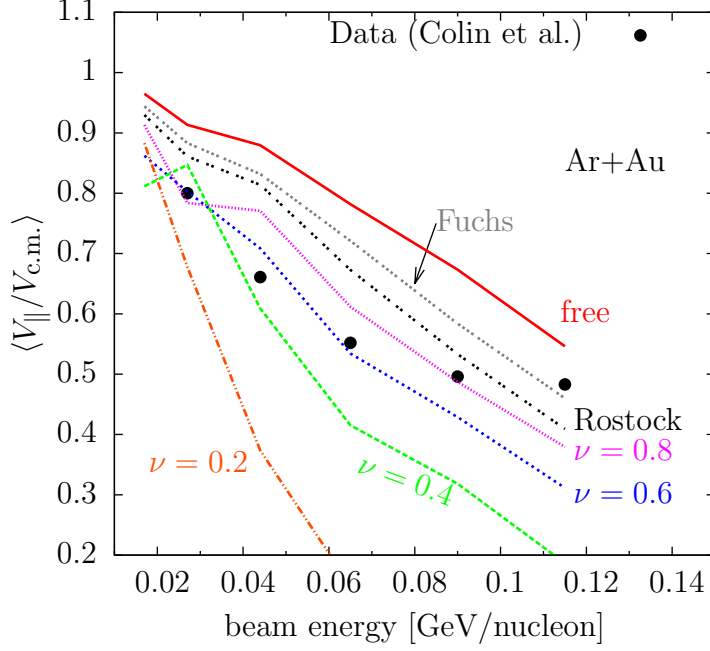
Figure 2.4: Linear momentum transfer for ^{40}Ar+Au. Lines show the effects of different in-medium reductions of the NN cross section. The "Tempered" reductions are marked with their tunable parameter ν. Symbols are experimental data [2].

cases, with Fuchs resulting in about 7% higher values than Rostock in the 65 MeV region.

Focusing on the trends, the free CS results in a linear dependence of LMT on beam energy in all three systems at about 27 MeV and higher, while the reductions all exhibit a positive concavity in the ^{40}Ar + Cu and ^{40}Ar + Ag cases that more closely resembles the data. In the case of ^{40}Ar + Au, all calculated lines show a roughly linear beam energy dependence, while the experimental data shows an even larger concavity compared to the smaller systems.

Judging by eye, the cross section that best fits the ^{40}Ar + Cu and ^{40}Ar + Ag data is the Tempered with $\nu = 0.4$ or 0.6. In the ^{40}Ar + Au reaction, however, due to the confluence of effects described in the previous paragraph, the cross section that best fits the data seems to be the Tempered CS with $\nu = 0.8$. Note that this determination of the in-medium cross section is only valid within the context of this specific model, the Boltzmann transport

15

simulation described in Section 1.2. The model-independent viscosity is calculated from this CS in Sec. 2.3.

2.2.2 Rapidity variance ratio *varxz*

If particles in the hot, dense region of a nuclear collision undergo many collisions (because the particle cross section is large), the region tends to equilibrate, and particles will lose memory of which direction they were originally travelling in. Emission from that region will be isotropic in the reaction center of mass. The observable *varxz* probes this isotropy. The FOPI Collaboration defines it thusly [31]:

$$varxz = \frac{\Delta y_x}{\Delta y_z},$$

(2.7)

where Δy_x is the variance of particle rapidity[1] in the direction that is transverse to the beam and fixed in the laboratory frame, which is a random transverse direction in the reaction center-of-mass system. Δy_z is the variance of the longitudinal rapidity (along the beam direction).

Fig. 2.5 shows the experimental results from FOPI [31] as well as the BUU transport simulation with the various in-medium NN CS reduction schemes used, for Au + Au, looking at the distribution of protons. The experiment was performed using the heavy ion accelerator SIS at GSI/Darmstadt, and charged particles were detected with a good coverage of angles throughout the 4π region, using the FOPI detector and a set of other detectors that pro-

---

[1]Rapidity, y_k, is a measure of a particle's velocity in a certain direction k, defined by $\tanh y_k = v_k$, where v_k is the component of particle velocity in direction $\hat{k}$. This is convenient for relativistic calculations, for if $y_{p/S}$ is the rapidity of a particle p in frame S, and $y_{S/S'}$ is the rapidity of frame S in frame S', then the rapidity of the particle in frame S' is given simply by $y_{p/S'} = y_{p/S} + y_{S/S'}$.
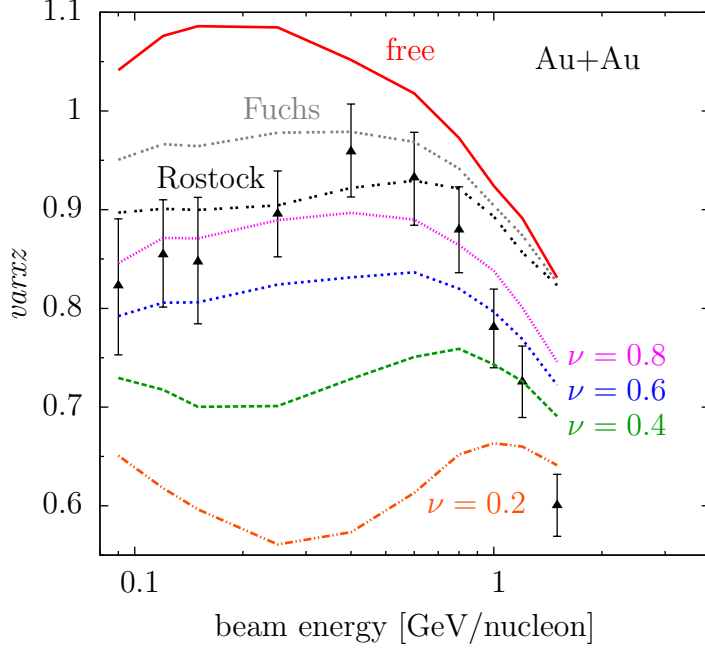
Figure 2.5: Stopping observable *varxz* for protons in Au + Au collisions at different beam energies at $b_{\mathrm{red}} < 0.15$. Lines show the effects of different in-medium reductions of the NN cross section. The "Tempered" reductions are marked with their tunable parameter ν. Symbols are experimental data from FOPI [3].

vided particle tracking, energy loss determinations, time of flight determination, and charged particle identification. The beam energies span the range from 0.09 to 1.5 GeV/nucleon, and the impact parameter selection was limited to $b_{\mathrm{red}} \equiv b/b_{\mathrm{max}} < 0.15$.

Inelastic scattering becomes more important than elastic scattering as the beam energy increases. (The pion has a mass of 135 MeV/c^2 [32], so its production become energetically allowed in individual NN collisions when $E_{\mathrm{beam}} > 300$ MeV/nucleon). Since only the elastic scattering cross section has been modified for the medium and not the inelastic channels, comparison for the purposes of determining the in-medium cross sections should be made at beam energies $\lesssim 400$ MeV/nucleon, the energy at which the pion production cross section starts to become significant in the dynamics. Given that caveat, it seems the CS reduction that best fits the data below 300 MeV/nucleon is either $\nu = 0.8$ or Rostock.
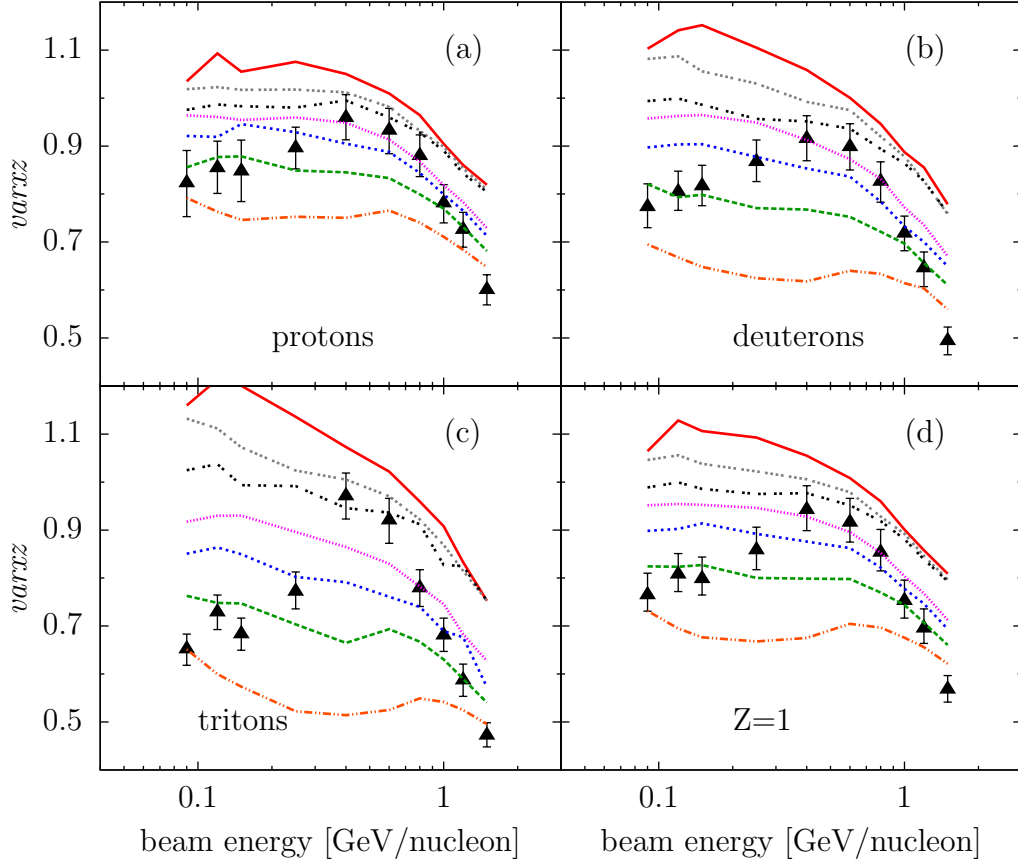
Figure 2.6: Same as Fig. 2.5, except that particle coalescence is enabled in the simulation, so comparison to different particle species in experiment is possible.

The observable *varxz* can also be produced for particles other than protons. The BUU transport simulation includes composite production that was not enabled for Fig. 2.5 — that is, no nuclear fragments heavier than $A = 1$ are produced in the code. If composite production is activated in the simulation [8], then particles up to $A = 3$ are produced (i.e. deuterons, tritons, helium-3). In this case, comparison with experiment for other particle species are possible and shown in Fig. 2.6.

Looking first at the experimental data, stopping decreases with increasing A, with the exception of a large enhancement of *varxz* for tritons at 400 and 600 MeV/nucleon. As

the beam energy decreases, especially for tritons, the experimental *varxz* decreases, while the simulation shows no such behavior. This is because at low energies in experiment, the projectile- and target-like residues have secondary decays that are not present in the transport calculations, making them less accurate. There is an increasing sensitivity to the NN CS with increasing A. If one focuses on those middle energies, then $\nu = 0.8$ or Rostock continue to best reproduce the experimental stopping (especially Rostock for the case of tritons).

Results for *varxz* in Ca + Ca collisions are shown in Fig. 2.7. Looking at $E_{\text{beam}} \lesssim$ 700 MeV/nucleon, one is left with one experimental point that is straddled by theory results for $\nu = 0.4$ and $\nu = 0.6$. However, the uncertainty of impact parameter in experiment is quite large (1–2 fm for Au + Au collisions [33]). If the impact parameter gate used in experiment was twice as much ($b_{\text{red}} < 0.3$ instead of < 0.15), then theory would give the results shown in Fig. 2.8. In this case, stopping is less sensitive to the CS reduction, but still gives the best fit for either $\nu = 0.4$ or $\nu = 0.6$.
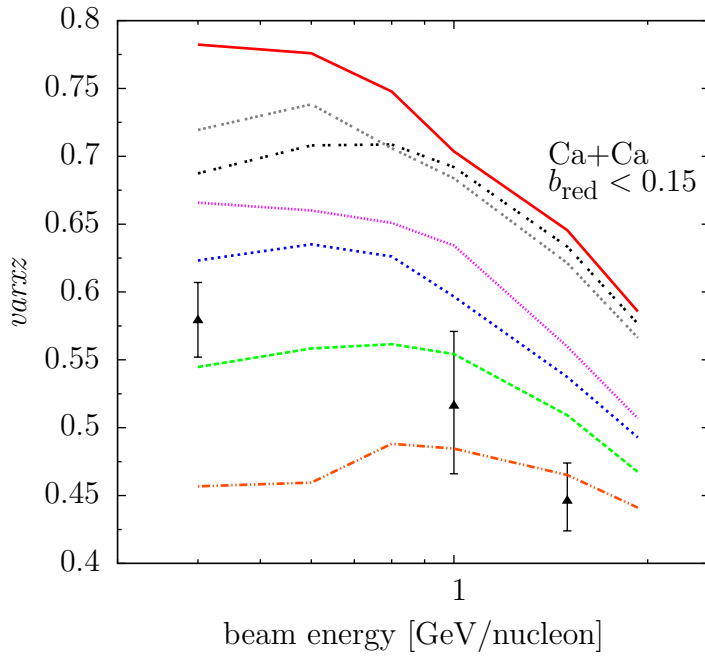
Figure 2.7: Stopping observable *varxz* for Ca+Ca collisions at $b_{\mathrm{red}} < 0.15$. Lines and symbols are the same as Fig. 2.5.
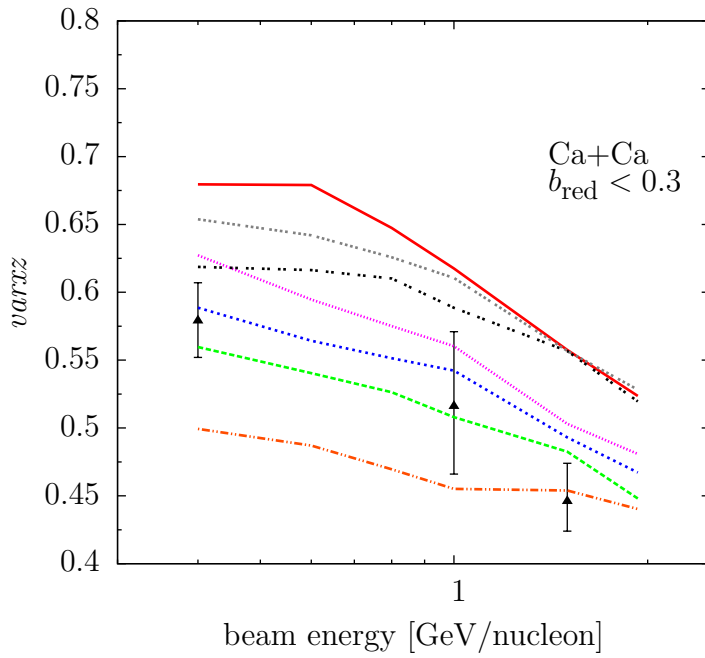
Figure 2.8: Stopping observable *varxz* for Ca+Ca collisions at $b_{\mathrm{red}} < 0.3$. Lines and symbols are the same as Fig. 2.5.

2.2.3 Isospin tracer

Another observable that we use as a measure of stopping is based on the isospin tracer technique, which is used to determine the relative yield of particles from the target and projectile in a given region of momentum space. This is done by using collisions between mirror nuclei and comparing to symmetric collisions of each of those two mirror nuclei.

The method is described here:

> "The (N/Z)-tracer method is based on the following idea: let us assume that we are observing the final number of protons, Z in a given cell of the momentum space. The expected yield Z^{Ru} measured for the Ru + Ru reaction is higher than Z^{Zr} of the Zr + Zr reaction since Ru has 44 protons as opposed to 40 for Zr. Such measurements using identical projectile and target deliver calibration values Z^{Ru} and Z^{Zr} for each observed cell. In the case of a mixed reaction, Ru + Zr or Zr + Ru, the measured proton yield Z takes values intermediate between the calibration values $(Z^{\mathrm{Ru}}, Z^{\mathrm{Zr}})$. If, e.g., Z is close to Z^{Ru} in a Ru + Zr reaction, means that the cell is populated predominantly from nucleons of the Ru projectile while if it is close to Z^{Zr} it is mostly populated from nucleons of the Zr target. In this way it is possible to trace back the relative abundance of target to projectile nucleons contributing to a given cell." [4]

The method yields the observable R_z, defined as

$$R_z = \frac{2 \times Z - Z^{\mathrm{Zr}} - Z^{\mathrm{Ru}}}{Z^{\mathrm{Zr}} - Z^{\mathrm{Ru}}} . \tag{2.8}$$

In this case, $R_z = 1(-1)$ corresponds to a momentum cell that is populated by protons completely from the Zr (Ru) nucleus. The case of complete stopping would mean that the protons completely mix and lose memory of which nucleus they were from. Thus, full stopping corresponds to $R_z = 0$.

The experimental results, along with results from the BUU transport model, for collisions between ^{96}Zr and one of its mirror nuclei, ^{96}Ru, are shown in Fig. 2.9, for a beam energy of
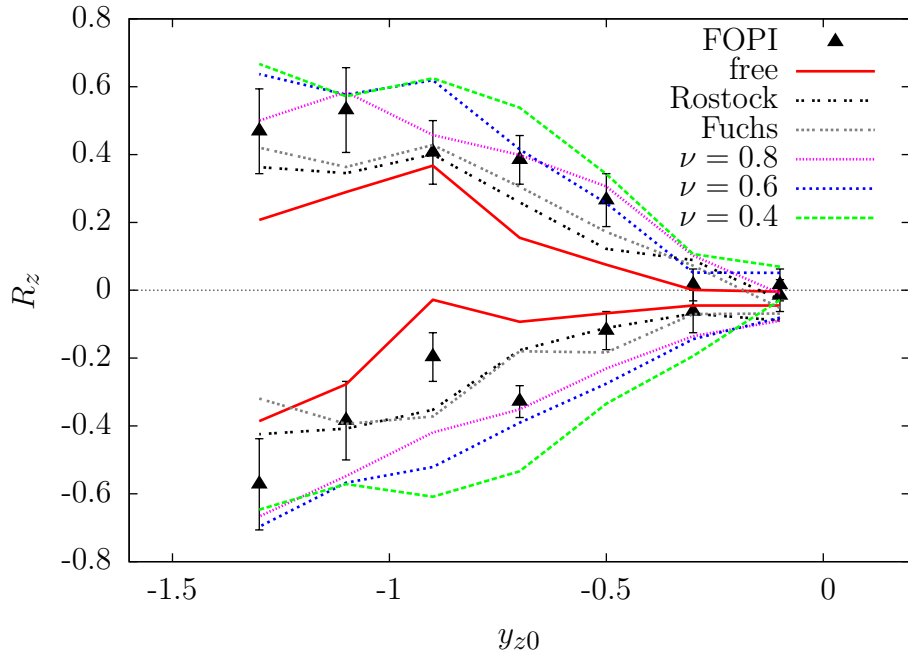
Figure 2.9: Isospin tracer observable for central collisions of ^{96}Zr $+$ ^{96}Ru (bottom) and ^{96}Ru $+$ ^{96}Zr (top) at 400 MeV/nucleon vs. scaled center-of-mass rapidity, where $y_0 = -1$ is the initial projectile rapidity. Data is from FOPI [4]. A value of R_z closer to zero indicates a higher degree of mixing, and thus stopping.

400 MeV/nucleon and $b_{\text{red}} < 0.12$. The experiment was performed at SIS/ESR-Darmstadt using the FOPI apparatus, TOF-wall, and the HELITRON and CDC drift chambers [4].

As center-of-mass rapidity gets more negative, the momentum cells are increasingly populated by protons from the target. This makes sense, as the target's particles are more likely to backscatter in the center-of-mass (opposite the direction of the beam). As the bins closer to midrapidity are examined, it is seen that those bins are populated by protons from both colliding nuclei, as R_z is close to zero there.

It is clear from Fig. 2.9 that use of the free NN cross section overestimates the stopping (mixing in this case). It seems that the CS best fitting the data here is either Rostock, Fuchs, or Tempered with $\nu \sim 0.8$. Statistical uncertainty is a difficulty with this observable, due to the subtraction of similar values, $Z^{\text{Zr}} - Z^{\text{Ru}}$, as well as division by the resulting small number.

2.2.4   Sensitivity to Equation of State

The equation of state (EOS) of nuclear matter describes how the energy changes with density and pressure, and is an important part of understanding the nuclear force and the effect on bulk systems [34]. In particular, the compressibility of nuclear matter, K, is a key input to calculations of neutron stars and some supernovae. It is commonly defined [35] as

$$K = 9\rho_0 \left. \frac{\partial^2 (E/A)}{\partial \rho^2} \right|_{\rho=\rho_0}.$$
(2.9)

The FOPI Collaboration found dependence of the stopping on the EOS [36], specifically the compressibility of nuclear matter, using the Isospin Quantum Molecular Dynamics (IQMD) model [37]. In Fig. 2.10, effects of two choices of compressibility, as well as a momentum-

dependent mean field, are shown. 'S' refers to a soft compressibility, $K = 210\,\text{MeV}$, while 'H' refers to a stiff or "hard" compressibility, $K = 380\,\text{MeV}$. 'M' refers to the inclusion of a momentum-dependent mean field, achieved by attributing to the nucleon an effective mass m^*, here using $m^*/m = 0.7$.

The combinations of SM and H give very similar results with our BUU transport model. The effects range as large as 16% for linear momentum transfer in $^{40}\text{Ar} + \text{Au}$ at high energy, and as low as within statistical and theoretical uncertainty in the case of *varxz* in $\text{Au} + \text{Au}$ and the isospin tracer R_z. Given a momentum-dependent mean field, the case is certainly distinguishable between stiff and soft compressibilities in stopping in $\text{Au} + \text{Au}$.

For the observables *varxz* and isospin tracer, the difference between the two plausible choices, soft with momentum-dependent mean field and stiff with momentum-indepedent mean field, is smaller than the difference between in-medium cross section reductions that we investigated. However, LMT is sensitive enough to this choice to render it less reliable for selecting the best cross section reduction.

2.2.5   Optimal cross section reduction

The determination of the in-medium NN cross section that best fits stopping data is not especially clear. The results are summarized in Table 2.1. There is a system size dependence, in that for all the reactions with $A < 150$, a stronger CS reduction is favored, while in heavier systems, less reduction in the cross section is needed to reproduce stopping. As speculation, this could be explained by the fact that in larger systems, each particle undergoes more chances to collide, since it must travel through a larger interaction volume. This means that the CS reduction is applied in more instances and has more of an effect on the stopping.
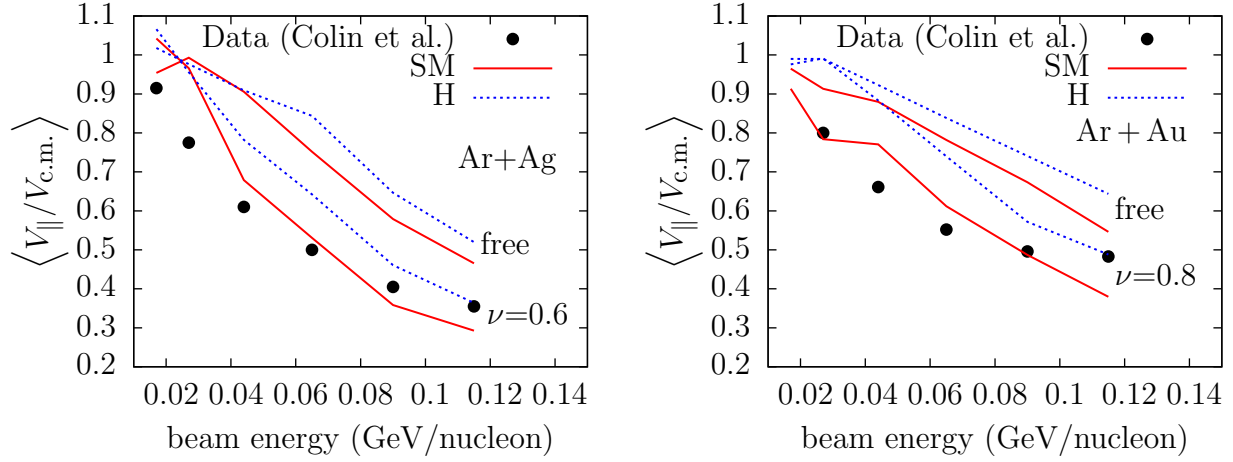
(a) Linear momentum transfer (LMT)
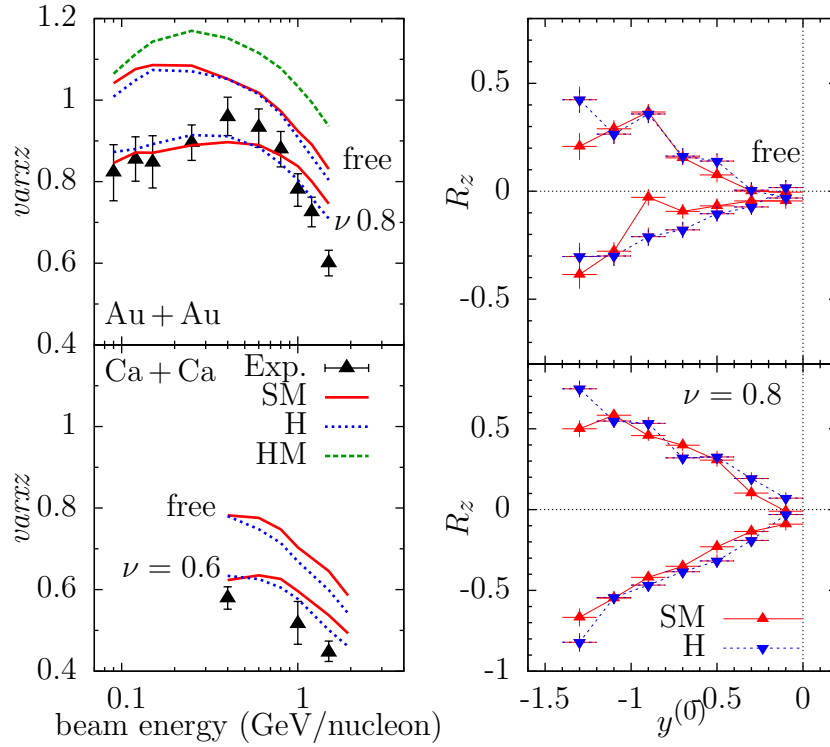
(b) *varxz*

(c) isospin tracer

Figure 2.10: EOS dependence of stopping observables. S (H) refers to a soft (stiff) compressibility, while M refers to the inclusion of momentum-dependence in the mean field. SM and H are both reasonable combinations, and they give similar predictions for stopping observables *varxz* and isospin tracer R_z. However, LMT is as sensitive to these settings as it is to cross section reductions, so that observable is less reliable for selecting the best reduction.

25

observable	reaction system	energies [MeV]	best cross section reduction
LMT	^{40}Ar + Cu	17–115	Tempered w/ $0.4 \leq \nu \leq 0.6$
LMT	^{40}Ar + Ag	17–115	Tempered w/ $0.4 \leq \nu \leq 0.6$
LMT	^{40}Ar + Au	27–115	Tempered w/ $\nu = 0.8$
varxz	Au + Au	90–1500	Tempered w/ $\nu = 0.8$ or Rostock
varxz	Ca + Ca	400–1500	Tempered w/ $0.4 \leq \nu \leq 0.6$
R_z	^{96}Zr+^{96}Ru	400	Tempered w/ $\nu = 0.8$, Rostock, or Fuchs
	(and inverse)		

Table 2.1: Summary of cross section determination results. No cross section reduction is favored universally, though Tempered with $\nu = 0.6$ or 0.8 appears to be the best compromise.

2.3 Viscosity

As a toy model to introduce the concept of viscosity, we describe laminar shear in a classical system. Consider two plates, with fluid between them, moving in antiparallel directions, in the steady state. The movement of one plate induces a shear stress, τ, on the layer of fluid below it, causing that layer to have a velocity $u < u_{\text{plate}}$. That layer induces a shear stress on the layer under it, and so on. In the linear approximation, these velocities can related using the equation $\tau = \eta(\partial u / \partial y)$, where $\hat{y}$ is perpendicular to the plates. Here, η is the coefficient of shear viscosity, which is a measure of the momentum transfer in the fluid.

2.3.1 Viscosity from BUU

The shear viscosity coefficient η can be derived from the BUU equation [38]. The result, for symmetric matter, is reproduced here:

$$\eta = \frac{5T}{9} \frac{\left(\int \mathrm{d}\mathbf{p}_1 f_1 p_1^2 \right)^2}{\int \mathrm{d}\mathbf{p}_1 \, \mathrm{d}\mathbf{p}_2 \, \mathrm{d}\Omega f_1 f_2 \tilde{f}_1' \tilde{f}_2' v_{12} \frac{\mathrm{d}\sigma}{\mathrm{d}\Omega} p_{12}^4 \sin^2 \theta} \tag{2.10}$$

Note that the NN cross section, σ, enters into the denominator. Since this equation is derived using the same assumptions as the transport model used to constrain the in-medium

26
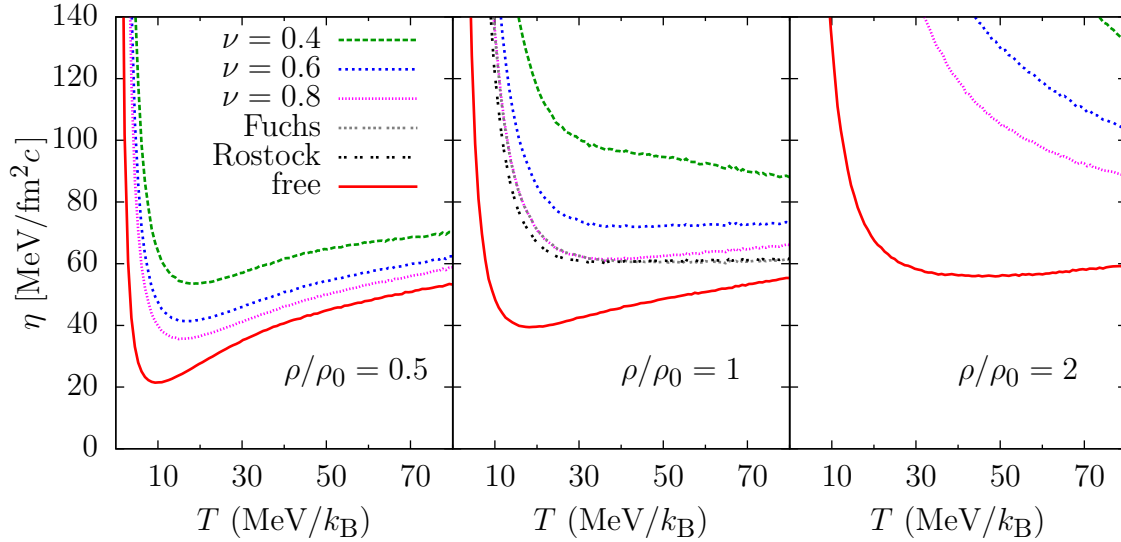
Figure 2.11: Viscosity for different temperatures, densities, and CS reductions. Note that for $\rho/\rho_0 = 1$, the Fuchs reduction overlaps with $\nu = 0.8$ up to about $T = 40\,\mathrm{MeV}/k_\mathrm{B}$, after which it overlaps with the Rostock reduction.

NN cross section, that cross section can be inserted into this equation to find a viscosity coefficient η that is model-independent. The calculation was performed with the effective mass described in Section 2.2.4, which tends to increase the viscosity somewhat.

The results of such calculations are found in Fig. 2.11. In all of the densities and CS reductions presented, the viscosity blows up at low temperature. At this temperature, the relative velocity between particles is low. Looking at Eq. 2.10, v_{12} is in the denominator, so this behavior makes sense. As the temperature increases, v_{12} increases while σ first drops very quickly and then flattens out. The combination of these causes a local minimum of η to appear. As the density increases, the NN reduction becomes stronger, directly causing an increase in viscosity, which is observed.

We now use our newly determined viscosity to explore how close nuclear matter is to being a "perfect fluid".

2.3.2 Lower quantum limit of ratio of viscosity to entropy density

It has been theoretically found that certain strong coupling limits of gauge theories have a constant ratio of shear viscosity to entropy density regardless of metric used,

$$\frac{\eta}{s} = \frac{\hbar}{4\pi k_B} \,,$$

(2.11)

where k_B is the Boltzmann constant [14]. Moreover, it is speculated that this value is a lower limit for all relativistic, finite temperature quantum field theories with zero chemical potential, and for single-component nonrelativistic gases of particles with spin 0 or 1/2 [14]. At Brookhaven's Relativistic Heavy Ion Collider (RHIC), in Au + Au collisions with energy $\sqrt{s_{NN}} = 200\,\mathrm{GeV}$, they found a value for η/s of $0.1\hbar/k_B$, quite close to the conjectured lower limit [39] and represented as a filled, red hexagon in Fig. 2.12. We calculate this ratio at our intermediate energies (IE) studied in this chapter, the entropy density having been estimated from cluster yields [8]. Represented as open hexagons in Fig. 2.12, the trend of the nuclear matter looks to match the findings at RHIC, at a much lower energy. The critical temperature $T_c \sim 170\,\mathrm{MeV}/k_{\mathrm{B}}$ for nuclear matter was taken from lattice QCD calculations [40].
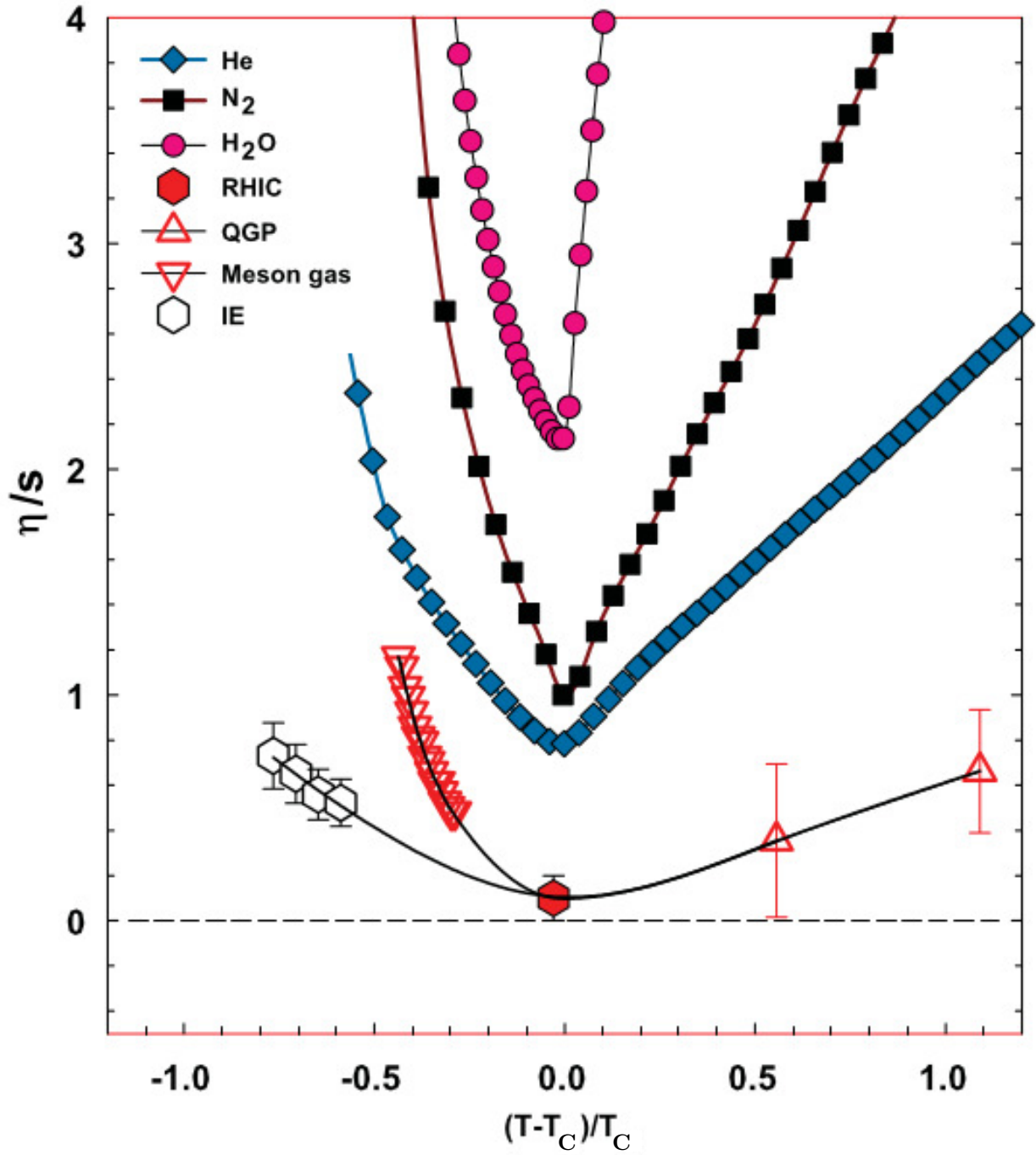
Figure 2.12: This work's estimate for η/s (in open hexagons) with the ratio given for other materials. RHIC has found a very low value, close to the proposed quantum lower limit (filled, red hexagon). We find that nuclear matter at intermediate energies approaches this value. The lines are to guide the eye. Compilation and figure from Ref. [5].

2.4 Conclusion

In this chapter, we investigated the viscosity of nuclear matter by adjusting the in-medium nucleon-nucleon cross section to fit nuclear stopping data with several different stopping observables across a wide range of nuclear mass and beam energy. We found that an in-medium reduction in the NN cross section is necessary to match experimental data. We calculated the shear viscosity and found that it is enhanced due to the medium effects, especially at higher densities. We also calculated the ratio of shear viscosity to entropy density, η/s, to determine the proximity of our reaction systems to the conjectured lower quantum limit. We found that the ratio follows a trend that matches with relativistic heavy ion collisions, suggesting that quark degrees of freedom may not be necessary to approach the limit of the "perfect liquid" seen at RHIC.

Chapter 3

Dynamics

3.1 Introduction

To explore the nature of nuclear matter at supranormal densities through observations, one must study either neutron stars or heavy ion collisions. Experimentally, we have just collisions between heavy nuclei, which generate brief pockets of nuclear matter at densities 2–4 times nuclear saturation density. It would be helpful to be able to focus on just the particles that are emitted from the high-density region. Unfortunately, the spatial and temporal resolution of current detectors are many orders of magnitude too coarse to directly trace back the position and time of emission of particles. Instead, for nuclear collisions, the detectors detect, among other observables, the momentum and energy spectra of emitted particles. Fortunately, the emitted particles affect each other in transit to the detectors, if they are close enough and move at similar velocities, developing observable correlations between the momenta of those particles. These correlations, coupled with information gained from transport simulations, allow us to identify particles that are emitted specifically from these high-density regions, giving an opportunity to study how nuclear matter acts at that scale.

Correlations between particles emitted in nuclear collisions develop in transit from the source of emission to the detector. Those correlations depend on the particles' relative scattering wavefunction, as well as the phase-space distribution of emitted particles. Thus,

correlations between particles emitted from collisions of nuclei can be used to determine the spacetime extent of the source of emission, giving an indication of the size and shape of the emitting region. This is loosely analogous to using light wave interference to determine the size and shape of a thin object, like a human hair. If we understand how the wave interplays with itself, then we can measure the interference pattern with millimeter resolution to discover the width of the hair at micrometer resolution.

For photons and other noninteracting, identical particles, intensity interferometry utilizes the Hanbury Brown and Twiss (HBT) effect, illustrated in Fig. 3.1. It was first used to study radio sources of galaxies by the eponymous authors [41]. Later, it was generalized to include correlations induced by Coulomb and strong interactions, when it found utility in elementary particle physics [42], relativistic heavy ion collisions [43], Bose-Einstein condensates [44], and intermediate energy heavy ion collisions (see Refs. in [45]). For these applications, especially heavy ion collisions, the generalized technique is now also called femtoscopy.

There are some methods of experimentally determining the timescale of the particles emitted during a collision, other than the one we show. Generally they involve determining which types of particle or fragments are emitted first, either using correlation functions of different species [46] or the N/Z ratio of the fragment [47]. The lifetime of individual emission sources has also been investigated [48]. For obvious reasons, these do not give the scale of the time relative to some initial start of the collision.

If particles are emitted from different regions of the collision that are moving with different velocities, then it stands to reason that filtering on these laboratory velocities would lead to isolating those different sources. For example, one group has identified several different sources of emitted particles from experimental data [49]. These are the source from the projectile-like fragment, from the target-like fragment, and from the interacting region.

32

They can be identified by their different laboratory velocities. Further, they have identified two sources in the interacting region: one from the emission as the fragments start to interpenetrate, and again after the participants have equilibrated and possibly formed a neck region connecting the projectile- and target-like fragments. These have been identified using a filter on total momentum of the particle pair in the center of mass of the collision. We use a similar filter to isolate the early emitting source in Section 3.3.

In studying the nuclear collision with BUU, it is important to identify the regime in which it is valid. In particular, it works fairly well for the liquid phase of nuclear matter, where the dynamics are affected by the mean field, as well as binary collisions. This is a good approximation for the early stage of a nuclear collision, when particles are close together, interact fairly often, and fluctuations are stochastically washed out. At later stages, once the interacting volume starts expanding, the particles become far enough away from each other that the dynamics follow the individual particles, the mean field is no longer a good description, and initial fluctuations will influence the evolution of the system. BUU is not equipped to handle this situation. Further, fragments of all sizes are produced, while the particular BUU model only produces fragments up to $A = 3$. It stands to reason that a way of filtering the output of experiment to focus on the early stage of the reaction would be important for accurately comparing to the BUU model.

In Section 3.2, I introduce the HBT interferometry and discussion extraction of the emission source. In Section 3.3, I will show how filtering the particles can emphasize the early emission. Finally, in Section 3.4, I show that the model predicts a much stronger resurgence in emission in heavy systems compared to light systems, explore why this is the case, and show how this can be detected in an experiment.
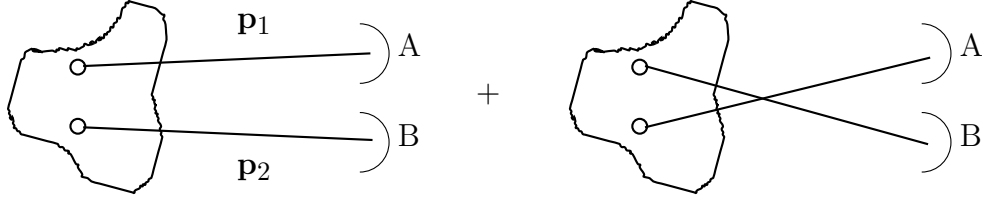
Figure 3.1: Schematic of HBT effect. Two particles with momenta $\mathbf{p}_1$ and $\mathbf{p}_2$ are emitted from the collision and observed at detectors A and B. If the particles are identical, then the emission is a quantum superposition of the left and right cases, leading to interference (figure from Ref. [6]).

3.2 HBT effect

When two photons with momenta $\mathbf{p}_1$ and $\mathbf{p}_2$, respectively, are emitted from a nuclear collision with a small relative momentum $\mathbf{q} = (\mathbf{p}_1 - \mathbf{p}_2)/2$, they will interplay with each other on the way to the detectors. Even for noninteracting, identical particles, their entanglement is described by a superposition of the two product states shown in Fig. 3.1. This superposition leads to a correlation in 2-particle intensity. Hence, the technique of learning about the size and shape of the emission source is called intensity interferometry.

For protons and other charged particles, another effect causes most of the correlation. If the protons are moving along with a similar velocity, and if they were emitted close enough together in time, then they will be subject to elastic scattering between them, either being repelled from each other by the Coulomb force or attracted by the strong nuclear force. This will lead to a correlation (or anti-correlation) within their relative momentum, from the perspective of the detectors. Since both this mechanism and the HBT effect give resolution on the level of femtometers, the techniques of using the correlations in reactions to learn about the size and shape of the emission region is called femtoscopy.

3.2.1   Correlation function

At the heart of observing the HBT effect is the 2-particle *correlation function*, which describes the correlation (or anti-correlation) between momentum states, $\mathbf{p}_1$ and $\mathbf{p}_2$. Experimentally, it can be observed as the ratio of the 2-particle yield, $\mathrm{d}N/(\mathrm{d}\mathbf{p}_1\,\mathrm{d}\mathbf{p}_2)$, to the multiplication of two single-particle yields, $\mathrm{d}N/\mathrm{d}\mathbf{p}$:

$$C(\mathbf{p}_1, \mathbf{p}_2) \propto \frac{\mathrm{d}N/(\mathrm{d}\mathbf{p}_1\mathrm{d}\mathbf{p}_2)}{(\mathrm{d}N/\mathrm{d}\mathbf{p}_1)(\mathrm{d}N/\mathrm{d}\mathbf{p}_2)}, \tag{3.1}$$

In nuclear collisions, the event mixing technique is often used, where the 2-particle coincidence yield is taken from a single collision event and the single-particle yields are taken from different events, to avoid autocorrelation effects. At large relative momenta $q = |\mathbf{p}_1 - \mathbf{p}_2|/2$, the emission tends to be uncorrelated and C approaches a constant. It is typically normalized such that the constant is unity.

To incorporate wider momentum volumes and thereby decrease statistical error, the angle-averaged correlation function is sometimes used. Here, C is integrated over all possible pair total momenta. The resulting function is dependent on the relative momentum $\mathbf{q} = (\mathbf{p}_1 - \mathbf{p}_2)/2$:

$$C(q) \propto \int \mathrm{d}\mathbf{p}\,\mathrm{d}\Omega_{12} \frac{\mathrm{d}N/(\mathrm{d}\mathbf{p}_1\mathrm{d}\mathbf{p}_2)}{(\mathrm{d}N/\mathrm{d}\mathbf{p}_1)(\mathrm{d}N/\mathrm{d}\mathbf{p}_2)}, \tag{3.2}$$

where $\mathbf{p} = \mathbf{p}_1 + \mathbf{p}_2$ and Ω_{12} is the direction of $\mathbf{q}$.

If the particles are uncorrelated, the probability of detecting a particle with $\mathbf{p}_1$ should not be affected by detecting a particle with $\mathbf{p}_2$. In that case, the probability of detecting both particles (numerator of Eq. 3.1) is proportional to the multiplication of the probabilities of detecting each individual particle (denominator) and $C(q) = 1$.
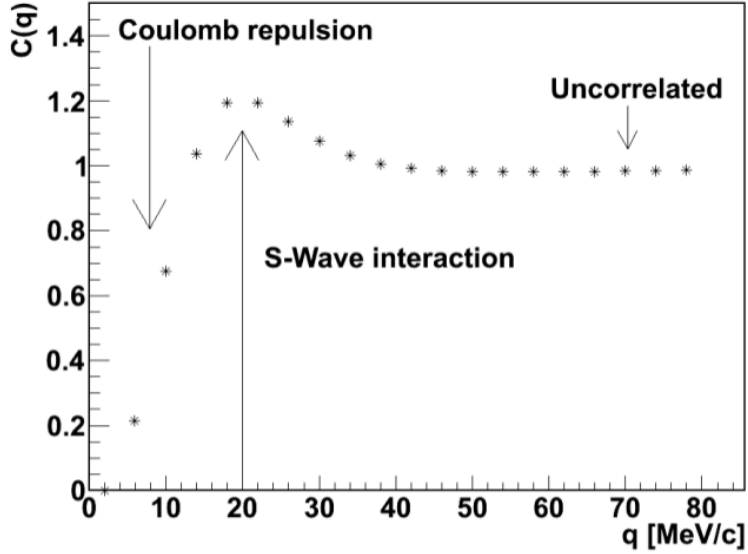
Figure 3.2: Sample correlation function [7]. At large q, particles are not correlated and the correlation function flattens to unity.

An example of a p-p correlation function is shown in Fig. 3.2. Below $q = 20\,\mathrm{MeV}/c$, it is less than one, which represents anticorrelation as the Coulomb force and Pauli blocking deplete low relative momenta. At large q, the protons are uncorrelated, since the probability for them to interact is so low, and thus $C(q)$ tends to unity. In the middle, $C > 1$ shows correlation, here caused by the $^1\mathrm{S}_0$ strong nuclear attraction.

In order to quantitatively analyze the correlation function and resolve the size and shape of the emitting source, we need to use the scattering wavefunction between the two particles and the Koonin-Pratt equation. This is described in the next section.

3.2.2   Source function

In experiment, the correlation function can be directly calculated from observables using Eq. 3.2. We would like to use it to learn about the size and shape of the region that emitted these particles. To resolve the actual size and shape of the emission source, the Koonin-Pratt

36

equation [50, 51] is used:

$$C(\mathbf{q}) = \int d\mathbf{r} \left| \Psi_{\mathbf{q}}(\mathbf{r}) \right|^2 S(\mathbf{r}) \tag{3.3}$$

The source of correlated particles is characterized by the *source function*, $S(\mathbf{r})$, which is defined as the probability of two particles to be emitted at a relative distance $\mathbf{r}$ in their center of mass. $\Psi_{\mathbf{q}}(\mathbf{r})$ is the scattering wave function of the two particles involved. This is analogous to the Young double-slit experiment, where the intensity of light on a screen (correlation function) is related to the superposition of the waves (wave function) and the width and orientation of the slits (source function).

The corresponding angle-averaged source function $S(r)$ is found by inverting the equation

$$C(q) - 1 = 4\pi \int dr\, r^2 K(r, q)\, S(r), \tag{3.4}$$

where $K(r, q)$ is the scattering kernel $\left| \Psi_{\mathbf{q}}(\mathbf{r}) \right|^2 - 1$, averaged over all angles.

To find the source function, an Ansatz is used, generally consisting of a Gaussian function $e^{-r^2/(2R^2)}$. The width R is adjusted to fit the experimental source function. This typical Ansatz assumes that the shape of the source is Gaussian, and that there is only one source of emission during the collision. As noted in Section 1.1, there are several different dynamical stages of the nuclear collision, which implies that particles will be emitted in different patterns in different dynamical stages, and thus there are several different emission sources. This makes interpretation of the Gaussian width more difficult.

Instead, the source function can be found directly by projecting Eq. 3.3 onto basis splines and inverting the resulting matrix. This allows the determination of the source with less prior assumptions about its shape [52].

In BUU, the source function can be directly calculated from the relative positions and

momenta of emitted particles, at the time of their emission. This is advantageous, as one need not rely on a theoretical wave function $\Psi_q(r)$ to construct the source. Since correlation is only built up between particles with similar momentum, the emitted particles are sorted into cubic momentum bins that are $25\,\mathrm{MeV}/c$ wide in each direction (in the laboratory frame). Within each bin, the distance between them, $r = |\mathbf{r}_1 - \mathbf{r}_2|$, is calculated, and this particle pair is counted as contributing to that part of the source function $S(r)$.

To determine whether a test particle is "emitted" in our BUU model, each particle is marked with the time of its last collision. At the end of the time evolution, if the density of the local medium is less than 1/15th nuclear saturation density $n_0 = 0.16\,\mathrm{fm}^{-3}$, then the test particle is considered emitted (if it is still in a higher-density region, then it would probably collide again, given more time).

3.3   Timescale of emission

To explore the dynamics of collisions, we choose one collision between high-mass nuclei, and one between low-mass nuclei, $^{112}\mathrm{Sn} + ^{112}\mathrm{Sn}$ and $^{40}\mathrm{Ar} + ^{45}\mathrm{Sc}$. Both have the same beam energy ($50\,\mathrm{MeV}$/nucleon) and impact parameter selection ($b_{\mathrm{reduced}} < 0.46$), as well as similar ratio of protons to neutrons (isospin asymmetry). In order to exclude emission from evaporation of the residues and isolate the high-density region, an angular filter is used to only accept particles that are emitted transverse to the beam direction in the center of mass ($70° \leq \theta_{\mathrm{cm}} \leq 110°$) [53].

The source functions $S(r)$ for the two systems, calculated from the transport theory, are seen in Fig. 3.3, with a zoomed view of the long-range tail inset in log scale. Since $S(r)$ is a probability density, its 3D integral sums to unity, and thus the height at a given distance
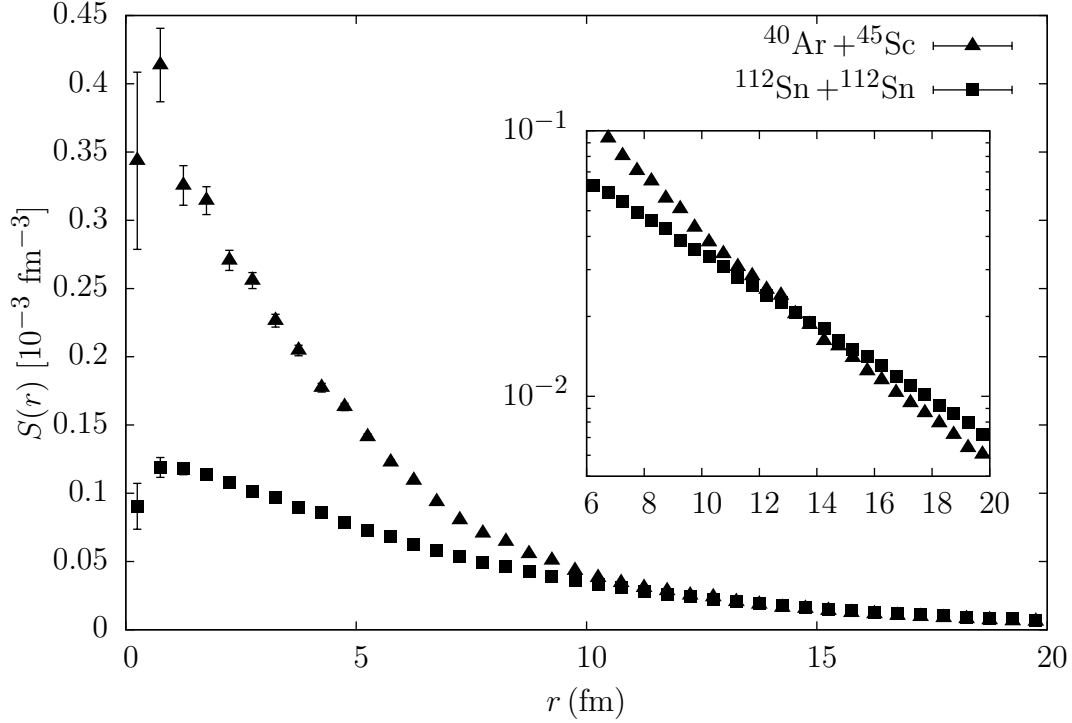
Figure 3.3: Source functions from BUU transport code. Inset is a close-up in log scale of the long-range part. The source for the smaller system is more peaked at short range, and it falls off faster at long range, compared to the larger system.

shows the relative weight of different ranges of the relative distance between 2 particles r. In the simulation, the integral of $S(r)$ is normalized in the range from 0 to 50 fm. Looking at the two sources, $^{40}\text{Ar} + ^{45}\text{Sc}$ shows a greater relative weight of the short-range component of the source, even as $^{112}\text{Sn} + ^{112}\text{Sn}$ has a greater number of particle pairs emitted with that relative distance, as witnessed by the smaller statistical error bars. At long range, visible in the inset, the source function of the smaller system falls off more rapidly, though both exhibit roughly exponential behavior.

Next, we describe a more systematic way of characterizing the shape of the source, in order to use it to understand the collision dynamics better.

3.3.1 Interpreting the source function

We want to have a quantitative method to compare source functions with each other, so that when we apply filters to emitted particles and produce the resulting source functions, we are able to more precisely notice any interesting effects. Additionally, experimental correlations are often fitted using analytic source functions, rather than inversion as described in Section 3.2.2. Therefore, it can be helpful to analyze the source function produced by the transport model in terms of such functions. To do this, we investigate different parameterizations that are fit to the source functions.

Different groups have come up with different ways of quantifying the size or shape of the source. If all that is wanted is the source size, then $r_{1/2}$, the half width at half maximum, could be used. This has the advantage that it is widely used and gives an estimate independent of any parametrization used. However, it loses details, especially in the behavior of the source at longer ranges. For this, one can use various fits to the source. Some have used generic cubic splines [54], 2-gaussian "hump fits" [55], or a superposition of Gaussian and decaying exponential behavior. Since this last one is the behavior of the source functions in Fig. 3.3, this is what we use[1].

However, a decaying exponential has a nonzero derivative of the form e^{-r} at $r = 0$. Since this is a one-dimensional function projected from three dimensions, the function should be smooth across $r = 0$. To compensate, the following form is used [56]:

$$S(r) = \frac{\lambda_{\text{gau}}}{N_{\text{gau}}} \exp\left[-\frac{r^2}{2R_{\text{gau}}^2}\right] + \frac{\lambda_{\text{exp}}}{N_{\text{exp}}} \exp\left[-\frac{\sqrt{r^2 + \beta^2}}{R_{\text{exp}}}\right] \tag{3.5}$$

[1]We also tried the convolution of two Gaussian sources with different widths and strengths, but it did not match the simulated behavior.

collision	λ_{gau}	λ_{exp}	R_{gau} (fm)	R_{exp} (fm)	f_{exp}
$^{40}\mathrm{Ar} + {}^{45}\mathrm{Sc}$	0.100(5)	0.915(4)	3.47(5)	5.09(5)	0.783(8)
$^{112}\mathrm{Sn} + {}^{112}\mathrm{Sn}$	0.006(3)	1.046(4)	4.16(15)	6.18(3)	0.87(2)

Table 3.1: Fit parameters for source functions. λ_{gau} and λ_{exp} are the fractions of particle pairs that contribute to the first and second terms of the equation. R_{gau} and R_{exp} are the widths of the Gaussian and exponential components, respectively. The fraction of particle pairs that contribute to the Gaussian shape, f_{gau}, is higher for the smaller system, while the larger system has a correspondingly longer exponential tail. Uncertainties are statistical from fit and do not include uncertainties of underlying model.

where $\beta = R_{\mathrm{gau}}^2/R_{\mathrm{exp}}$, and N_{gau} and N_{exp} are chosen to make each term have a 3D integration equal to unity when ignoring the λs (these factors are given in Eq. B.3). Thus, since $S(r)$ is a probability and should integrate to unity, λ_{gau} and λ_{exp} are the fractions of particle pairs that contribute to each term and should add to unity, if the equation accurately represents the source. At short distances, the second term acts as a Gaussian with the same radius as the first term, while at long distances, it behaves as e^{-r}, thus enabling the parameterization of the source into two components: Gaussian and exponential decay.

To find out the relative weight of the Gaussian and exponential components, it is insufficient to use the λ parameters above, since the λ_{exp} term contains part of the Gaussian component. Instead, to find the fraction of proton pairs that contribute to the Gaussian part of the source, the square root in the second term is expanded to the 2nd order in r, and the resulting Gaussian is integrated over the sphere to get the exponential fraction f_{exp} (see Eq. B.3 for the derivation).

The results of the fitting procedure (using MINUIT [57]) for the reaction systems studied are shown in Table 3.1. The resulting curves are shown along with the simulation results in Fig. 3.4. The Gaussian fraction f_{gau} is also listed in Table 3.1.

Looking at the source function, the smaller system has a smaller Gaussian width and a
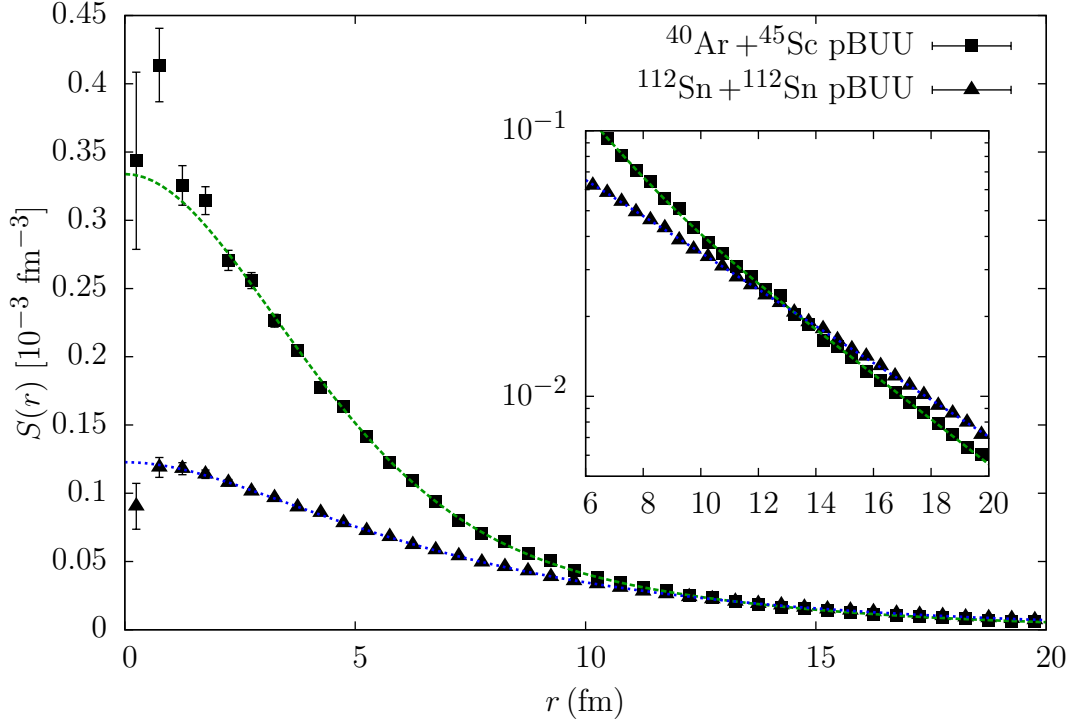
Figure 3.4: Source function $S(r)$ from BUU transport simulation for ^{112}Sn $+$ ^{112}Sn (triangles) and ^{40}Ar $+$ ^{45}Sc (squares). Also shown are curve fits using a short-range Gaussian and long-range exponential (seen in the logscale plot inset).

slightly smaller exponential tail, as expected. Overall, $f_{\exp}$ is smaller for ^{40}Ar $+$ ^{45}Sc than ^{112}Sn $+$ ^{112}Sn. Next, we use our time dependent model to investigate when and where these different components are emitted, and see if we can enhance one versus the other and thereby isolate one emission source for future study.

3.3.2 Time dependence of the source function

To determine when the protons are emitted that contribute to the various parts of the source, we use the BUU transport model described in Section 1.2 to simulate the collisions. Then, we use the explicit timing information given in the simulation to filter on different times and look at the result.

Naively, if the source function is constructed from only particles at early times, then the source should be smaller, since particles have less time to travel away from each other before being emitted. This suggests that particles from early time are correlated strongly with the short-range part of the source. Conversely, particles that are emitted from a source that has been expanding for some time will be, on average, farther apart from one another, leading to late emitted particles contributing primarily to longer ranges of the source function. A caveat here is that, in the calculation of the source function from the simulation, all particles are paired with others with similar momentum, regardless of time, so the early particles can contribute to longer ranges by being paired with a particle from a later time.

Using the transport code, we can test this by constructing a source function from particles that are emitted at selected times. This is done in Fig. 3.5 for ^{40}Ar $+^{45}$Sc. The early-time function matches the rationale given in the previous paragraph.
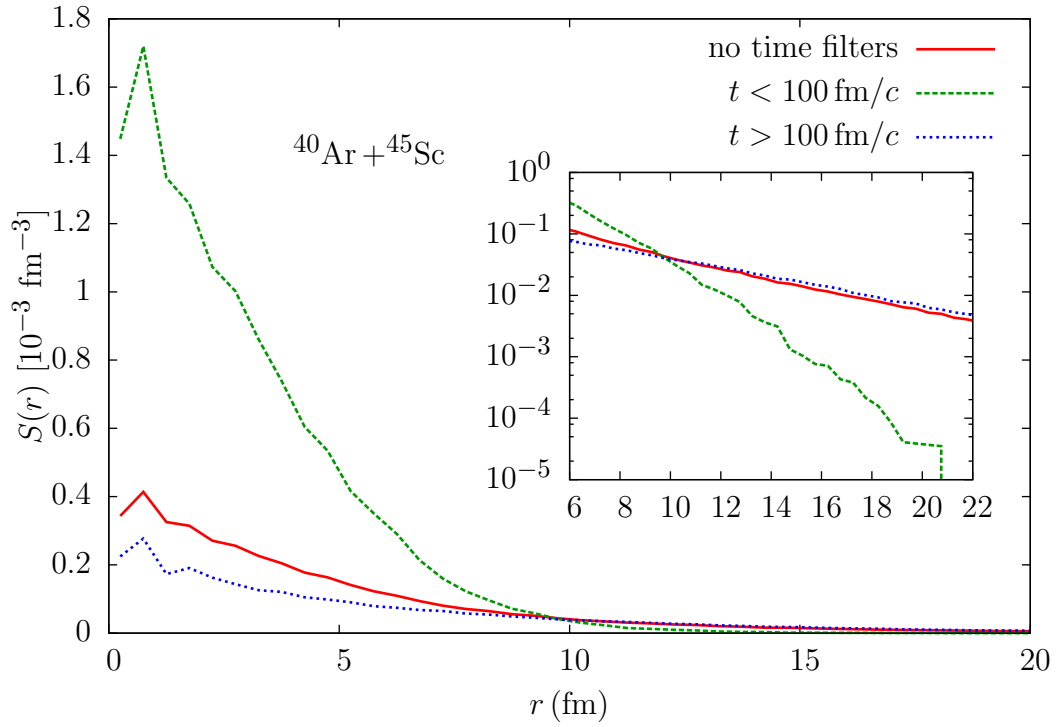
Figure 3.5: Source function for ^{40}Ar$+^{45}$Sc constructed from only early time (green, long dash) and only late time (blue, short dash).

3.4 Late-time resurgent emission

Now that we have a qualitative understanding, using a transport code, of how the emission time affects the source function, we examine the history of particle emission directly, from our transport model. Such a timeline of emission of protons is shown in Fig. 3.6. In both systems, there is one early peak, and in ^{112}Sn$+^{112}$Sn, one broad hump is seen at later times. This resurge in emission has not previously been predicted, to the author's knowedge. If it were evaporation (deexcitation of excited fragments), it should start immediately after the initial interpenetration. Instead, there is a lull in emission followed by a burst. To learn more, we inspect the phase distribution of these particles to find out what is happening.

3.4.1 Analysis of second emission

To start, we look at the spatial distribution of nucleons during the collision. Fig. 3.7 shows the nucleon density for both collision systems. Initially they have a similar evolution: inter-penetrating spheres lead to a large density in the middle of the collision. The collision of the heavier system takes longer, since the nuclei are larger in volume. Around $\sim 80\,\mathrm{fm}/c$, the spectator regions have passed each other and continue on their merry way. A dilute region of nuclei are left in the middle, the so-called "neck" region (seen around $120\,\mathrm{fm}/c$). At later times, around $230\,\mathrm{fm}/c$, a qualitative difference emerges — in ^{112}Sn$+^{112}$Sn, the particles in the neck region draw close together to form two sizable high-density regions, while in the lighter system, a single recontracted higher-density region is barely visible in the middle of the neck. Comparing with Fig. 3.6, this recontraction happens at the same time that proton emission increases.

To confirm that the protons are being emitted from these recontracting fragments, one
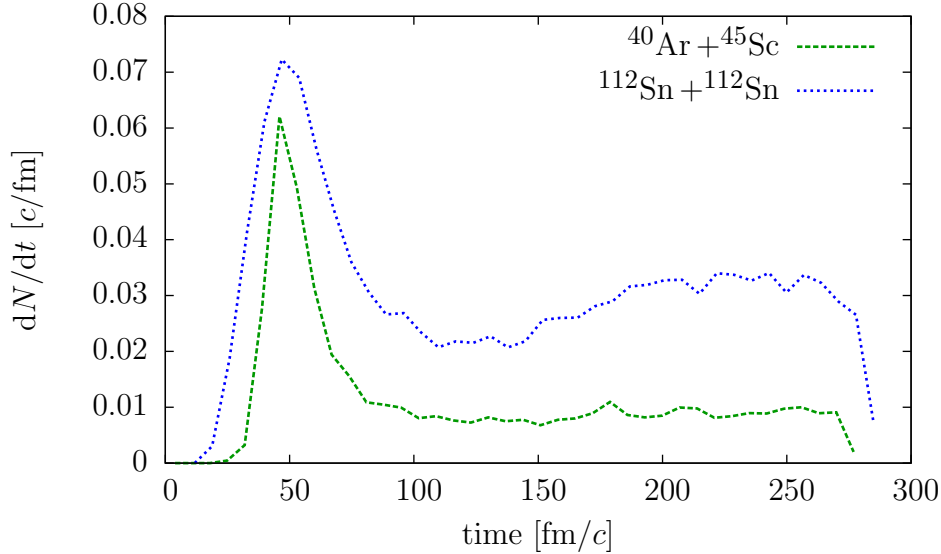
Figure 3.6: Proton emission versus time, from BUU transport simulation. Note the clear separation between early and late emissions and rise in late-time emission in the heavier system.

can see where the emitted particles are coming from, spread out over time. Fig. 3.8 shows this. Indeed, the emission is coming from the higher density region at early time, and at later times, an increase in emission occurs at the same time and location as the recontraction of the 2 fragments in the neck region.

To determine what causes this recontraction and emission, we compare the two collisions we are studying. The most significant difference between the two (for central collision dynamics, at least) is the volume of the interaction region and number of nucleons participating. One effect is that there is more volume in which NN collisions occur in the larger-A collision. Perhaps the nucleons collide so much that enough of them are pulled out of the projectile- and target-like fragments and into the neck region, where the mean field then causes them to seek higher densities (closer to the nuclear saturation density) and recontract into fragments.

To test this theory, the nucleon-nucleon cross section (σ_{NN}) in the heavier system can
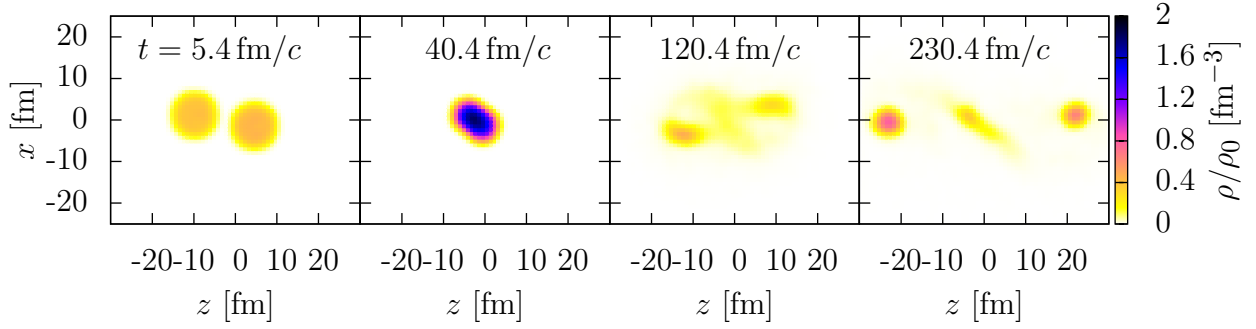
(a) ^{40}Ar + ^{45}Sc
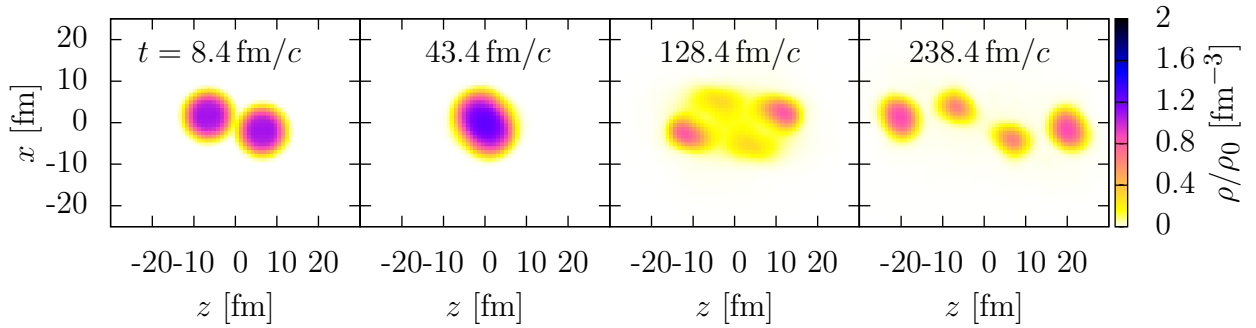
(b) ^{112}Sn + ^{112}Sn

Figure 3.7: Density contours at selected times after the beginning of collision of (a) ^{40}Ar + ^{45}Sc and (b) ^{112}Sn + ^{112}Sn. The heavier system has a recontraction of density at later times. Time is normalized so that the centers of the nuclei cross at $51\,\mathrm{fm}/c$ (as predicted with Coulomb effects, not including stopping).
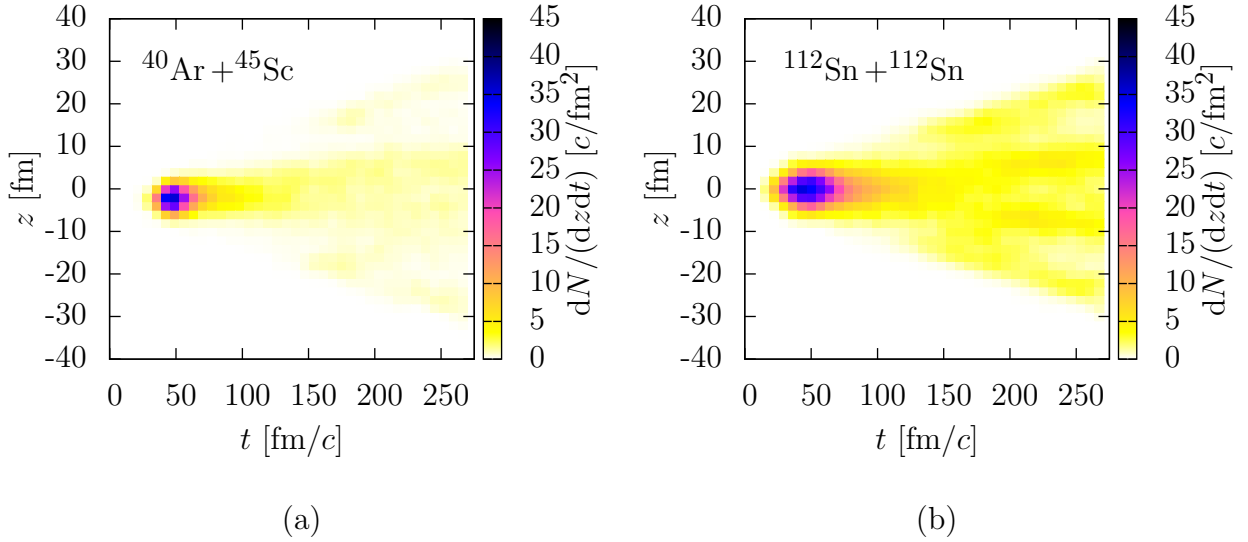
Figure 3.8: 2D histogram that shows where along the beam axis (z) protons are emitted as time goes on, for a) ^{40}Ar $+^{45}$Sc and b) ^{112}Sn $+^{112}$Sn. In the Sn collision, a second emission is quite pronounced, starting at about 125 fm/c. At late times, the emission is seen to come from 4 distinct regions, which are the positions of high density in Fig. 3.7b.

be reduced artificially, to mimic the effects of fewer collisions. To get a qualitative look, we

reduce it by 5 times. The reduction causes the resurgent particle emission to vanish, as seen

in the timeline of emission in Fig. 3.9, while not significantly altering the early emission. In

Fig. 3.10, we see that there is no recontraction of particles in the neck region at later times,

and in Fig. 3.11, the source function shows a slight reduction in the long-range exponential

part, which may be consistent with the behavior of the source function of the ^{40}Ar $+^{45}$Sc

collision. Thus, we learn that the formation of recontracted fragments in the neck region

is due to the certain ratio of nucleon mean free path to the size of the interacting region[2].

Now we show how to detect whether this recontraction occurs in reality, since we cannot

[2]Production of composite particles (deuterons, tritons, and ^{3}He) was turned off for these simulations, as the model used for composite production [8] is derived for higher energies and might not be valid at this energy [58]. Turning it on changes some of the dynamics, including causing some recontraction in the lighter system. It still shows and even reaffirms the effect of late-time recontraction causing emission of particles.
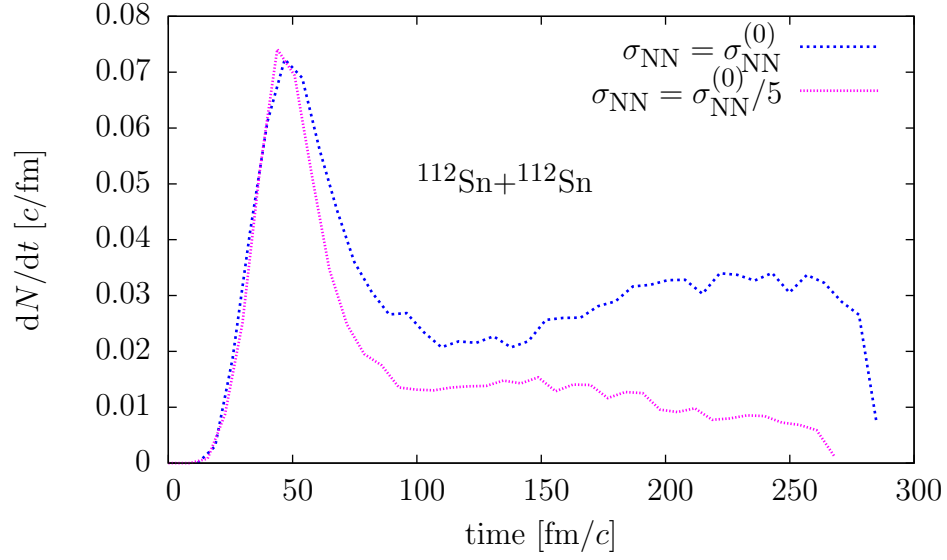
Figure 3.9: Emission timeline for ^{112}Sn $+^{112}$112 compared to the same with an *ad hoc* reduction in the NN cross section. The reduction suppresses the late emission, while leaving the early emission mostly unaffected.

manually adjust this ratio in experiment.
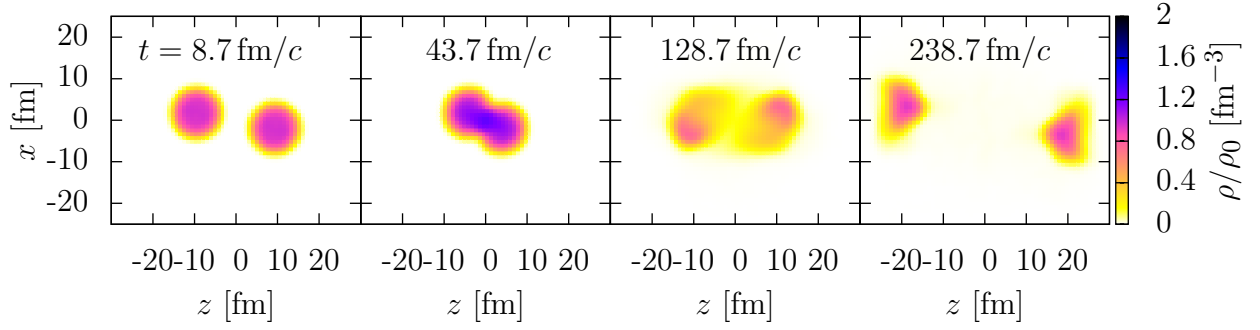
Figure 3.10: Density contours at selected times after the beginning of collision of ^{112}Sn $+^{112}$Sn with an *ad hoc* reduction of σ_{NN} by a factor of 5. Unlike the unreduced case seen in Fig. 3.7b, there is no formation of dense fragments from the neck region at late times.
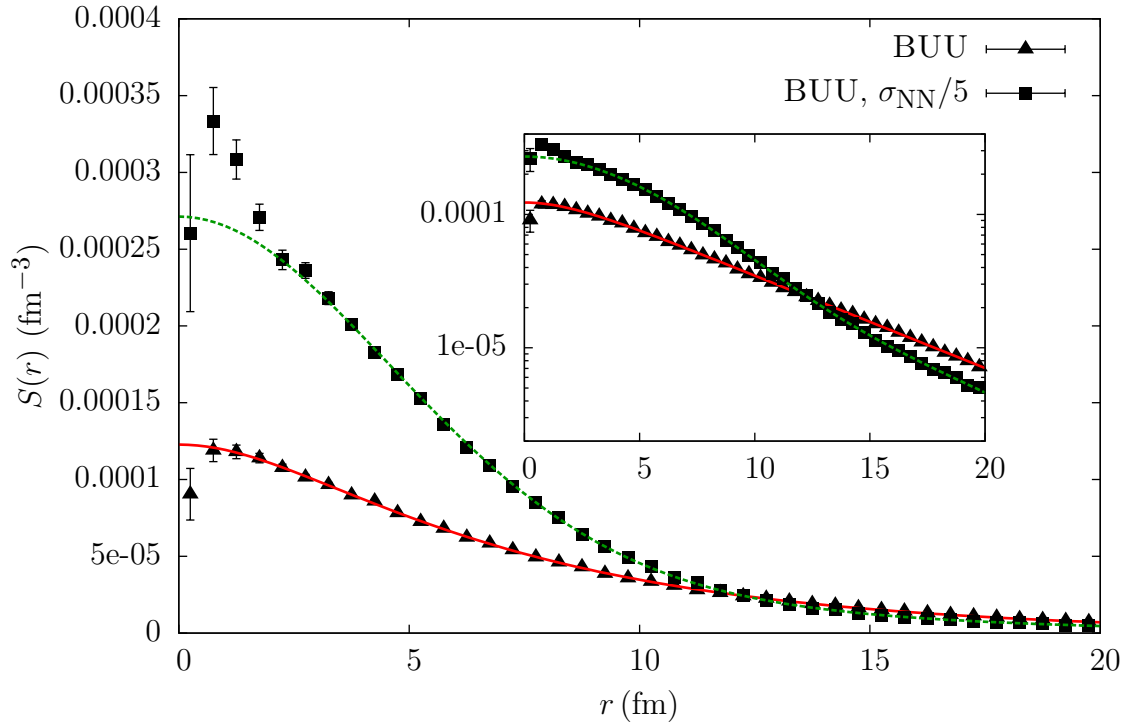
Figure 3.11: Source function for ^{112}Sn $+^{112}$Sn calculated in a transport model with a nominal NN cross section (triangles) and with an *ad hoc* reduction in that cross section (squares). The lines represent a fit using the Chung parameterization.

3.4.2 Detection in experiment

To determine whether this recontraction occurs in experiment, we need an observable that is based on the momentum structure, since that is all we have access to, and sensitive to the shape of the emitting source. As mentioned in the introduction, Ghetti and collaborators have used filters on laboratory velocity and total cms momentum of the pair to focus on sources of emission coming from different spacetime regions of the collision. Thus, it stands to reason to look at the spectrum of particles in transverse (to the beam) momentum. Such a 2D histogram is shown in Figs. 3.12 and 3.13 for ^{40}Ar $+^{45}$Sc and ^{112}Sn $+^{112}$Sn, respectively.

The figures show how many protons are emitted at a given cell of transverse momentum $(p_\perp/m)$ and time (t). The two emission regions at early and late time are clearly seen. In ^{112}Sn $+^{112}$Sn, the second re-emission is visible, showing that it only occurs at low $p_\perp/m$ (below $\sim 0.2\,c$), while the early emission extends to $\sim 0.4\,c$ for both systems.[3] We learn that for both systems, a filter on high $p_\perp/m$ suppresses the later emission, emphasizing the protons emitted during the initial interpenetration. Thus, we correlate a theoretical quantity, time, with an experimental observable, transverse momentum — by filtering on high $p_\perp$, we can access the particle sample dominated by the early emitted protons.

The effects of this filter in the source function $S(r)$ are seen in Figs. 3.14 and 3.15 for ^{40}Ar $+^{45}$Sc and ^{112}Sn $+^{112}$Sn, respectively. Also included are best-fit lines using the Chung fit parameterization, Eq. 3.3.1, including a short-range Gaussian and a longer-range exponential. In both cases, the relative proportion of protons contributing to the short-range Gaussian component is increased, as reflected by an increased value (since the source function

---

[3]A feature for future study is the 2 distinct regions at early time in ^{112}Sn $+^{112}$Sn, 1 at low $p_\perp/m$ and 1 at high. Turning composite production on shifts the lower one later in time relative to the more energetic region
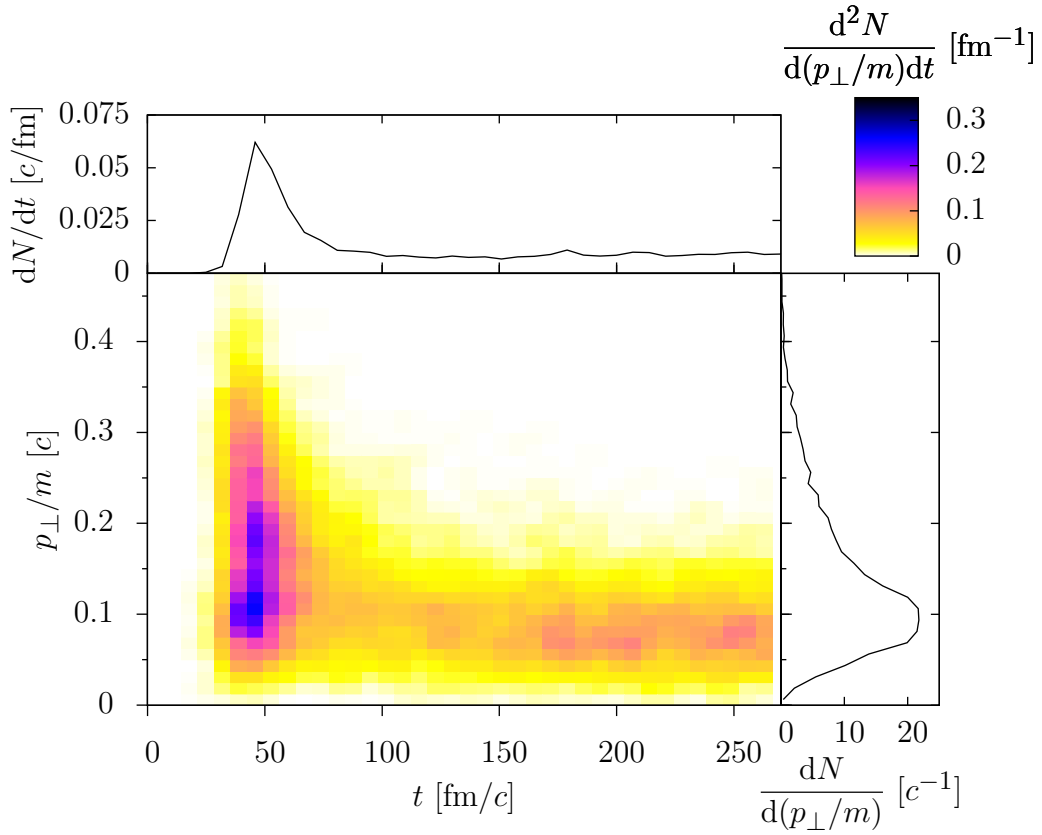
Figure 3.12: 2D Histogram of $p_\perp/m$ vs. t for protons emitted from collisions of ^{40}Ar $+^{45}$Sc. Also displayed are 1D histograms projected onto both axes. Emphasis on early emission in an experiment is possible with a filter on $p_\perp/m \gtrsim 0.15\,c$.
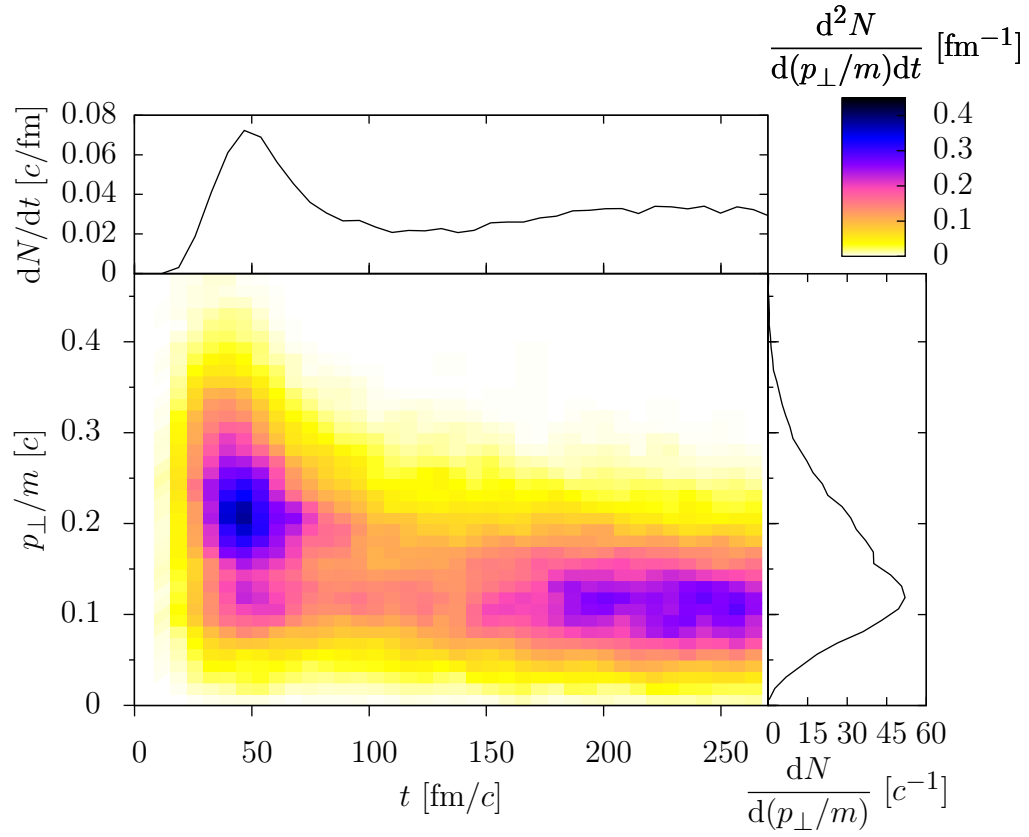
Figure 3.13: Same as Fig. 3.12, but for ^{112}Sn$+^{112}$Sn. The second surge in emission is very visible at late times.
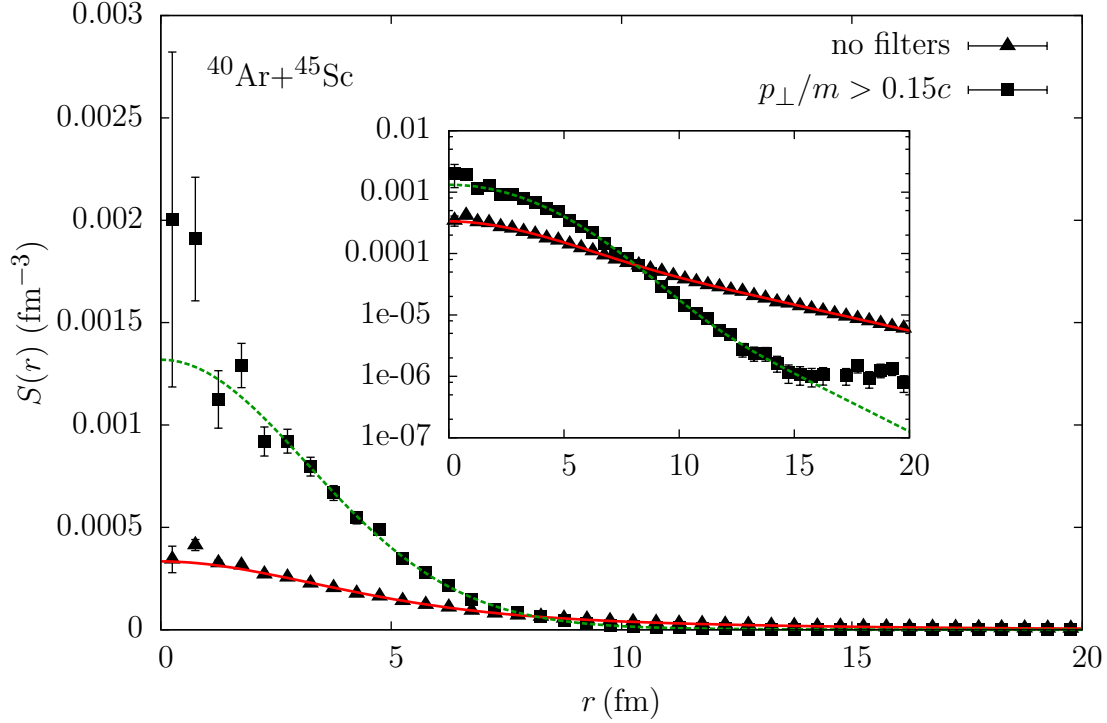
Figure 3.14: Source function for ^{40}Ar$+^{45}$Sc. Inset employs logscale to illuminate the effects of the high $p_\perp$ gate at far-away distances.

is a probability distribution). To more precisely see this effect, the best-fit Gaussian width and exponential width are given in Figs. 3.16 and 3.17.

In other work, it was found that the short-range size of the source, characterized by $r_{1/2}$, the half width at half maximum, was different by about $0.2\,\mathrm{fm}$, depending on the momentum filter used [59]. Looking more closely into the shape of the source using the Chung fit, we see that the width of the Gaussian source, R_gau, changes very slightly (The error bars only reflect the uncertainty and goodness of the fit, not the model uncertainties). Meanwhile, the width, or shallowness, of the exponential tail is affected greatly, suggesting that this region was primarily populated by protons with low $p_\perp/m$. This notion is verified by the calculation of the fraction of protons contributing to the exponential component, f_exp, also given in Figs. 3.16 and 3.17 — when we filter on high transverse momentum, we greatly
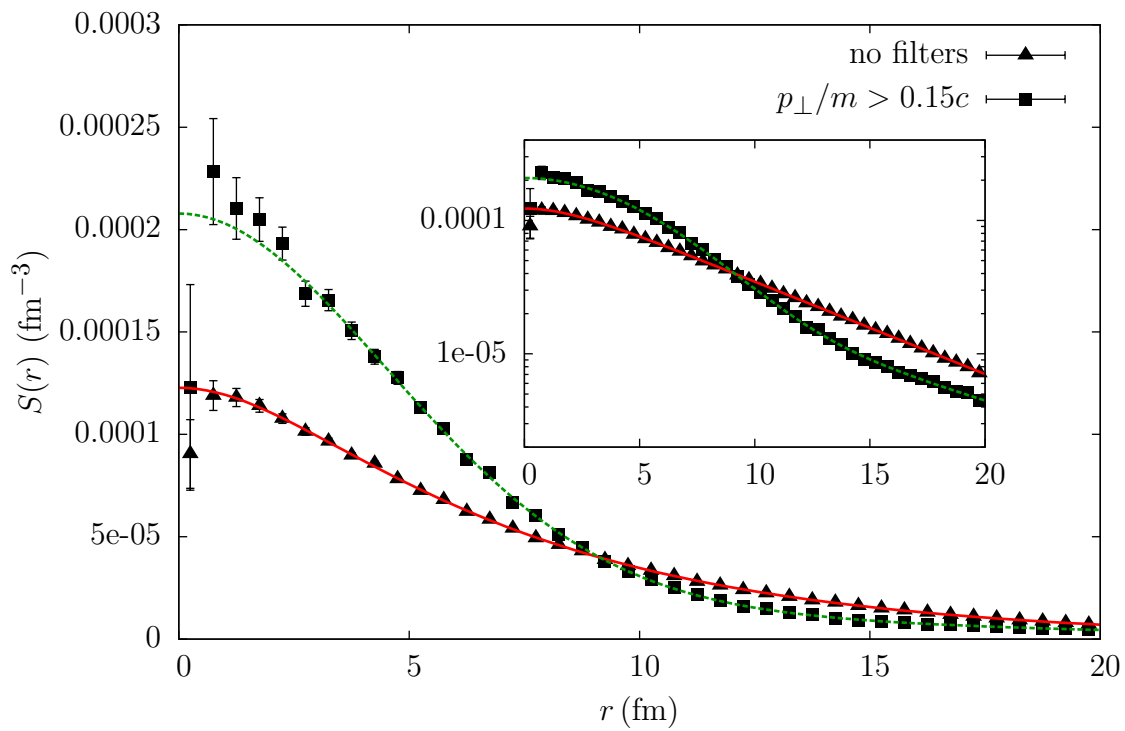
Figure 3.15: Source function for ^{112}Sn $+^{112}$Sn. Inset is in logscale, to see the effects of the high $p_\perp$ gate at long range.
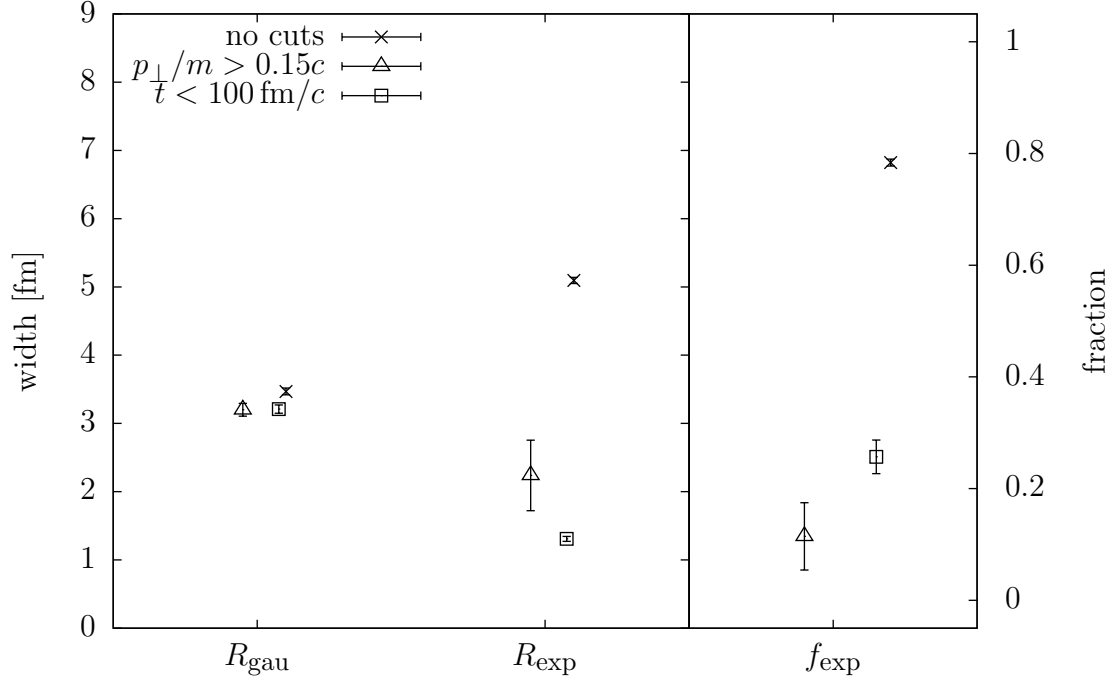
Figure 3.16: Fit parameters for source functions created with filters on the emitted protons, for ^{40}Ar $+^{45}$Sc. The filter allowing only early t (open squares) results in similar parameter values as for high $p_\perp/m$ (open triangles), showing that filtering on high $p_\perp/m$ selects for early t. Further, these filters enhance the Gaussian fraction f_{gau}, showing that the Gaussian component is primarily at early time.

decrease the contribution to the exponential component.

To verify that this is really representing the early part of the collision, we also construct the source function including only protons emitted before $100\,\mathrm{fm}/c$ and show the fit parameters as well. For all the parameters but R_{exp} for ^{112}Sn $+^{112}$Sn, it shows the same trend as for high-$p_\perp/m$, indicating that this momentum filter indeed does allow a dependence on early time. For R_{exp}, they have diverging behaviors. However, the uncertainty for this width for the early time filter shows that the there is still suppression of the exponential component, as there is less of an exponential trend to fit precisely.

According to Figs. 3.16 and 3.17, the source functions of both collisions under consider-
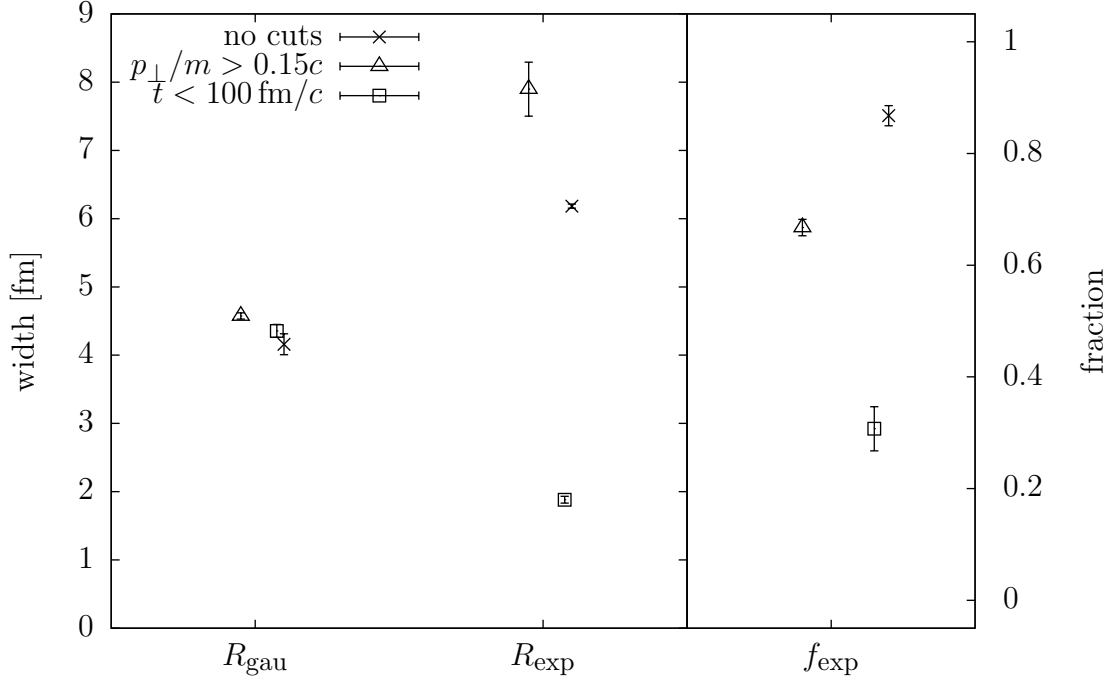
Figure 3.17: Same as Fig. 3.16, but for ^{112}Sn $+^{112}$Sn.

ation are affected qualitatively similarly by the filter $p_\perp/m > 0.15c$. Since ^{40}Ar $+^{45}$Sc does

not have any late-time recontraction and ^{112}Sn $+^{112}$Sn does, then this behavior of the source

function is not a good indicator of this recontraction that we can search for in an experiment.

Instead, we look at the collision in which we made an *ad hoc* reduction in the NN cross

section in Section 3.4. The effect of the $p_\perp/m$ filter on the source function is shown in

Fig. 3.18. The width of the Gaussian and exponential components of the source, $R_{\rm gau}$ and

$R_{\rm exp}$ respectively, are quite similar to that of the calculation with a nominal cross section, as

is the effect of the $p_\perp/m$ filter on $R_{\rm exp}$. Thus, the shape of each source is about the same as in

the nominal case, which gives credence to using this calculation as a prediction of dynamical

behavior, even though it has an unphysical NN cross section. The major difference is in

the fraction of proton pairs that contribute to the long-range exponential component, $f_{\rm exp}$,

with the calculation with the reduced NN cross section having a substantially suppressed
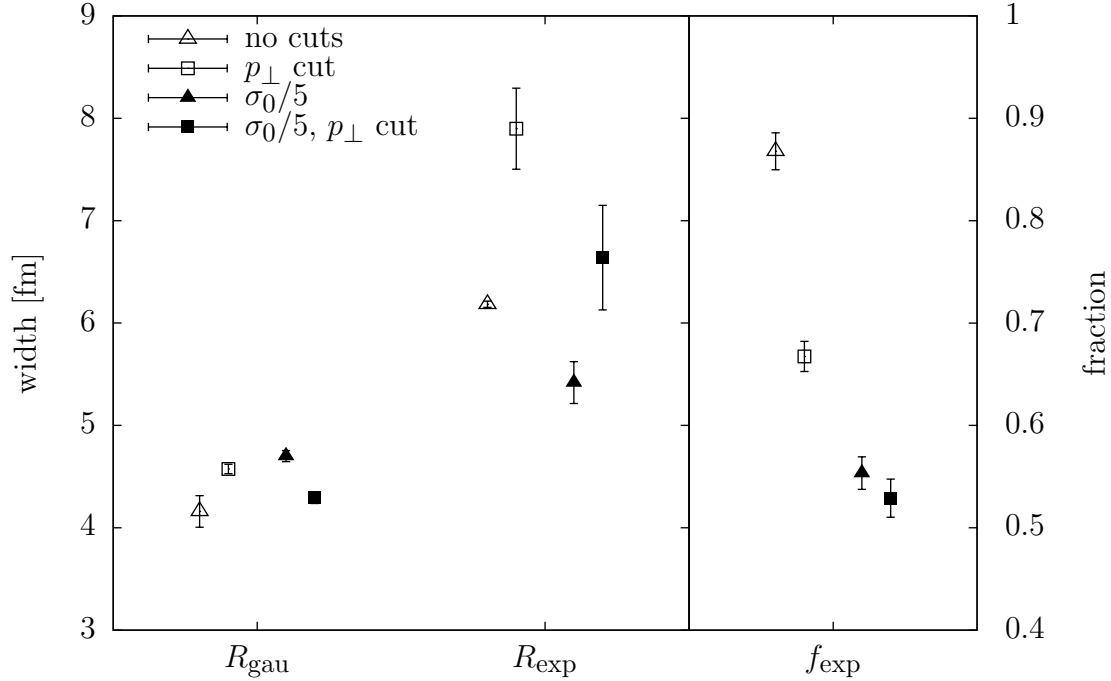
Figure 3.18: Parameters describing the shape of the source function for ^{112}Sn $+^{112}$Sn, calculated with a filter on transverse momentum, $p_\perp/m > 0.15c$ (squares) and without (triangles), as well as having the simulated reaction calculated with a nominal NN cross section (open shapes) and with an *ad hoc* reduction in that cross section, $\sigma = \sigma_0/5$ (filled shapes), which leads to no late-time recontraction. In the $\sigma/5$ case, the $p_\perp$ cut does not affect the exponential fraction f_{exp} like it does in the nominal case. Therefore, the sensitivity of f_{exp} to a cut in $p_\perp$ is a signal of this recontraction.

exponential fraction. This is consistent with our earlier conclusion that the substantial exponential component is caused by the late-time recontraction, which is not seen in the time evolution in this calculation.

The summary of f_{exp} results is shown in Fig. 3.19. In the simulation with the *ad hoc* σ_{NN} reduction, this fraction is not affected by the $p_\perp/m$ filter, as it is in the nominal σ case. This suggests that in the nominal case, there are two emission sources and one is suppressed by the filter more than the other, where in the $\sigma/5$ case, there is one source that is suppressed universally. Thus, if in experiment, the exponential fraction in the source function
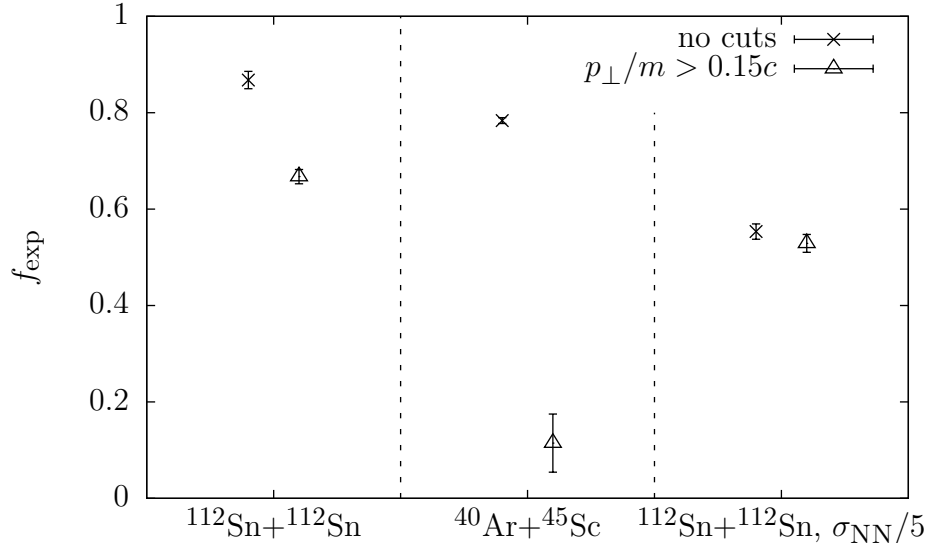
Figure 3.19: Fraction of proton pairs, f_{exp}, that contribute to the long-range exponential component of the source function, for the heavy system (left), light system (middle), and heavy system with *ad hoc* reduction in σ_{NN} (right). The first two collision systems produce a recontraction in the neck region and resurgent emission. Here, a filter on high $p_\perp/m$ causes a preferential suppression of the exponential component. With reduced σ_{NN}, the heavy system exhibits no re-emission, and the filter does not noticeably change f_{exp}, suggesting that the filter is only acting on 1 emission source, rather than 2.

is significantly suppressed by a filter on high $p_\perp/m$, then there is probably a recontraction

of nucleons occurring after the initial compression and expansion stages of the reaction.

3.5   Conclusion

In this chapter, we investigated the dynamics of central nuclear collisions at intermediate

energies. In particular, we used the source function to learn about the size and shape of the

proton emission region and provided an observable that correlates with late-time dynamics

of the collision.

We learned that the formation of recontracted fragments in the neck region is connected

with a certain ratio of nucleon mean free path to the size of the interacting region. To study

this effect, we demonstrated the correlation betweeen a theoretically accessible quantity, time, with an experimental observable, transverse momentum.

Finally, we predicted a second emission source, coming from a recontraction of particles in the neck region at late times. We showed that with a transverse momentum filter, we see this late-time source being affected differently than the early-time source, as evidenced by the exponential fraction changing significantly with the application of the filter. This is unlike many analyses of experiments at intermediate energies, where, in the end, only one source size was seen, no matter the transverse momentum filter. We showed that to test the theory of a late-time recontraction, one can use a high-$p_\perp$ filter and compare the relative contributions to the short- and long-range parts of the source function. If the relative contribution is the same, then only one source was present; if it changes, then two sources are present in the collision.

Chapter 4

Towards a fully quantal approach

In this work so far, we have simulated central nuclear collisions with a BUU transport model. While it has been and continues to be very useful and retains much predictive power, it has some drawbacks that we would like to overcome. The approach is inherently semi-classical, with an arbitrary divide between mean field and collision effects, and it is disconnected from approaches to nuclear structure. In this chapter, we take some early steps in implementing a transport model that does not have the above drawbacks.

Nonequilibrium Green's function (NGF) techniques [58, 60–62] represent a powerful tool to describe the evolution of correlated quantum many-body systems. The study of the Kadanoff-Baym (KB) dynamics in different quantum many-body systems is an ongoing challenge for theorists. The first direct implementations of NGF in homogeneous nuclear systems saw light almost 30 years ago [58]. Later advances include, among others, the extension to homogeneous electronic systems [63], small atoms [64], small molecules [65], quantum dots [66], and, more recently, double excitations in electronic systems [67, 68]. The advancement of dynamical quantum many-body methods is necessary for our understanding of systems that range from ultracold atoms [69] to nuclei [70] and atoms [64], a range of phenomena spanning 15 orders of magnitude in energy (neV to MeV).

Within nuclear physics, NGF techniques have been mostly used for derivations rather than exploited directly [62, 71, 72]. With so few quantitative studies on the impact of correlations in the time evolution of nuclear systems, one might wonder about the validity of

nuclear reactions simulations that are based on the mean-field picture or on semiclassical approaches. To clarify these issues, we would like to develop nuclear reaction simulations beyond the Hartree-Fock approximation. Nonequilibrium Green's functions, their time evolution described by the KB equations, represent a large step in that direction. However, with a naive algorithm, the KB equations are too computationally costly; therefore, we present a method to reduce this cost. We then apply a simplified model to the problem of 1D Bose Einstein Condensates (BEC), as they are an example of a physical quantum system in one dimension.

Historically, just a handful of methods have been developed to describe central nuclear reactions. Few of these are general enough to be employed in generating practical predictions. The time-dependent Hartree-Fock (TDHF) method has been exhaustively employed in describing low-energy reactions [73]. Nowadays, TDHF simulations can be performed in full 3D and involve nuclei as heavy as uranium [74]. However, the validity of TDHF requires correlations to play a negligible role in the dynamics [72]. At low energies, one expects that the role of correlations is minimal due to antisymmetrization effects. Conversely, one would expect correlations to dominate at higher beam energies, where the Pauli principle plays less of a role in the reaction dynamics.

In the semiclassical limit, the two-time KB equations reduce to a single-time Boltzmann equation, like the one used in the previous chapters. The Boltzmann equation approach deals with the increasing complexity of the reaction by using simplifying assumptions with an average, single-particle approach. Because of its inherently semiclassical nature, however, this kind of description remains genuinely disconnected from the quantum methods employed for nuclear structure [75–77]. More importantly, there is no systematic way of extending Boltzmann equation-type approaches to include more quantal effects.

Correlations can lead to a fast thermalization of the occupation of single-particle states and to enhanced stopping, compared to what can be found in TDHF [78–80]. Further, quantum effects may dominate in high-density regions and thus affect reaction observables. Therefore, if one is aiming at increasing incident energies, it is important to develop a quantal approach to central nuclear reactions that, besides the mean field effects, can also incorporate correlations. Unfortunately, even at the single-particle level, NGF techniques require handling vast amounts of information that can easily overwhelm the capabilities of computing systems, rendering this approach impractical in the naive approach.

In this chapter, we first introduce briefly the Kadanoff-Baym equations, which describe the time dependence of nonequilibrium Green's functions, followed by the mean field approximation that we use in the rest of the chapter. Next, in Section 4.3, we implement the mean field approximation in 1D, describing the time evolution of a collision of nuclear "slabs", including the solution of the initial ground state using the same framework as the time evolution and a discussion of the off-diagonal elements of the density matrix. In Section 4.4, we test the importance of those far off-diagonal elements, in anticipation of truncating them to reduce the computational cost.

Next we describe a coordinate rotation of the density matrix that allows us both to partially decouple the position and momentum domain, increasing the efficiency of accessing arbitrary momentum regimes, as well as straightforwardly truncating the density matrix in the off-diagonal direction to reduce the computational cost. Finally, we implement the density matrix evolution to describe the initial state of a Bose-Einstein Condensate of ultracold atoms.

4.1 Kadanoff-Baym equations

We aim to describe the dynamics of correlated nuclear systems using the KB equations. They are, in general, derived without any particular assumption on the physical system under consideration. They describe the time evolution of the single-particle Green's functions for fermions or bosons,

$$
\begin{aligned}
G^<(x_1, t_1; x_{1'}, t_{1'}) &\equiv \ i \left\langle \hat{a}^\dagger(x_{1'}, t_{1'})\, \hat{a}(x_1, t_1) \right\rangle, \\
G^>(x_1, t_1; x_{1'}, t_{1'}) &\equiv -i \left\langle \hat{a}(x_1, t_1)\, \hat{a}^\dagger(x_{1'}, t_{1'}) \right\rangle,
\end{aligned}
\tag{4.1}
$$

where $\hat{a}^\dagger$ and $\hat{a}$ are the single-particle creation and annihilation operators, respectively, and where the expectation values, $\langle \cdot \rangle \equiv \mathrm{Tr}\{\hat{\rho}_i \cdot\}$, are taken with respect to an initial density matrix, $\hat{\rho}_i$, at $t = t_0$. We consider initial states that are uncorrelated, even though the theory can incorporate correlated initial states [58].

The KB equations for 1D systems, governing the evolution of Green's functions in their arguments, follow from considerations of the equations of motion for creation and destruction operators [60]:

$$
\begin{aligned}
\left\{ \ i\hbar\, \frac{\partial}{\partial t_1} + \frac{\hbar^2}{2m} \frac{\partial^2}{\partial x_1^2} \right\} G^{\lessgtr}(\mathbf{11'}) &= \int dx_2\, \Sigma_{\mathrm{HF}}(x_1, x_2; t_1)\, G^{\lessgtr}(x_2, t_1; \mathbf{1'}) \\
&\quad + \int_{t_0}^{t_1} d\mathbf{2}\, \Sigma^+(\mathbf{12})\, G^{\lessgtr}(\mathbf{21'}) + \int_{t_0}^{t_{1'}} d\mathbf{2}\, \Sigma^{\lessgtr}(\mathbf{21'})\, G^-(\mathbf{21'}), \\
\left\{ -i\hbar\, \frac{\partial}{\partial t_{1'}} + \frac{\hbar^2}{2m} \frac{\partial^2}{\partial x_{1'}^2} \right\} G^{\lessgtr}(\mathbf{11'}) &= \int dx_2\, G^{\lessgtr}(\mathbf{1}; x_2, t_{1'})\, \Sigma_{\mathrm{HF}}(x_2, x_1, t_{1'}) \\
&\quad + \int_{t_0}^{t_1} d\mathbf{2}\, G^+(\mathbf{12})\, \Sigma^{\lessgtr}(\mathbf{21'}) + \int_{t_0}^{t_{1'}} d\mathbf{2}\, G^{\lessgtr}(\mathbf{12})\, \Sigma^-(\mathbf{21'}),
\end{aligned}
\tag{4.2}
$$

where the notation $\mathbf{1} \equiv (x_1, t_1)$ has been introduced. The retarded $(+)$ and advanced $(-)$ Green's functions are defined according to

$$G^{\pm}(\mathbf{1}, \mathbf{2}) = G^{\delta}(\mathbf{1}, \mathbf{2}) \pm \Theta\left[\pm(t_1 - t_2)\right]\left[G^{>}(\mathbf{1}, \mathbf{2}) - G^{<}(\mathbf{1}, \mathbf{2})\right] , \qquad (4.3)$$

where G^{δ} stands for a possible singular contribution at $t_1 = t_2$. The self-energies $\Sigma^{\pm}$ are defined similarly, except that the singular contribution is instead explicitly included in the first term on the r.h.s. of Eq. 4.2 as Σ_{HF}, to emphasize its mean field nature and to foreshadow the approximation in the next section. The generalized self-energy $\Sigma(\mathbf{1}, \mathbf{2})$ introduces interaction effects on the time evolution and also describes excitation processes within the system [58, 60].

The self-energy in the previous equations has been separated into two different components. The first one involves the Hartree-Fock (HF) contribution, $\Sigma_{\mathrm{HF}}(x_1, x_2; t)$, which accounts for the instantaneous, one-body interaction of the considered particle with the mean-field produced by the other particles of the system. The term involving $\Sigma^{\lessgtr}$ describes time-dependent excitation processes, beyond the mean-field changes. Such contributions account for the effect of correlations on the dynamics and need to be included for a complete description of nuclear reactions.

1D calculations are rather economical in terms of CPU and storage. Let us consider, though, the difficulties associated to storing density matrices (or Green's functions) in D dimensions without explicit spin or isospin degrees of freedom. A uniform mesh of size N_x in each direction will yield matrices of size N_x^{2D}. Fairly sparse meshes with $N_x \sim 10$ are already computationally demanding for $D > 2$. For 1D this is not an issue, and we present results with $N_x \sim 100$, which can be carried out straightforwardly, so that we may study a

tractable situation and see how to reduce the computational cost before moving to 3D.

In addition to spatial variables, NGF requires a suitable infrastructure to keep track of the time degree of freedom, as memory effects come into play. From Eq. 4.2, one can see that the time derivative of the Green's function $G^<$ at times t_1 and $t_{1'}$ depends on the Green's functions and self-energies at all the previous times t, $t_0 < t < t_1$ and $t_0 < t < t_{1'}$, via the time integrals on the r.h.s. Consequently, to find a solution of the KB equations, one must keep track of all the previous time-steps. For a uniform mesh of N_t points in time, the $G^{\lessgtr}$ functions thus require handling $N_x^{2D} \times N_t^2$ matrices. For $D > 1$, this becomes a major concern in the numerical implementation of the KB equations [81].

4.2   Mean field approximation

The KB equations simplify substantially when the correlation effects, described in terms of $\Sigma^{\lessgtr}$, are neglected. In that case, the evolution equations for $G^<$ and $G^>$ can be decoupled. Since the single-particle observables are more straightforwardly expressed in terms of $G^<$, we concentrate on the evolution of that function. Thanks to the instantaneous nature of Σ_{HF}, the set of equations for the time-diagonal elements of the Green's function, $t_1 = t_{1'}$, can also be closed and there is no need to consider explicitly time off-diagonal terms. Note, in particular, that this reduces the dimensionality of the problem to N_x^{2D}, as one can update $G^<$ at every timestep, and there is no need to keep explicit track of expectation values involving the past.

The evolution equations simplify even more when assuming a negligible range for the

particle-particle interactions. In that case, the evolution equation becomes

$$i\hbar\frac{\partial}{\partial t}G^<(x_1, x_{1'}; t) = \left[-\frac{\hbar^2}{2m}\left\{\frac{\partial^2}{\partial x_1^2} - \frac{\partial^2}{\partial x_{1'}^2}\right\} + U(x_1, t) - U(x_{1'}, t)\right]G^<(x_1, x_{1'}; t), \quad (4.4)$$

where U is related to Σ_{HF}, in the local limit, with $\Sigma_{\text{HF}}(x_1, x_2; t) = \delta(x_1 - x_2)U(x_1, t)$. This

can easily be linked to TDHF by expanding the Green's functions in terms of single-particle

states [70]. For the same initial state and mean-field parametrization, both approaches yield

identical dynamics. Our goal here is not so much to provide an accurate description of 1D

nuclear mean-field dynamics, as this has been a path well tread by others in the past, but

rather to explore its implementation in terms of Green's functions.

4.3   Collision of one-dimensional nuclear slabs

As a first example of implementation, we investigate the collision of two one-dimensional slabs

of spin-isospin saturated nuclear matter. Thus, each shell (energy state) contains 4 nucleons,

a combination of spin-up and spin-down neutrons and protons. Consider the evolution of

the one-body density matrix, found via the Green's functions,

$$\rho(x, x', t) = -iG^<(x, t; x', t) \quad (4.5)$$

In the 1D interpretation, the nucleon density is given by

$$n_1(x, t) = \nu\rho(x, x; t), \quad (4.6)$$

where ν is the nucleon degeneracy, $\nu = 4$, multiplied by the diagonal of the density matrix.

In this mean field approximation, we would like to interpret the results in a 3D situation, even though it is a 1D simulation. The 3D density, n, can be related to the 1D density by [70]

$$n(x,t) = \sqrt{\frac{5}{3}} \left(\frac{\pi n_0^2}{6\nu^2} \right)^{1/3} n_1(x,t),$$ (4.7)

where n_0 is the nuclear saturation density, $n_0 = 0.16\,\text{fm}^{-3}$. This relation allows us to employ well-known 3D mean field parameterizations for 1D calculations. We choose a simple nuclear mean field parameterization for our calculations,

$$U(t) = \frac{3}{4} t_0\, n(x,t) + \frac{2+\sigma}{16}\, t_3\, [n(x,t)]^{1+\sigma}\;,$$ (4.8)

with the free parameters, t_0, t_3, and σ, fitted to the saturation properties of nuclear matter [70] (Here, σ has no relation to the cross section. It is merely an unfortunate homonym). For such a local mean field, the time evolution of the density matrix can be implemented numerically in a rather straightforward way using the Split Operator Method [70,82]. This involves a repeated switching between position and momentum space, optimally accomplished using Fast Fourier Transforms (FFT) [82], implemented here with the FFTW library [83].

4.3.1   Preparation of the initial state

To describe the time evolution of a system, one needs a well-defined initial state. To describe a collision between nuclei, the nuclei start in their ground state (besides the necessary center-of-mass motion). However, the potential described in Eq. 4.8 does not have an analytic solution for the ground state, so some numerical method needs to be used to produce it. In the BUU implementation used in Chapters 2 and 3, the Thomas-Fermi approximation is used. Instead,

we would like to use the same computational framework to initialize the ground state as we do for the time evolution. This becomes important for describing correlated initial states, and it reduces development time due to code reuse.

In particular, the initial state for a reaction (or any other dynamical process) should be a ground state within the same approximation scheme as used in the dynamics. This guarantees that observables for the ground state do not change with time, and thus it is actually a ground state.

Since it is more reliable to start with an analytic ground state, we slowly switch from a potential with such a state to our desired potential as we evolve forward in time, a method known as adiabatic switching [84]. If switched smoothly and slowly enough, then the density matrix will move to be, at every step, in the ground state of the current potential. Therefore, at the end of the switching, the density matrix represents the ground state of the desired, non-analytic potential.

For the collision of 1D nuclear slabs, we use a harmonic oscillator (HO) initial state [70]. With the adiabatic switching, the single-particle potential acquires an explicit time dependence and we adopt the switching potential

$$U_{\text{switching}} = F(t)U_0 + [1 - F(t)]U \,, \tag{4.9}$$

where U_0 is the initial HO potential, $U_0 = \frac{1}{2}m\Omega^2 x^2$, U is our mean field potential, and $F(t)$ is the switching function. Ω is chosen to minimize the shape difference between the ground state of the two potentials, to speed up the transition. For the switching time evolution from time t_i to t_f, we choose $F(t)$ such that it transitions monotonically and smoothly from 1 to 0 with a transition timescale τ, which should be longer than any characteristic time of the

69

system.

Slower adiabatic switchings should provide better approximations to the mean-field ground states. In the top panel of Fig. 4.1, we show the evolution of the energy per nucleon for a HO slab with initial time $t = -1000 \, \text{fm}/c$. We concentrate on a single case, with $N_s = 2$ HO shells filled (*i.e.* $A = 8$ nucleons in the 1D interpretation). We consider different transition times, τ, that characterise the adiabaticity of the transition. For any of the employed transition times $\tau \geq 5 \, \text{fm}/c$, the energy evolves to a value very close to that for the static Hartree-Fock solution (see inset). Judging the quality of the adiabatic transition on the basis of the energy alone is potentially treacherous, though, as the energy is quadratic in the deviation of wave function from the ground state. In principle, final states for the adiabatic evolution might be found, with a wavefunction poorly approximating that of the mean-field ground-state, but giving an energy close to the ground-state value.

Alternatively, the total density, n, is linear in the deviation of the wavefunction from the ground state, so it may provide a better measure of the wavefunction quality. With this in mind, in the bottom panel of Fig. 4.1, we show the evolution of the size of the slab, defined as twice its average extent in 1D. Indeed, for $\tau = 5$ and $10 \, \text{fm}/c$, slab sizes exhibit significant oscillations in the final state, indicating that the ground state has not been yet satisfactorily reached. Instead, the final state in the dynamics is an excited state of the final hamiltonian and thus fluctuates over time. For $\tau \gtrsim 30 \, \text{fm}/c$, the oscillations become insignificant, with the slab sizes practically coinciding with that of the static Hartree-Fock solution.

Now we have the initial state of one nuclear slab. To simulate a collision, they must be made to collide with each other. In practice, this is acheived with a momentum translation or "boost" operator [85]:

$$\rho_K(x, x') = e^{iKx} \rho_0(x, x') e^{-iKx'} \tag{4.10}$$
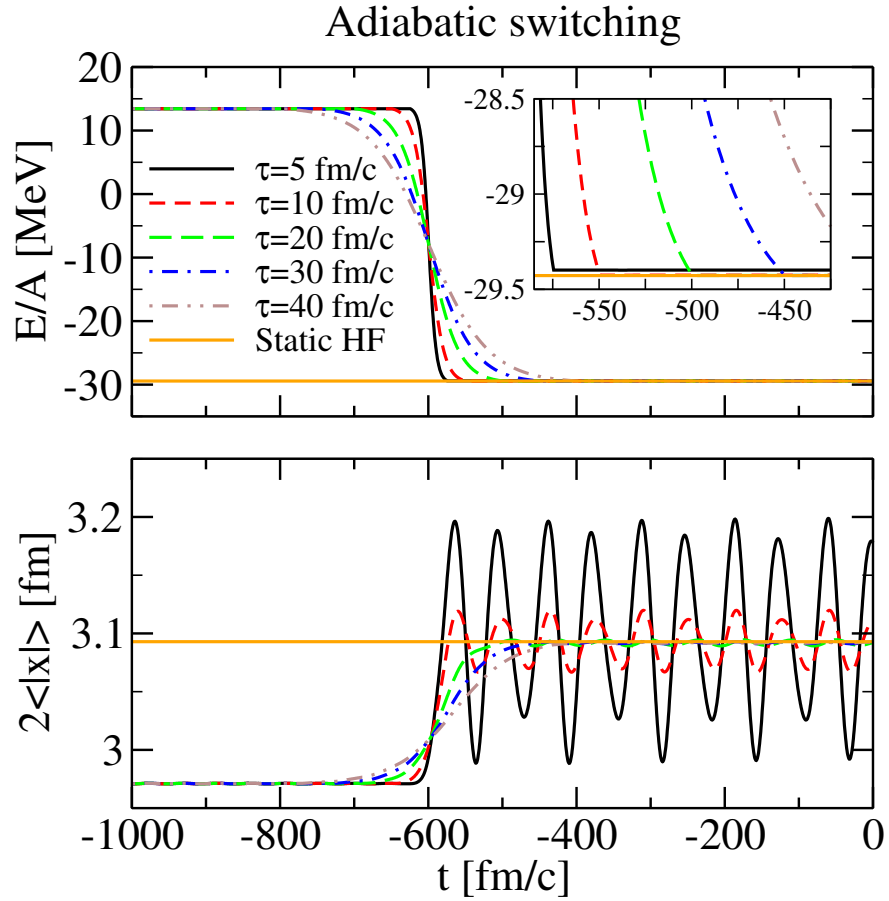
Figure 4.1: Time evolution of the energy per particle (upper panel) and the size of the slab (lower panel) when adiabatically switching from a starting HO configuration to a final mean field state. Different values of the transition time τ are considered. The inset in the top panel shows a magnified portion of the time evolution of the energy. For reference, mean field results from static Hartree-Fock solutions are shown as straight solid (dark yellow) lines.

where ρ_K corresponds to a moving slab with momentum per nucleon $\hbar K$, while ρ_0 is that of a stationary slab. The complete initial state of the colliding system consists of two such slabs moving towards each other.

4.3.2 Dynamics of colliding slabs

In order to explore the importance of the off-diagonal elements of the density matrix, we take as an example the case of colliding nuclear slabs. Here, we examine the dynamics of this collision to provide firm ground to investigate the off-diagonal elements in the next section.

The relatively simple 1D model of nuclear collisions discussed here demonstrates a surprisingly rich range of phenomena [70, 86, 87]. Qualitatively different physical processes are observed within the model when changing the center-of-mass (CM) energy for the reactions. At low collision energies ($E_{\mathrm{CM}}/\mathrm{nucleon} \sim 0.1 - 0.5\,\mathrm{MeV}$), the nuclear slabs fuse into one compound slab that remains excited for long times. For intermediate energies ($E_{\mathrm{CM}}/\mathrm{nucleon} \sim 0.5 - 15\,\mathrm{MeV}$), a fusion process is observed, followed by a break-up into a number of smaller slabs. Higher reaction energies ($E_{\mathrm{CM}}/\mathrm{nucleon} > 15\,\mathrm{MeV}$) yield a pile-up of density at the system center, followed by a violent break-up phase with the formation of a low-density neck. The process is reminiscent of multifragmentation in nuclear reactions and the results of the 3D transport model used in Chapter 3.

We do not explore this wide phenomenology here, but rather focus on one particular case that will highlight the importance of off-diagonal matrix elements in $\rho(x, x')$, since we will be truncating those elements later. Specifically, we concentrate on the collision energy range immediately above fusion reactions. When the two colliding slabs fuse, the compound system is too excited in energy to remain bound and the system undergoes a fission process into three fragments. Because of the symmetry of this specific collision, the final state is formed

$$E_{CM}/A = 4 \text{ MeV}$$
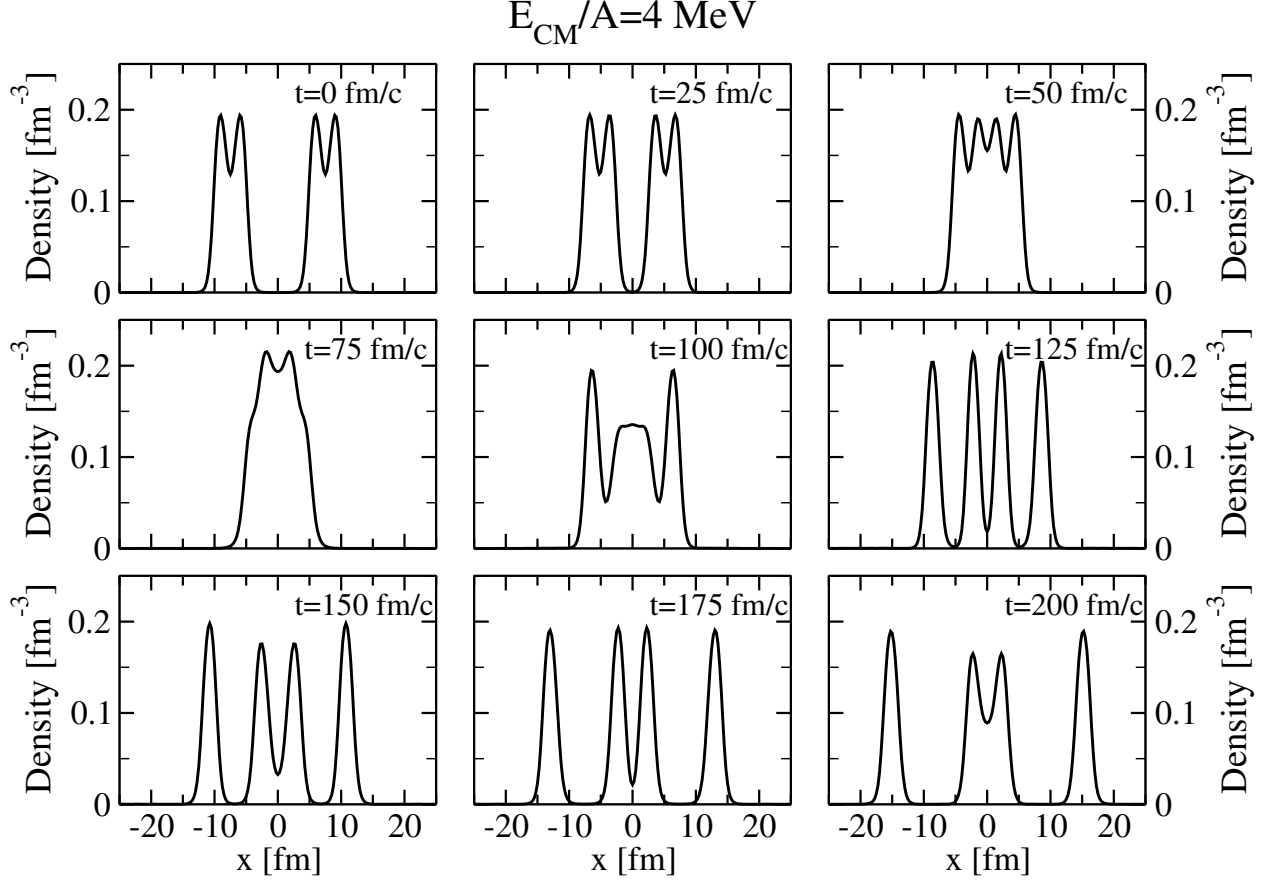
Figure 4.2: Evolution of the center-of-mass density profile for a collision of two $A = 8$ slabs at the collision energy of $E_{cm} = 4 \text{ MeV/nucleon}$.

by a central fragment and two outgoing, identical slabs. Fig. 4.2 provides the snapshots for the time evolution of one such collision at $E_{CM}/\text{nucleon} = 4 \text{ MeV}$. Following the fusion of the original slabs at $t \sim 50 \text{ fm}/c$, two density peaks form at the edges of the compound system and subsequently emerge from the central region to opposite sides. The central region eventually recontracts and oscillates, as it is a highly excited state of an $A \sim 8$ system. The $A \sim 4$ fragments remain excited too, as evidenced in the small changes with time of their central density.

4.3.3 Off-diagonal structure of the density matrix

In order to determine whether we can neglect the far off-diagonal elements in the density matrix, we first investigate how the structures there are created.

At equal arguments in a specific basis, the density matrix ρ of Eq. (4.5) yields the single-particle density in that representation. For example, in the reciprocal basis, $\rho(k, k' = k, t)$ yields the single-particle momentum occupation. At different arguments (*e.g.* $k \neq k'$), the off-diagonal matrix elements reflect correlations between the density at different locations in the domain. As we have discussed earlier, the task of following all the elements in 3D is likely to overwhelm present computer storage capabilities. Nevertheless, the quantities of most direct physical interest, including densities, tend to be associated with either diagonal or near-diagonal elements of the matrix [60]. If the physical system is such that we can safely neglect far off-diagonal elements, NGF calculations would become practical, due to a drastic reduction in dimensionality. We argue that central nuclear reactions are good examples of this, as the late stages involve limited phase coherence between different nuclear fragments.

To examine and quantify the importance of elements far from the diagonal in space representation, let us explore the off-diagonal structure of $\rho(x, x')$ in the same reaction as presented in Fig. 4.2. The upper (lower) panels of Fig. 4.3 show intensity plots for the real (imaginary) parts of $\rho(x, x', t)$ for three different times in the reaction, chosen to represent the initial, overlap and late ("freeze-out") stages. The diagonal of $\mathrm{Re}\{\rho\}$ (upper panels), $x = x'$, coincide with the density profiles displayed in Fig. 4.2. The complex character of the density matrix at initial time reflects the fact that the slabs have been boosted to have a momentum directed toward the center of the system.

To understand off-diagonal structures, it is useful to consider the expansion of the density
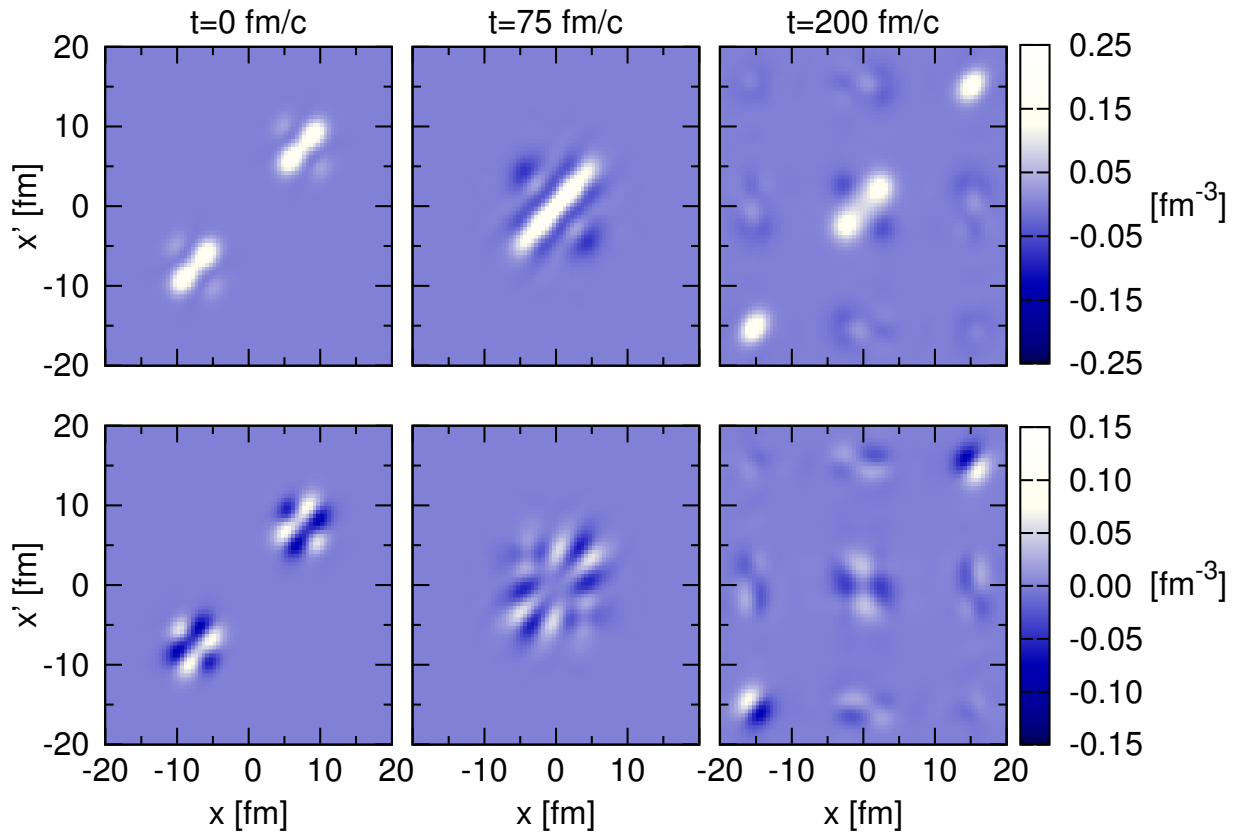
Figure 4.3: Intensity plots representing the real (upper panels) and the imaginary part (lower panels) of the scaled density matrix, $\rho(x, x', t)$, for a collision at $E_{cm} = 4\,\mathrm{MeV/nucleon}$. Off-diagonal correlations develop as the slabs interpenetrate and fragments continue on.

matrix in terms of wavefunctions,

$$\rho(x, x', t) = \sum_{\alpha} n_\alpha \phi_\alpha(x, t) \, \phi_\alpha^*(x', t) \,, \tag{4.11}$$

where n_α is the occupation fraction of the state α. The wavefunctions of the initial slabs are confined to within the size of the slab and, consequently, ρ will have a limited, square support in the (x, x') plane. The left panels of Fig. 4.3 show this structure around the two initial slabs.

At this collision energy, a compound slab is formed (central panel, $75\,\mathrm{fm}/c$) in the center-of-mass. The two outgoing fragments and the central compound system are clearly identified as blobs near the diagonal, $x = x'$. Cross-correlations develop between individual fragments, as signalled by the patches of significant values of the density matrix far away from the $x = x'$ diagonal. As an example, the structure at $(x \sim 0, x' \sim 15)\,\mathrm{fm}$ for $t = 200\,\mathrm{fm}/c$ in Fig. 4.3, both for the real and imaginary parts of the matrix, signal the overlap of single-particle states between the central fragment and the fragment that is leaving in the positive direction. That is, a state that was localized within one of the fragments is now spread between these two fragments, carrying with it its correlated phase.

The discussed correlation patches may be understood in terms of the fragmentation of natural orbitals. Orbitals can have components in each fragment rather than being split among them. Consequently, if those two fragments are in positions x_1 and x_2, when taking the product in Eq. (4.11), one will find non-zero elements of ρ around (x_1, x_2). Physically, this is a reflection of the fact that, during the breakup process, the nucleons from the original orbitals have finite probabilities of ending up in different fragments. The amplitudes for those probabilities maintain a phase relationship leading to correlations in the density matrix. The

entanglement of the internal wavefunctions is thus the sole reason for the persistence of the far-away off-diagonal patches in the density matrix. The real and imaginary parts for those structures are comparable in magnitude, as seen in Fig. 4.3. This points to the involvement of significant relative phases, as expected from the large difference in momentum and position. Note that these entanglement correlations persist for fragments that are $30\,\mathrm{fm}$ apart for the $t = 200\,\mathrm{fm}/c$ panels of Fig. 4.3.

The entanglement between these far-away fragments, represented by the nonzero off-diagonal elements, will only affect the dynamics if the fragments interact again — a consequence of the irrelevance of global phase. In the context of a nuclear collision, this is unlikely, as particles tend to experience a Hubble-like expansion, no longer interacting with particles that have dissimilar momenta. This suggests that perhaps the off-diagonal elements can be safely ignored, leading to truncating them and reducing the computational cost. We test this in the next section.

4.4 Testing importance of off-diagonal elements

Physics beyond the mean-field dynamics (short-range correlations, particle and gamma decays, etc.) are likely to introduce additional decoherence between the separating fragments, beyond that stemming only from different mean-field orbitals. Correspondingly, higher values for the off-diagonal elements are likely to persist more in a mean-field approach than in any simulation with correlations. As a corollary, if one finds out that the far off-diagonal elements may be disregarded within the mean-field dynamics, then it should be even more possible to disregard such elements in more realistic approaches.

To quantify the importance of off-diagonal elements, we want to force them to be zero

at all times and see how it affects the dynamics. This suppression must be done smoothly, however, to avoid the density matrix elements reflected from the suppression and creating spurious oscillations. To acheive this in the evolution, we employ an *ad hoc* procedure based on super-operators[1] that eliminates off-diagonal elements in the time evolution [70]. Fig. 4.4 sketches the spatial structure of the super-operator. White areas, beyond $|x - x'| > x_0 + d_0$, are artificially eliminated at each time step. The remaining blue areas are left unaffected. Note that because we are using a fourier transform to access the momentum space, the structure is periodic in position space. Any operation we perform should preserve this periodicity, thus the lack of suppression at the $(-L, L)$ and $(L, -L)$ corners. Fixing the smoothness factor $d_0 = 2\,\mathrm{fm}$, one can progressively eliminate more and more off-diagonal matrix elements by decreasing x_0. For the break-up reaction explored here, the results of this procedure are shown in Fig. 4.5. Neither the total energy nor its kinetic or potential components (upper panel) are significantly affected by these cuts. The spatial extent of the system, presented in the bottom panel, is also mostly unaffected, pointing towards a good description of the density distribution. Overall, the elimination procedure we have devised indicates that off-diagonal elements play a very small feedback effect on the dynamics.

The off-diagonal suppression procedure we have just presented, though, does not directly involve any savings in terms of storage or CPU time, since though these off-diagonal elements are now zero, we are still using them for computation. The most substantial savings can be achieved by using an alternative spatial discretization scheme in a rotated coordinate frame. With this, we can also control the spareness and lengths of the mesh in the relative coordinate while keeping the average (physical) direction unaffected. This is investigated in

---

[1]A super-operator is an operator that acts on other operators. In this case, it acts on the density operator.
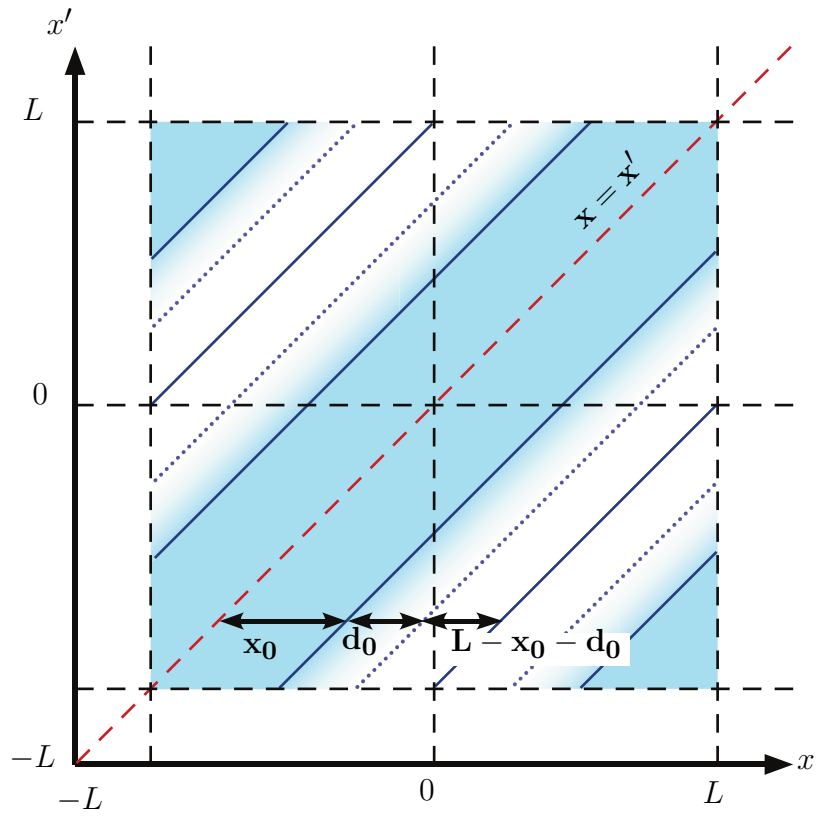
Figure 4.4: Schematic of suppression of off-diagonal elements. White (non-shaded) areas are heavily suppressed. The upper-left and lower-right corners are not suppressed, to preserve periodicity in both coordinates.
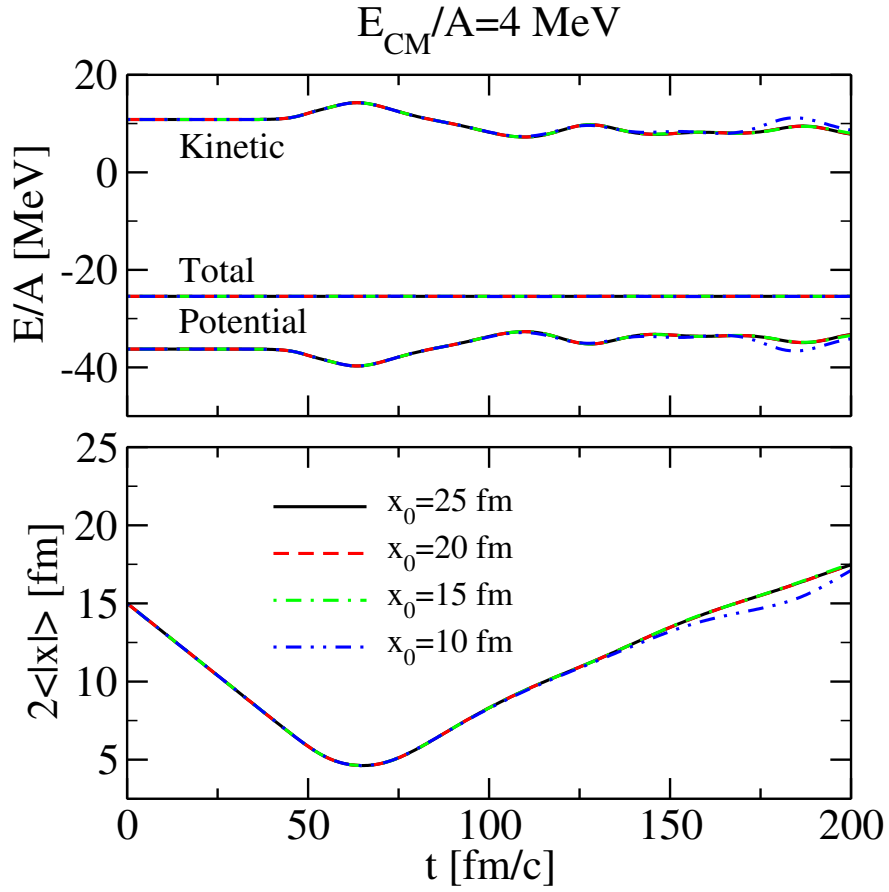
Figure 4.5: Time evolution of the energy per particle (upper panel) and of the spatial extent (lower panel) in a collision between 1D nuclear slabs at $E_{CM}/\text{nucleon}= 4\,\text{MeV}$, for different values of the cutoff parameter x_0 at fixed smoothness $d_0 = 2\,\text{fm}$.

the next section.

4.5 Rotated density matrix

Now that we've shown that the far off-diagonal elements of the density matrix can safely be suppressed, we describe a technique to practically truncate the matrix in the off-diagonal direction by recasting it into a rotated coordinate frame. We also show how this rotation partially decouples the position and momentum discretization, permitting access to arbitrary regimes of kinetic energy without altering the resolution and range of the 1D box in position space. First we provide justification for why it is helpful to rotate the coordinate system, rather than simply rewrite the Fourier transforms.

Naively, in order to not compute the unnecessary off-diagonal regions of the density matrix, we could rewrite the Fourier transform code to simply not consider them. If we used an off-the-shelf FFT library, then each row would also have a different periodicity, since each row has a different range. However, much work has gone into making FFT libraries very efficient, especially for rectangular multi-dimensional transforms. Therefore, our first step is to set up a rectangular density matrix, with one of the directions being the direction that we truncate. The next step, not explored here, would be to use parallel processing FFT implementations. Adaptive Mesh Refinement (AMR) should also be explored, so as to only compute important regions, irrespective of where they lie in the density matrix.

To be able to truncate in this way, we need one direction of the grid to be in the off-diagonal direction of the (x, x') matrix. As one travels in this direction away from the $x = x'$ diagonal, we notice that $|x - x'|$ increases, while $(x + x')$ remains constant. This suggests that a convenient coordinate system would be the average and relative coordinates, which we call x_a and x_r, respectively. Note that this is not a transform into a center-of-mass system, since x and x' refer to different positions of the same object. In this new representation, the

line that gives the probability density is now $x_r = 0$, compared to $x = x'$ in the previous coordinate system.

4.5.1 Fourier transform in the new coordinates

In the unrotated, (x, x') system, the transform to momentum space takes the form

$$\rho^{(k)}(k, k') = \frac{1}{2\pi} \int dx \, dx' \rho(x, x') e^{-ikx} e^{ik'x'} \tag{4.12}$$

The second exponential factor has no negative sign in the argument, tied to the fact that the density matrix is hermitian-symmetric under exchange of position or momentum arguments, $\rho(x, x') = \rho^\dagger(x', x)$. The $1/(2\pi)$ prefactor is in both the transform and inverse transform, in order to produce the suitably normalized probability density in momentum space.

In the rotated, (x_a, x_r) system, we make the substitutions

$$q_a = \frac{q + q'}{2}, \quad q_r = q - q', \tag{4.13}$$

where q represents x or k. Since these are not actually center-of-mass and relative coordinates of a 2-particle system, we do not need to ensure that k_a is the conjugate of x_a. Therefore, we are free to choose $1/2$ as a factor in both of those coordinates. This allows a straightforward interpretation of x_a as the "physical coordinate" — that is, if $q_r = 0$, then q_a gives the physical position or momentum, where q stands in for x or k in turn.

Substituting these coordinates in Eq. 4.12, we arrive at the transform

$$\rho^{(k)}(k_r, k_a) = \frac{1}{2\pi} \int dx_a \, dx_r \, \rho(x_a, x_r) e^{-ik_a x_r} e^{-ik_r x_a} . \tag{4.14}$$

This substitution gives a new transform that is identical in structure to the previous one, making it amenable to direct use of FFT libraries. Note that x_r (x_a) transforms into k_a (k_r).

4.5.2 Discrete Fourier transform

Since we are assuming periodic boundary conditions in position space, this creates a discrete spectrum of allowed momenta, the resolution Δk being inversely proportional to the length of the periodic box in position space, $x_{\max}$. Further, as we are approximating a continuous space with a discrete position basis with a finite number of positions, there is a maximum momentum, $k_{\max}$, that can be described by the calculation, inversely proportional to the resolution in position space, Δx (the closer together the positions are, the more-quickly-varying density can be described, which corresponds to a higher momentum). These relations are true for both x and x'. In particular, for a box that has a length $2x_{\max}$, the relations are

$$\Delta k = \frac{\pi}{x_{\max}}, \quad k_{\max} = \frac{\pi}{\Delta x}, \tag{4.15}$$

and similar for $\Delta k'$ and $k'_{\max}$. Note that this is for the choice of position range $-x_{\max}$ to $x_{\max}$ and momentum range $-k_{\max}$ to $k_{\max}$.

In the rotated system, k_a (k_r) is conjugate to x_r (x_a) in the Fourier transform, and the relations become

$$\Delta k_{a(r)} = \frac{\pi}{x_{r(a)}^{(\max)}}, \quad k_{a(r)}^{(\max)} = \frac{\pi}{\Delta x_{r(a)}}. \tag{4.16}$$

Thus, we can independently vary the resolution and range of x_a and k_a, by modifying the characteristics of the relative coordinates. In the unrotated system, for a given size in position

84

space, for increasing the maximum momentum, the computational storage scales as $(DN)^2$, where D is the number of physical dimensions and N is the number of grid points in each x and x' direction (for an $N \times N$ density matrix). In this rotated system, one can vary the number of points in the relative direction independently, making the computational storage scale as (DN) for an increase in maximum momentum described by the system.

4.5.3   Testing the rotated matrix

To validate the method, we first obtain exactly the same results as in the unrotated case. In order to perform exactly the same operations, we must match the periodic of the original system. This periodicity, illustrated in Fig. 4.6, is such that $\rho(x, x') = \rho(x + 2x_{\max}, x') = \rho(x, x' + 2x_{\max})$. In this schematic example, we give a physical system that consists of a large and small slab, represented as filled circles centered on the diagonal. The circles could represent quantum harmonic oscillator states. There is a correlation between them (a non-zero phase factor), as evidenced by the fainter ellipses in the far off-diagonal region. We show this assymetric, correlated system to provide orientation throughout the following rotation and subsequence truncation in the relative direction.

When rotated into (x_a, x_r) coordinates, we select an area that is a) rectangular, to be convenient for the FFT, and b) is periodic in both the average and relative directions. Fig. 4.7 shows our choice.

However, this area is twice the original area, hence twice the computational storage of the original matrix (and over twice the computation time for the FFT). This is because the orginal (x, x') matrix appears twice in the rotated one. The maximum extent in x_r is $x_r^{(\max)} = 2x_a^{(\max)}$. In Fig. 4.8, regions with the same pattern are representing the same region of the unrotated matrix. Using this duplication, we rewrite the Discrete Fourier Transform
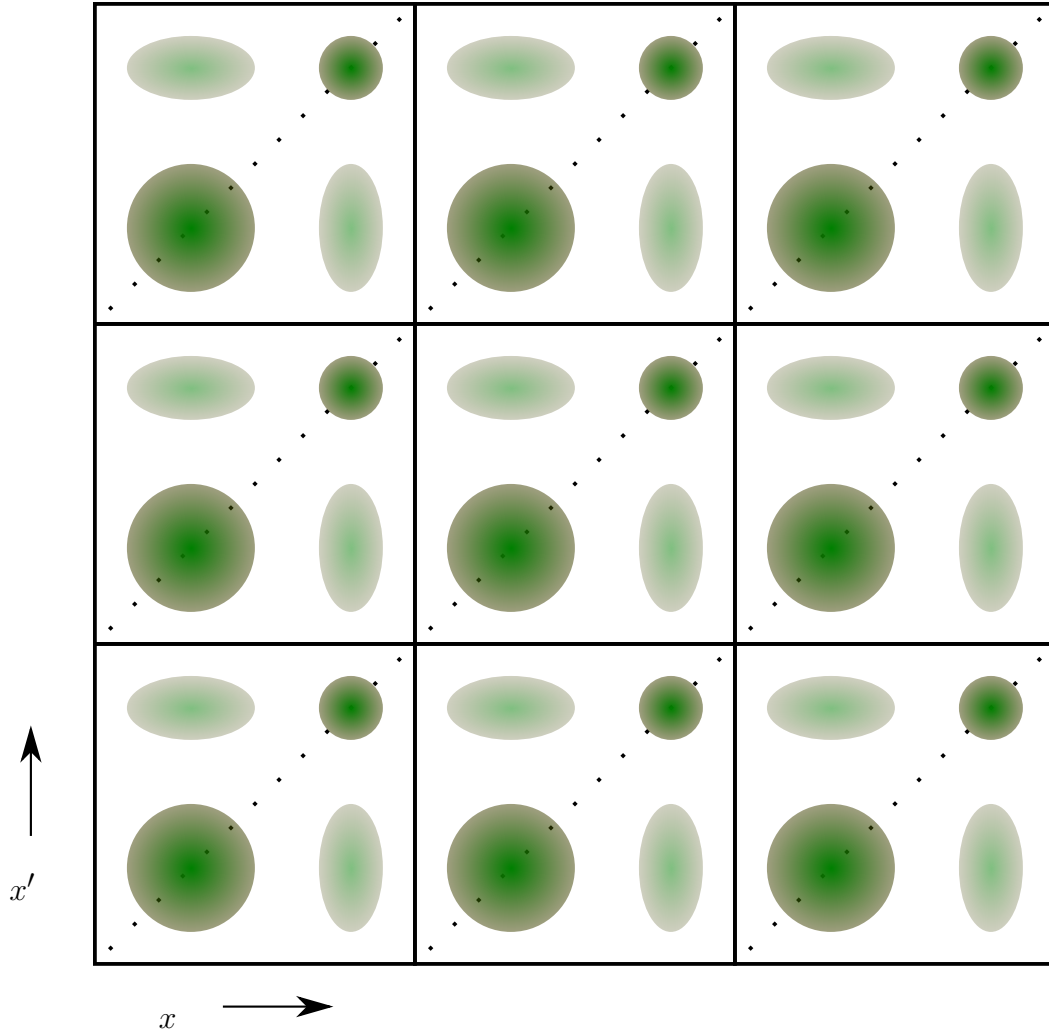
Figure 4.6: Schematic of density matrix in (x, x') coordinates, with example of periodic boundaries and the resulting physical system that is simulated. Each square contains an identical copy of the physical system.
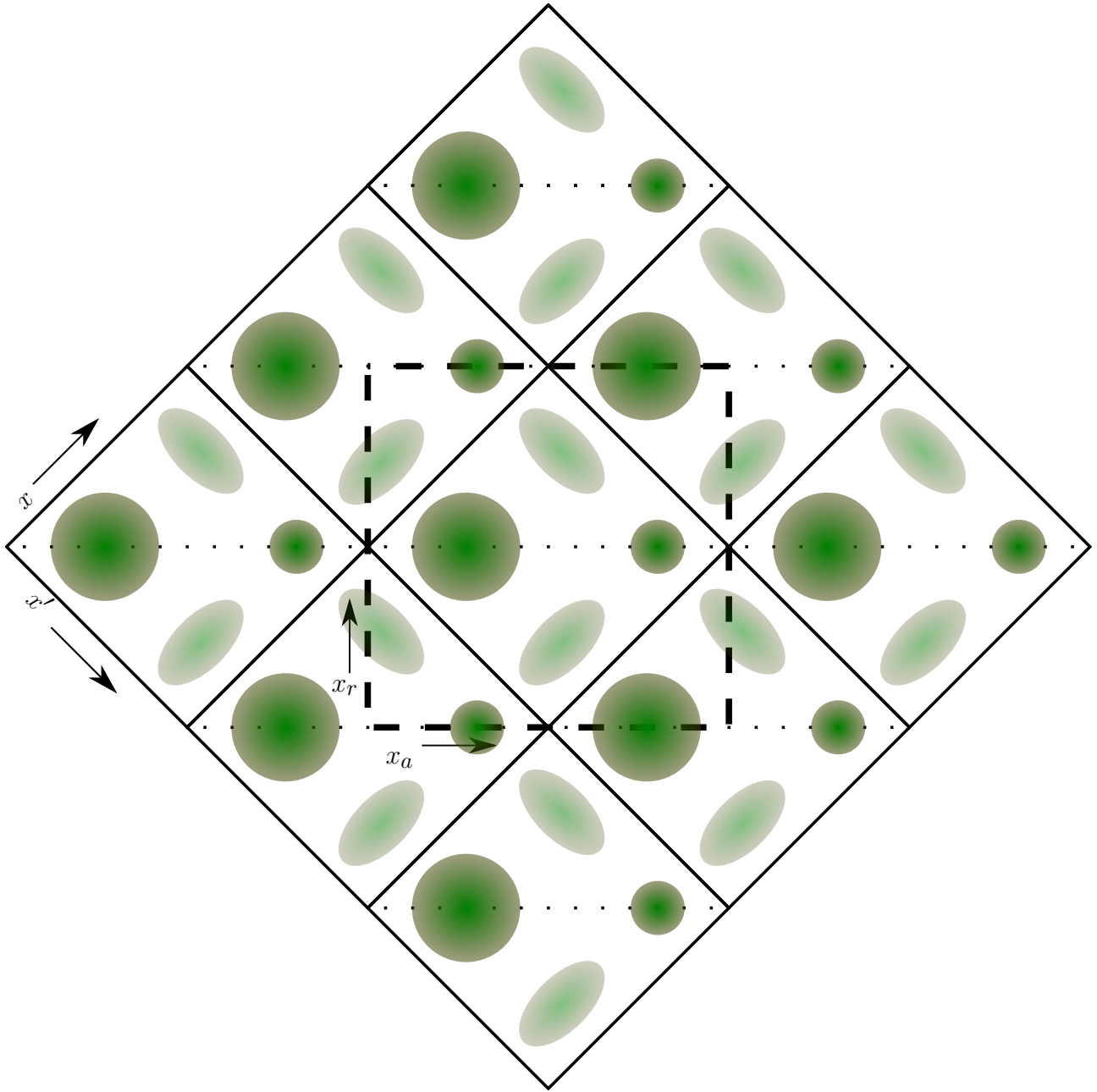
Figure 4.7: With the density matrix rotated, the smallest rectangle that is periodic in both the average coordinate (left-to-right) and relative coordinate (down-to-up) is marked in dashed lines.

(DFT) to span only the innermost 4 rectangles, reducing the maximum extent in the relative direction to $x_r^{(\max)} = 2x_a^{(\max)}$, producing the rectangle in Fig. 4.8 that is bounded in the x_r direction by dot-dashed lines.

However, this configuration leads to a surprising result — in momentum space, $\rho^k(k_r, k_a)$, every grid point where the sum of the indices, $k_a + k_r$, is odd, the density is identically zero, creating a checkerboard pattern. In the derivation, this results from a factor in the DFT, $[1 + (-1)^{k_a + k_r}]$, that appears when the duplicated density matrix from Fig. 4.8 is rewritten as a non-duplicated sum. Conceptually, this can be seen to arise from the rotation itself, as seen in Fig. 4.9.

We remove this duplication by separating the Fourier transform into two — one for even k_r and k_a, and one for odd. These transforms do not communicate between each other, and so the $N \times N$ Fourier transform is reduced to two $N \times N$ transforms, regaining the original order of computational cost.

With this work done, we now have a rotated density matrix that can be computed with the same computational cost as the original. Now we can perform the work we set out to do at the beginning of this chapter — reduce the computational cost by truncating the matrix in the x_r direction.

Fig. 4.10 illustrates the implementation. In the left-most panel, the suppression of far-off-diagonal elements is displayed. Again, a smooth transition to total suppression is used, seen by the shading (blue) gradient in the figure. The resulting suppression of the original (x, x') density matrix in Fig. 4.10b (due to the duplicated regions described earlier) can be compared to Fig. 4.4, showing that the suppression is identical, leaving the corners of large $|x - x'| = |x_r|$ unsuppressed. To perform the actual truncation, we simply reduce the extent of the matrix in the x_r direction, producing the matrix bordered with a dot-dashed line in
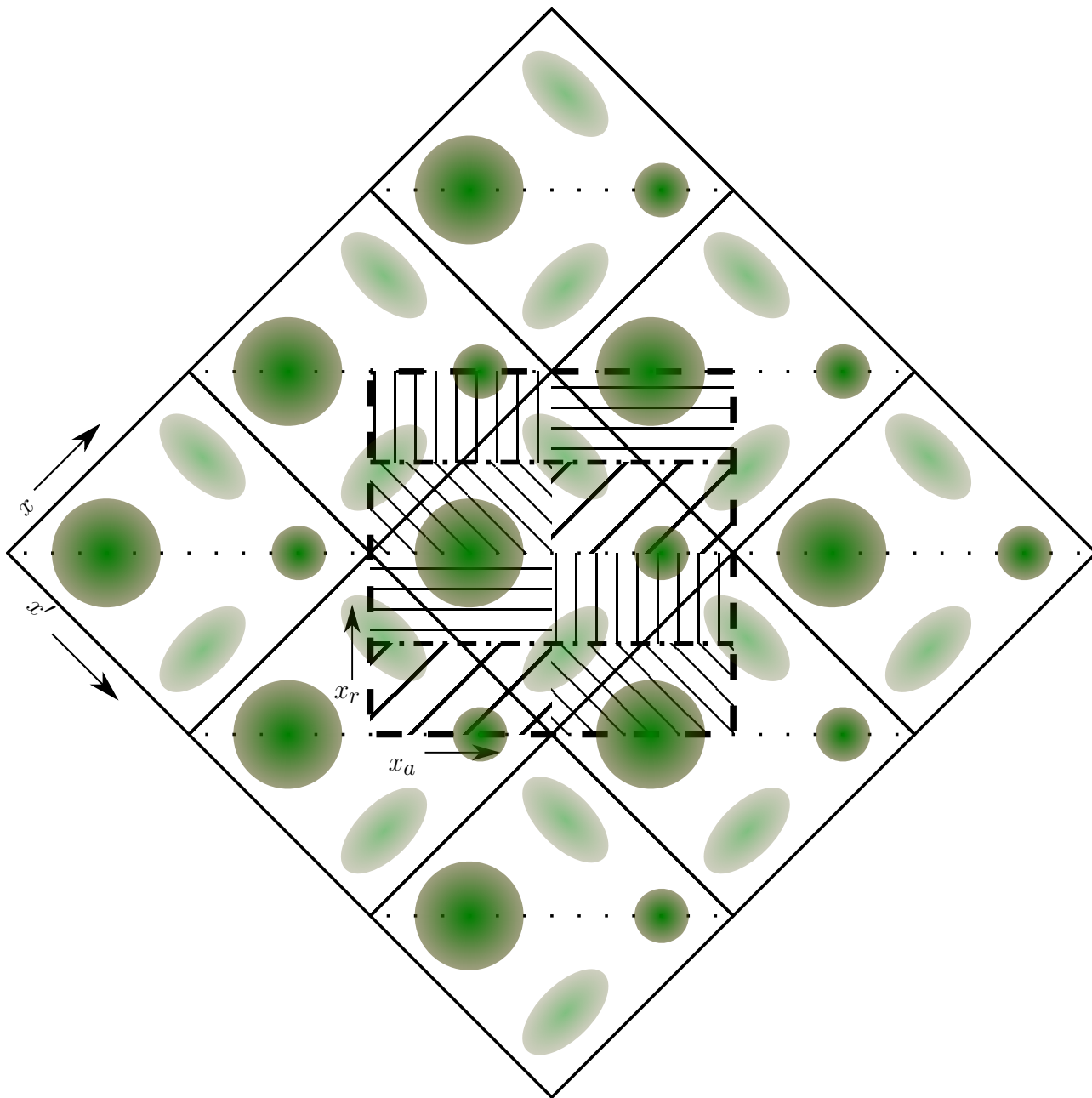
Figure 4.8: Schematic illustrating duplication of original density matrix. Regions with the same pattern have the same exact part of the unrotated (x, x') density matrix in them.

(a) unrotated   (b) rotated   (c) extra zeroes
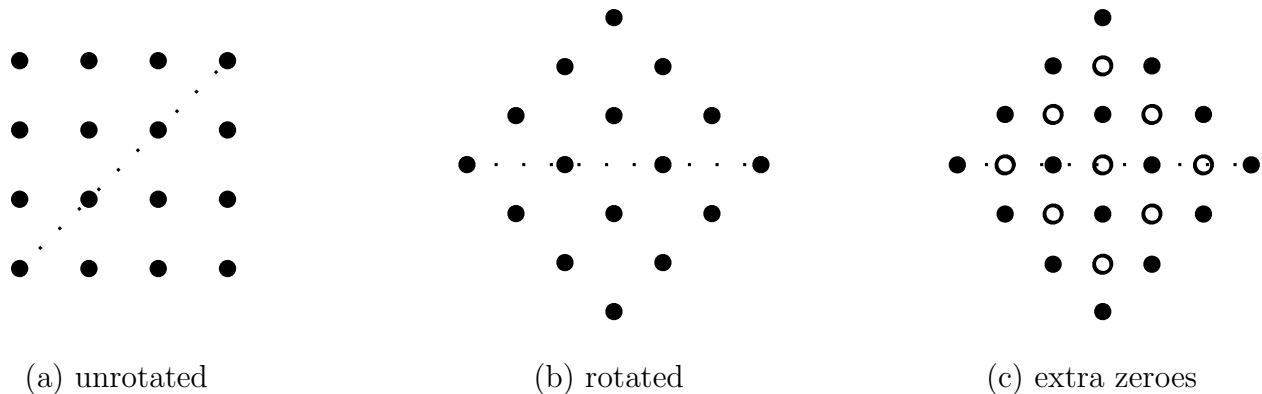
Figure 4.9: Rotation of matrix and creation of fictitious points. The $x = x'$ line is shown as a dotted line, for orientation ($x_r = 0$ line in rotated system). When the matrix in (a) is rotated into (b) and the system is modeled with a rectangular Fourier transform, extra grid points are created, shown as open circles in (c).

the right-most panel. The duplicated regions, bordered with dashed lines, are still modeled, since they are duplications of the computed matrix.

Here, there is a complication regarding the use of stock FFT libraries. The standard DFT is

$$\tilde{f}_k = \sum_{j=-N/2}^{N/2-1} f_j e^{-i2\pi jk/N} \tag{4.17}$$

If we reduce the extent in x_r without changing the number of points, then the DFT remains the same and we get the exact result compared to the suppressed, untruncated case. Since this increases the resolution in x_r, the maximum momentum $k_a^{(\mathrm{max})}$ is increased and we can access higher energy regimes without increasing the computational cost. However, if we want to change the number of points while keeping the DFT the same, we run into a problem. If we reduce the number of points by a factor ν and only change the range of indices in the

(a) suppressed regions   (b) periodic view   (c) matrix truncation
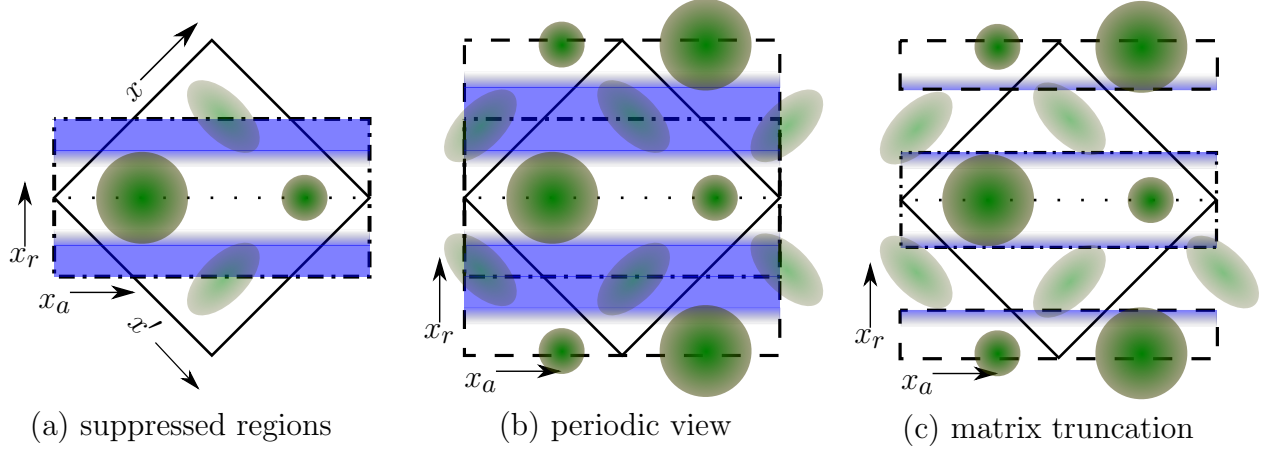
Figure 4.10: Implementation of off-diagonal (x_r-direction) suppression. Suppressed areas are blue (shaded). Implementation is in (a), while the resulting suppression of the original density matrix shown in (b) (compare to Fig. 4.4). Truncation of the matrix is shown in (c), with the computed matrix bordered with a dot-dashed line and periodic extensions shown with dashed borders. The empty space is not computed at all, reducing the computation cost. This benefit is amplified geometrically with an increase in the number of dimensions.

transform, while keeping Δx the same, we get

$$\tilde{f}_k = \sum_{j=-\nu N/2}^{\nu N/2-1} f_j e^{-i2\pi jk/N} \tag{4.18}$$

However, if we feed these νN points to a stock DFT algorithm, it will compute

$$\tilde{f}_k = \sum_{j=-\nu N/2}^{\nu N/2-1} f_j e^{-i2\pi jk/(\nu N)} \,, \tag{4.19}$$

thus raising each phase factor to the power $1/\nu$. Until we learn how to rewrite this in the standard form, we resort to using our own Fourier transform algorithms. Since Fortran 95 introduced built-in, optimized matrix multiplication routines, there is not a large sacrifice in computation time.

We have shown how to practically truncate the density matrix to reduce the computational cost. This method also results in the ability to tune independently the resolution and

91

range of position and momentum. In the next section, we show a practical application of this 1D density matrix time evolution in modeling the Bose-Einstein condensate (BEC).

4.6 Bose-Einstein Condensates

Before moving to a 3D simulation or adding correlations (both are beyond the scope of this thesis), we demonstrate the use of this code in a physical 1D quantum system, in particular the Bose-Einstein condensate (BEC).

A BEC is a collection of bosons, the majority of which are in the same ground state. In magneto-optical trap (MOT) experiments, there are typically $\gtrsim 10^4$ atoms in this ground state, their wavefunction spread out across $\sim 0.1 \, \text{mm}$. An ideal BEC has all of the particles in the ground state. This occurs below a certain critical temperature associated with Bose statistics.

In this section, we first describe the mean field model for BECs. Then, we use the density matrix formalism developed in this chapter to find the ground state of that model to find the density distribution of the BEC ground state.

4.6.1 Modeling with the Gross-Pitaevskii equation

The mean field description of the BEC is given by the Gross-Pitaevskii equation (GPE) [88]. This models a dilute gas of atoms interacting with a contact potential, with particles moving slowly enough to only scatter with binary s-wave interactions. The resulting equation is the Schrödinger equation with a potential term that is linearly dependent on the density. And since the condensate is all in one quantum state, a single wave function can be used to

describe all the atoms,

$$\left\{ -\frac{\hbar^2}{2m}\nabla^2 + V_{\text{ext}}(\mathbf{r}) + g\,|\phi(\mathbf{r})|^2 \right\}\phi(\mathbf{r}) = \mu\phi(\mathbf{r})\,, \qquad (4.20)$$

where $V_{\text{ext}}(x)$ is an external potential, typically a harmonic oscillator trapping potential, and g is the interaction strength. g is dependent on the s-wave scattering length a_s and the mass m of the particle, $g = 4\pi\hbar^2 a_s/m$.

For a 1D condensate, an elongated trap is used, where a steep potential is created in 2 perpendicular directions, called transverse or radial (HO with frequency $2\pi\omega_\perp$), and a much shallower potential is used in the third, longitudinal direction (frequency $2\pi\omega_z$). Due to this anisotropy, excitations in the transverse direction are limited to zero-point fluctuations, and thus the dynamics in the transverse direction are frozen.[2] When these directions are integrated over, we arrive at the 1D GPE,

$$\left\{ -\frac{\hbar^2}{2m}\frac{\partial^2}{\partial^2 x} + V_{\text{ext}}(x) + g_{1\text{D}}\,|\phi(x)|^2 \right\}\phi(x) = \mu\phi(x)\,, \qquad (4.21)$$

where $g_{1\text{D}} = 2a_s\hbar\omega_\perp$ [89]. Thus, the interaction potential is dependent on the number of particles in the trap, unlike in the 3D case.

In general, this equation cannot be solved analytically. In the Thomas-Fermi approximation (the limit where potential energy is much greater than the kinetic energy) and with a harmonic oscillator external potential $V_{\text{ext}}(x) = (1/2)m\Omega^2 x^2$, the kinetic term is neglected,

---

[2]Strictly speaking, this is a so-called *quasi*-1D condensate, as the critical temperature for condensation in 1D tends to zero (see Appendix C).

and the probability density of the ground state is an inverted parabola,

$$|\psi(x)|^2 = \begin{cases} \dfrac{1}{g}\left(\mu - \tfrac{1}{2}m\omega^2 x^2\right) & , \quad |x| < \sqrt{\dfrac{2\mu}{m\omega^2}} \\[2em] 0 & , \quad \text{otherwise} \end{cases} , \tag{4.22}$$

the piecewise continuous function being necessary to preserve the positive-definiteness of the probability density. Note that this sudden change in the wave function in position will cause an extended population of momentum states. The practical effects of this are addressed in a following section.

For the case where the Thomas-Fermi equation does not appply, a numerical method to arrive at the ground state must be used. We use the adiabatic switching technique described in Section 4.3.1. For this technique, we start with a wave function and potential that is analytically solvable. Since most BECs are produced and contained in a harmonic oscillator potential produced by a magneto-optical trap (MOT), we use this as our external potential. An intuitive choice for the initial, analytic potential would be the bare harmonic oscillator potential, with no density dependent interaction term. To minimize the number of switching steps required, we select by eye the initial HO frequency that results in a similar physical extent of the system as the final, density-dependent potential, as measured by $\langle |x| \rangle$. Another method would be to variationally solve for the frequency of the harmonic oscillator potential whose ground state (a Gaussian) has the lowest energy in the final, density-dependent potential. The resulting Gaussian width, σ, can be solved iteratively with

$$\sigma = \sqrt[4]{\frac{1}{m\omega_z}\left(\sqrt{\frac{2}{\pi}}\, g_{1D}\, \sigma + \frac{\hbar^2}{2m}\right)} \tag{4.23}$$

and the HO frequency is given by $\Omega_{\text{HO}} = \hbar/(\sigma^2 m)$.

To do this, we need to choose a physical system, preferably one that has been experimentally realized. We choose for our system a gas of ultracold ^{87}Rb atoms, placed in an elongated trap so as to be nearly one-dimensional and thus describable by our 1D code [90]. ^{87}Rb has an s-wave scattering length of $a_s = 5.29$ nm. Since it is positive, the interaction is repulsive, and thus we need a trapping potential to contain them and actually form the condensate. The trap frequencies used in the experiment were 840 Hz in the transverse (radial) direction and 14 Hz in the longitudinal (axial) direction. With a trap potential anisotropy ratio of $\omega_r^2/\omega_a^2 = 3600$, this is a clear candidate for the use of the 1D simulation — there will be a large spectrum of excitations in the axial direction before any radial excitations are produced.

4.6.2   Initial state

To produce the ground state of the BEC, we considered several different initial, analytic potentials for which we could calculate the ground state. These included the infinite square well, finite square well, harmonic oscillator, and Kronig-Penney model. The finite square well and harmonic oscillator (HO) have the disadvantage that they are not periodic, while our system is assumed to be periodic through our use of the Fourier transform. The infinite square well, while not strictly violating periodicity, does not lend itself easily to adiabatically switching to a different, finite potential. The Kronig-Penney model is perhaps the potential that gives a ground state best suited to the periodic nature of our system. This potential is a periodic system of rectangular potential barriers. Thus, the ground state is that of the infinite periodic system that the Fourier transform assumes, and thus the ground state of the Kronig-Penney model should be closer to our true ground state than the ground state of

other, nonperiodic potentials.

In the end, however, the Kronig-Penney ground state is complicated and not as intuitive as that of the HO, so we use the HO potential, in order to manipulate it by hand more easily. Its nonperiodic nature is not so relevant, since its ground state density is effectively zero near the edges of the box.

The system of ^{87}Rb atoms described in the previous section was realized experimentally with 5×10^5 atoms. To discover what the resolution and range for position and momentum should be to maintain a stable evolution, we start simulating the system with just 1 particle, then increase the number of particles in subsequent trials, since the interaction potential is dependent on the number of particles N, as seen in Eq. 4.21. To maintain a similar shape of the resulting condensate across different numbers of particles, the trap frequency is proportionally reduced, keeping constant the ratio ω_z^2/N and thus the shape of the potential.

To verify that the system smoothly transitioned to the new ground state, we examine how the energy and spatial extent vary over time, shown in Figs. 4.11 and 4.12. For a very small number of particles, $N = 256$, the resulting system is quite stationary, the energy varying by about 0.6% over 1 s and the spatial extent varying by about 2% over 1 s at the end of the adiabatic switching. Given that the relevant timescale of dynamics is $\sim 1\,\mathrm{ms}$, this is a very good approximation of the ground state. For greater numbers of particles, with a matching increase in the trapping potential, the resulting ground state is less stationary, with the spatial extent varying by about 3% over 0.5 s. As N increases and the trapping potential frequency increases, we must adjust the position and time discretization to obey stabilty constraints (see Appendix D).

We satisfy the momentum-space stability constraint in Eq. D.4 for the BEC ground state found in the previous section. For that system, we also satisfy the position-space constraint,
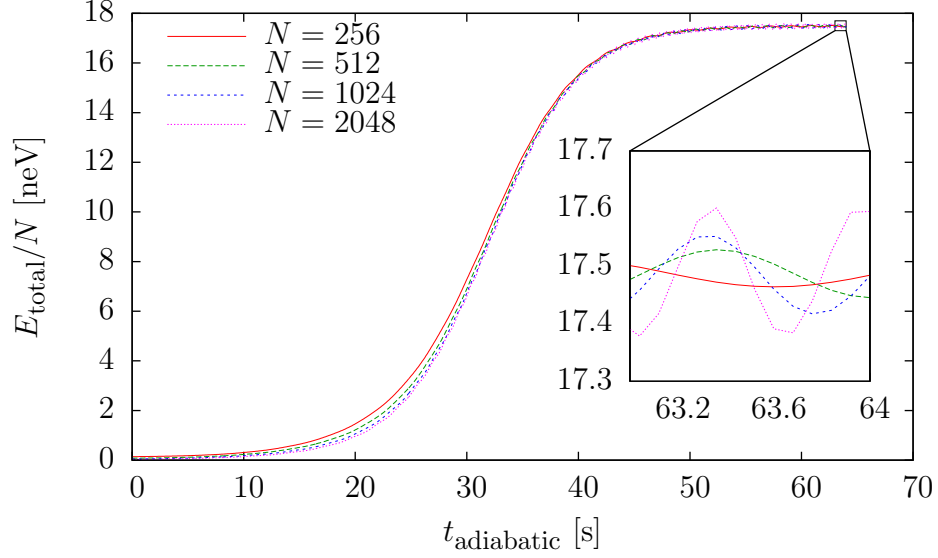
Figure 4.11: Total energy of system while adiabatically switching from an external HO potential to the Gross-Pitaevskii potential. A reasonably stable energy is reached as the number of atoms in the condensate, N, increases. However, as seen in the inset, as N increases, the total energy exhibits an increasing oscillation, suggesting higher excitations.
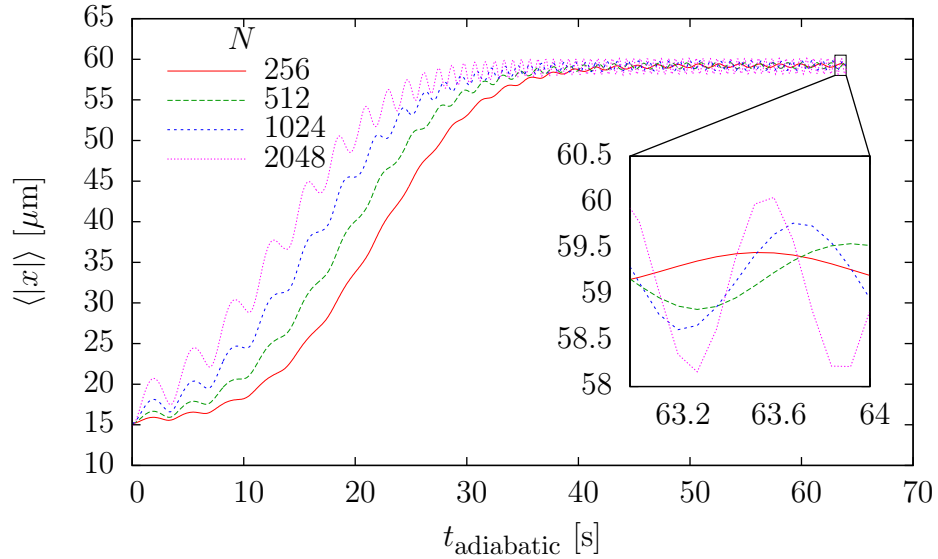
Figure 4.12: Extent of system in position space while adiabatically switching from an external HO potential to the Gross-Pitaevskii potential. The ground state is more closely reached for a fewer number of particles in the condensate, as seen by a slower, lower-amplitude oscillation at late times than for larger numbers of particles.

Eq.D.5, for $N \lesssim 50$. As N increases, we increase the trap frequency Ω to maintain the same shape of the potential. If Ω and N were to be increased to match the experiment described, with $\Omega = 2\pi \times 14\,\mathrm{Hz}$ and $N = 5 \times 10^5$, the position-space constraint would be exceeded by 7 orders of magnitude, and satisfying this constraint would require a substantial change in x_{max} and Δt, potentially to degrees that unacceptably increase the computational cost. This is migitated, somewhat, by the fact that the BEC never reaches the edge of the grid, and thus it never experiences the maximum potential. If it only approaches, for example, half the distance to the edge, then this would relax the position-space constraint by a factor of 4. Still, more work needs to be done to allow the increase in particle number to the typical size of experimentally realized condensates.

Fig. 4.13 shows the probability density $\rho(x) \equiv \rho(x, x' = x)$ before and after the adiabatic switching procedure. During the switching, the external HO transitions to a higher frequency, and the density dependent potential turns on, pushing the density to spread out. In this stationary system, with large N, the potential energy is much higher than the kinetic, resulting in the applicability of the Thomas-Fermi approximation, with the solution for the density given in Eq. 4.22 — an inverted parabola. In fact, this is the shape that is seen in the figure, except for the edges of the parabola. Analytically, the Thomas-Fermi solution is piecewise continuous here, with an undefined first derivative. Such a sharp change in the density in position space would be represented as an infinite sum of waves in momentum space, akin to the Fourier series of a square wave. Because of our finite grid, and a limited maximum momentum, sharp boundaries cannot be represented. Instead, the edge becomes softened, as seen in the inset in Fig. 4.13.

The 2D density matrix $\rho(x, x')$ is shown in Fig. 4.14, both before and after the adiabatic switching. During the switching, the amplitude spreads in both the average direction, $(x +$
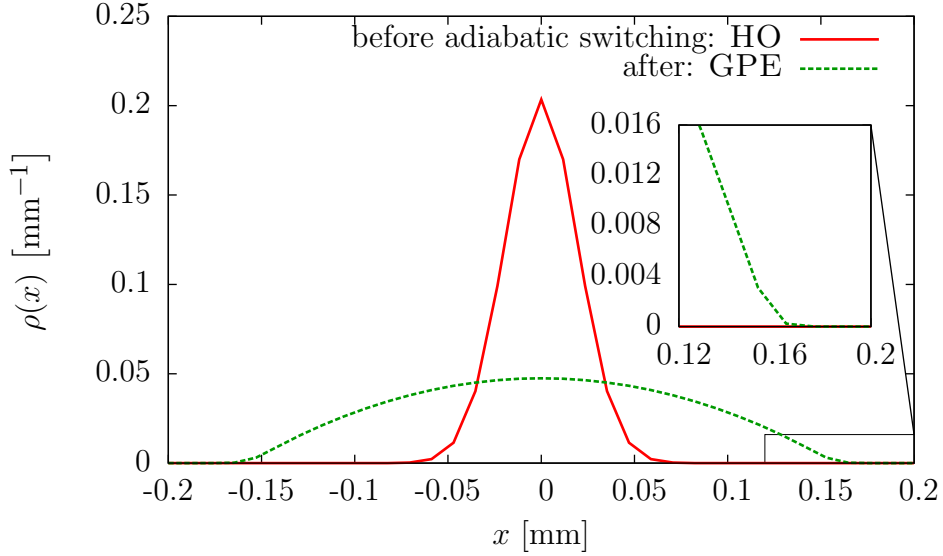
Figure 4.13: Probability density at beginning (solid line, red) and end (dashed line, green) of adiabatically switching from the harmonic oscillator potential to the Gross-Pitaevskii potential. Since the potential energy is much stronger than the kinetic, the resulting distribution is the Thomas-Fermi approximation, an upside-down parabola, as in Eq. 4.22. The transition between the parabola and zero density, seen inset, is smoother than the piecewise continuous solution and more realistic.

$x')/2$, and relative direction, $x - x'$. The circular support for the HO state has shifted to a square-shaped support for the GPE state. The square shape means that the more distant regions of the density (the upper right and lower left regions of density matrix) have a stronger correlation with each other than in the HO case. This makes sense for a BEC since the whole system is one coherent macroscopic state.

(a) HO　　　　　　　　　　　　　　　(b) GPE
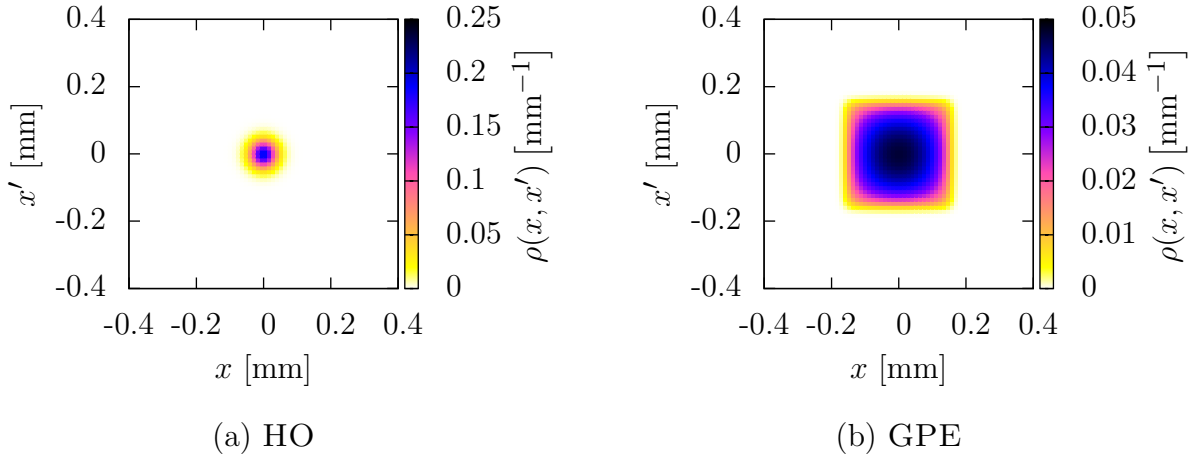
Figure 4.14: Density matrix for (a) the analytic harmonic oscillator ground state before adiabatic switching and (b) after adiabatic switching to the Gross-Piteavskii equation, yielding the Bose-Einstein Condensate. The local density lies along the diagonal $x = x'$, shown in Fig. 4.13. The square support in the BEC shows a stronger correlation between distant regions of the condensate, exhibiting stronger long-range coherence than in the HO case.

4.7   Conclusion

With the goal of eventually describing 3D nuclear collisions including correlation effects beyond the mean field with the Kadanoff-Baym equations, we have developed the apparatus to simulate 1D systems in the mean field limit, showing that we can successfully reduce the computational cost of the calculation by truncating the density matrix in the off-diagonal direction. We used this model to describe 1D Bose-Einstein Condensates, thus using the model to describe physical phenomena across 15 orders of magnitude in energy.

Chapter 5

Conclusion

In this thesis, we have simulated the time evolution of quantum many-body systems and used comparisons to experimental data in order to learn more about the properties of nuclear matter, understand better the dynamical processes in central nuclear collisions, and advance the development of a nonequilibrium Green's function description of both central nuclear collisions and Bose-Einstein Condensates.

In Chapter 2, we determined the viscosity of nuclear matter by adjusting the in-medium nucleon-nucleon cross section ($\sigma_{\mathrm{NN}}^{\mathrm{(med)}}$) in a BUU transport model, using theory-motivated reductions, until the simulation results matched experimental data on nuclear stopping. Then we used that cross section to calculate the viscosity self-consistently. We confirmed that it is necessary to reduce the $\sigma_{\mathrm{NN}}^{\mathrm{(med)}}$ to agree with experiment. Using our new viscosity determination, we showed that the ratio of shear viscosity to entropy density, η/s, of nuclear matter in intermediate energy collisions follows a trend that is qualitatively consistent with results from collisions at relativistic energies.

In Chapter 3, we used the same BUU transport model as in the previous chapter to isolate the protons emitted early in a central nuclear collision at intermediate energy, as predicted in the model, using a filter on high transverse momentum. We predicted that there is a detectable effect that this filter has on the experimentally observable source function. Then we explored the prediction of a recontraction of protons at late times in the central collision of $^{112}\mathrm{Sn} + ^{112}\mathrm{Sn}$ at $50\,\mathrm{MeV/nucleon}$ that results in a secondary emission of protons. We

showed that the existence of this reemission would be detected by how the source function changed with the filter on high transverse momentum.

In Chapter 4, we developed an early implementation of a more fully quantal transport model, with our sights set on solving central nuclear collisions in 3D using nonequilibrium Green's functions. In our 1D, mean field approximation, density matrix model, we demonstrated the initial state preparation and collision of 1D nuclear "slabs", showing the successful ground state calculation and qualitative features of low-energy nuclear collisions. With the aim of reducing the computational cost of the calculation, in anticipation of more dimensions and costly correlations, we showed that we can neglect far off-diagonal elements in the density matrix, exploiting the proximity of the nuclear system to the classical limit, without afffecting the one-body observables.

Further, we described a method of recasting the density matrix in a rotated coordinate system, enabling us to not only ignore the irrelevant matrix elements in the time evolution, but also avoid computing them completely, reducing the computational cost. As an added benefit, we found that the rotation allows us to partially decouple the position and momentum discretization, permitting access to arbitrary regimes of kinetic energy without altering the resolution and range of the 1D box in position space. Finally, we exhibited the wide applicability of this density matrix approach by applying it to a system of 2000 ultracold ^{87}Rb atoms in a Bose-Einstein condensate, as described by the Gross-Pitaevskii equation, successfully acheiving a stable state in a harmonic oscillator trap.

APPENDICES

Appendix A

Equations for Source Imaging

Chapter

Momentum of a projectile nucleon in the reaction center of mass, $p_{1,\text{cm}}$, given the kinetic energy in the laboratory frame T_{lab}, mass of a nucleon m_0, and mass number of projectile and target A_1 and A_2 is given by

$$p_{1,\text{cm}}^2 = -\frac{1}{2}\frac{A_1^2 + A_2^2}{A_1^2}m_0^2$$
$$-\sqrt{\left(p_{1,\text{cm}}^2 + m_0^2\right)\left(p_{1,\text{cm}}^2 + \left(\frac{A_2}{A_1}m_0\right)^2\right)} \tag{A.1}$$
$$+\frac{1}{2}\left(\left(\frac{A_1 + A_2}{A_1}m_0\right)^2 + \frac{A_2}{A_1}T_{\text{lab}}\,m_0\right).$$

This equation is solved iteratively. The momentum of a target nucleon is correspondingly

$$p_{2,\text{cm}} = \frac{A_1}{A_2}p_{1,\text{cm}}. \tag{A.2}$$

Appendix B

Parameterizations of the source function

B.1 Half-width at half-maximum

The most leading-order approximation for describing the source function is $r_{1/2}$, the half-width at half-maximum. As the source function is generally seen to be Gaussian at short ranges, this value could be used to find the width of the Gaussian (if there are no other components super-imposed at short range). The other benefit is that it is agnostic to the actually details of the source function, and provides a coarse, understandable description.

The primary question is then how to determine the maximum of the source function. Fitting the source with a single Gaussian function is problematic, as the source falls off exponentially at large distances (see Fig. 3.4 inset). The HiRA group has fit the value of the source between 0.5 and 2.5 fm to a parabola symmetric around $r = 0$,

$$S(r) = a + br^2, \tag{B.1}$$

using a as the maximum [7]. They did not use the value of $S(r)$ near zero, as that value had a large uncertainty.

B.2 Hump fit

To fit the entire source function, one can also assume that it the combination of two Gaussian sources, one short- and one long-range. An example of this is the so-called hump fit, used in RHIC physics [55] (here abbreviated for one dimension):

$$S(r) = \exp\left[-F_s\left(\frac{r}{2r_s}\right)^2\right] \times \exp\left[-F_l\left(\frac{r}{2r_l}\right)^2\right], \tag{B.2}$$

where $F_s = 1/(1+(r/r_0)^2)$ and $F_l = 1 - F_s$. At short range, the first exponential dominates as a Gaussian and the second goes as e^{-r^4}. At a longer range, the first exponential reduces to a constant while the second acts as a Gaussian.

B.3 Chung fit

However, looking at Fig. 3.3, the long-range behavior of $S(r)$ is exponential. Naively, one would use a function that is the superposition of a Guassian and an exponential. However, since this is a one-dimensional function projected from three dimensions, the function should be smooth across $r = 0$, and an exponential of the form e^{-r} has a nonzero first derivative at the origin. Thus, one could use a functional form like [56],

$$S(r) = \frac{\lambda_{\text{gau}}}{\left(\sqrt{2\pi}R_{\text{gau}}\right)^3}\exp\left[-\frac{r^2}{2R_{\text{gau}}^2}\right] + \frac{\lambda_{\text{exp}}}{N(R_{\text{gau}}, R_{\text{exp}})}\exp\left[\frac{-\sqrt{r^2 + \beta^2}}{R_{\text{exp}}}\right],$$
$$N(R_{\text{gau}}, R_{\text{exp}}) = 4\pi\beta^3\left(\frac{K_0(z)}{z} + \frac{2K_1(z)}{z^2}\right), \ \beta = \frac{R_{\text{gau}}^2}{R_{\text{exp}}}, \ z = \frac{\beta}{R_{exp}} \tag{B.3}$$

f_{gau} is the fraction of proton pairs that contribute to the Gaussian part of the source within this source function parametrization, found by expanding the second term of Eq. B.3

in small r and integrating over all space.

$$
\begin{aligned}
f_{\text{gau}} &= \frac{4\pi}{\lambda_{\text{gau}} + \lambda_{\text{exp}}} \int_0^\infty \mathrm{d}r \, r^2 S_{\text{short-range}}(r) \\
&= \frac{4\pi}{\lambda_{\text{gau}} + \lambda_{\text{exp}}} \int_0^\infty \mathrm{d}r \, \frac{\lambda_{\text{gau}}}{\left(\sqrt{2\pi}R_{\text{gau}}\right)^3} \exp\left[-\frac{r^2}{2R_{\text{gau}}^2}\right] + \frac{\lambda_{\text{exp}}}{N(R_{\text{gau}}, R_{\text{exp}})} \exp\left[-\frac{\beta + r^2/2\beta}{R_{\text{exp}}}\right] \\
&= \frac{4\pi}{\lambda_{\text{gau}} + \lambda_{\text{exp}}} \left\{ \frac{\lambda_{\text{gau}}}{\left(\sqrt{2\pi}R_{\text{gau}}\right)^3} + \frac{\lambda_{\text{exp}}}{N(R_{\text{gau}}, R_{\text{exp}})} \exp\left[-\frac{R_{\text{gau}}^2}{R_{\text{exp}}^2}\right] \right\} \int_0^\infty \mathrm{d}r \, r^2 \exp\left[-\frac{r^2}{2R_{\text{gau}}^2}\right] \\
&= \frac{1}{\lambda_{\text{gau}} + \lambda_{\text{exp}}} \left\{ \lambda_{\text{gau}} + \lambda_{\text{exp}} \frac{\left(\sqrt{2\pi}R_{\text{gau}}\right)^3}{N(R_{\text{gau}}, R_{\text{exp}})} \exp\left[-\frac{R_{\text{gau}}^2}{R_{\text{exp}}^2}\right] \right\}
\end{aligned}
$$

$$(\text{B.4})$$

Appendix C

Existence of the BEC in one dimension

The occupation probability, $f(\epsilon)$, for a system of bosons in thermal equilibrium is

$$f(\epsilon) = \frac{e^{-\beta(\epsilon-\mu)}}{1 - e^{-\beta(\epsilon-\mu)}}, \tag{C.1}$$

where β is the inverse temperature, ϵ is the energy of the state in question, and μ is the chemical potential. Thus the occupation probability approaches infinity as μ approaches ϵ from below — that is, as it costs less and less energy to increase the occupation of this state. This divergence leads to the phenomenon of BECs [91].

Therefore, if there exists a critical density that makes the chemical potential go to zero, then we have a condensate. This density ρ, in a volume of dimension D (in the non-relativistic case), is

$$
\begin{aligned}
\rho(\mu \to 0^-, T) &= (2s+1) \int \frac{\mathrm{d}^D p}{(2\pi\hbar)^D} \frac{e^{-p^2/(2mT)}}{1 - e^{-p^2/(2mT)}} \\
&= (2s+1) \int \frac{\mathrm{d}^D p}{(2\pi\hbar)^D} \sum_{n=1}^{\infty} e^{-np^2/(2mT)} \\
&= (2s+1) \left(\frac{\sqrt{mT}}{2\pi\hbar}\right)^D \left(\int \mathrm{d}^D x \, e^{-x^2/2}\right) \sum_{n=1}^{\infty} n^{-D/2}
\end{aligned}
\tag{C.2}
$$

For $D = 1$ and $D = 2$, the sum over n diverges — hence, strictly speaking, an ideal BEC cannot form in 1 or 2 dimensions.

Appendix D

Numerical stability in the density matrix time evolution

Since we are describing continuous space with a finite set of discrete points, we must choose suitable parameters for the resolution and range of position and momentum such that the numerical approximations do not affect the physics predictions. We also use a finite timestep, which leads to its own constraints.

We approximate continuous time with a series of discrete timesteps, and assume that the Hamiltonian is constant over that timestep. Thus the time evolution operator for the wave function is approximated,

$$
\begin{aligned}
\hat{U}(t + \Delta t, t) &= \exp\left\{ -\frac{i}{\hbar} \int_t^{t+\Delta t} \mathrm{d}\tau \, \hat{\mathcal{H}}(\tau) \right\} \\
&\approx \exp\left\{ -\frac{i}{\hbar} \hat{\mathcal{H}}(t) \Delta t \right\}
\end{aligned}
\tag{D.1}
$$

Since there is a density-dependent mean field potential, and the density changes with time, the Hamiltonian changes with time. So, to maintain the validity of the approximation in Eq. D.1, the density should change slowly with time, and thus, the time evolution operator that the density matrix is multiplied by should be not too far away from unity. In addition, the Split Operator Method (SOM) that we are using for the time evolution (described in Section 4.3) is accurate to $\mathcal{O}\left((\Delta t)^3\right)$, so Δt must itself be kept small, as we shouldn't

evolve too much with the part of the Hamiltonian that is diagonal in the position basis before evolving with the momentum-diagonal part. Since we are employing the SOM, we can address the momentum- and position-dependent terms of the time evolution operator separately to determine the constraints on the resolution, range, and timestep parameters.

The factor that must be kept close to unity is the one multiplied by the density matrix. The time dependence of the density matrix can be related to the its definition in terms of wave functions (Eq. 4.11). Combining this with the wave function evolution in Eq. D.1, we arrive at

$$\hat{\rho}(t + \Delta t) = \hat{U}\, \hat{\rho}(t)\, \hat{U}^\dagger$$
$$= \hat{U} \left\{ \sum_\alpha n_\alpha \, |\phi_\alpha\rangle \, \langle\phi_\alpha| \right\} \hat{U}^\dagger \,. \tag{D.2}$$

In momentum space, using just the kinetic term of the Hamiltonian, this becomes

$$\rho^{(k)}(k, k', t + \Delta t) = \exp\left[-i\hbar \frac{k^2}{2m} \Delta t\right] \left\{ \sum_\alpha n_\alpha \, \phi_\alpha(k, t) \, \phi_\alpha^*(k', t) \right\} \exp\left[i\hbar \frac{k'^2}{2m} \Delta t\right] \,. \tag{D.3}$$

Thus, the most significant phase factor that a grid point in momentum space will be multiplied by is $\exp[i\hbar \frac{k_{\max}^2}{2m} \Delta t]$. This maximum value for k is given by Eq. 4.15 (or Eq. 4.16 for the rotated system), which is in terms of Δx. The argument of the exponential should be small compared to $\pi/2$, since that would make the phase factor equal to i. This yields the constraint

$$\frac{\hbar \pi^2}{2m} \frac{\Delta t}{(\Delta x)^2} \ll \frac{\pi}{2} \,. \tag{D.4}$$

A similar result is attained for the position-basis evolution. In general, the constraint is

$$\left(\frac{V_{\mathrm{max}} - V_{\mathrm{min}}}{\hbar}\right)\Delta t \ll \frac{\pi}{2} . \tag{D.5}$$

For the case when the largest part of the potential is an external harmonic oscillator, which is the case in the trapped BEC system we study in Section 4.6, and when it is much larger than the minimum potential at any position, the constraint becomes

$$\frac{m\Omega^2}{2\hbar}x_{\mathrm{max}}^2\Delta t \ll \frac{\pi}{2} . \tag{D.6}$$

BIBLIOGRAPHY

BIBLIOGRAPHY

[1] Norbert Herrmann, Johannes P. Wessels, and Thomas Wienold, "Collective flow in heavy-ion collisions," Annual Review of Nuclear and Particle Science **49**, 581–632 (1999), `http://www.annualreviews.org/doi/abs/10.1146/annurev.nucl.49.1.581`

[2] E. Colin, Rulin Sun, N. N. Ajitanand, John M. Alexander, M. A. Barton, P. A. DeYoung, A. Elmaani, C. J. Gelderloos, E. E. Gualtieri, D. Guinet, S. Hannuschke, J. A. Jasma, L. Kowalski, Roy A. Lacey, J. Lauret, E. Norbeck, R. Pak, G. F. Peaslee, M. Stern, N. T. B. Stone, S. D. Sundbeck, A. M. Vander Molen, G. D. Westfall, and J. Yee, "Splintering central collisions: Systematics of momentum and energy deposition for (17–115) A MeV ^{40}Ar," Physical Review C **57**, R1032–R1036 (Mar. 1998), `http://link.aps.org/doi/10.1103/PhysRevC.57.R1032`

[3] W. Reisdorf, A. Andronic, R. Averbeck, M.L. Benabderrahmane, O.N. Hartmann, N. Herrmann, K.D. Hildenbrand, T.I. Kang, Y.J. Kim, M. Kiš, P. Koczoń, T. Kress, Y. Leifels, M. Merschmeyer, K. Piasecki, A. Schüttauf, M. Stockmeier, V. Barret, Z. Basrak, N. Bastid, R. Čaplar, P. Crochet, P. Dupieux, M. Dželalija, Z. Fodor, P. Gasik, Y. Grishkin, B. Hong, J. Kecskemeti, M. Kirejczyk, M. Korolija, R. Kotte, A. Lebedev, X. Lopez, T. Matulewicz, W. Neubert, M. Petrovici, F. Rami, M.S. Ryu, Z. Seres, B. Sikora, K.S. Sim, V. Simion, K. Siwek-Wilczyńska, V. Smolyankin, G. Stoicea, Z. Tymiński, K. Wiśniewski, D. Wohlfarth, Z.G. Xiao, H.S. Xu, I. Yushmanov, and A. Zhilin, "Systematics of central heavy ion collisions in the 1 A GeV regime," Nuclear Physics A **848**, 366–427 (Dec. 2010), ISSN 0375-9474, `http://www.sciencedirect.com/science/article/pii/S0375947410006810`

[4] F. Rami, Y. Leifels, B. de Schauenburg, A. Gobbi, B. Hong, J. P. Alard, A. Andronic, R. Averbeck, V. Barret, Z. Basrak, N. Bastid, I. Belyaev, A. Bendarag, G. Berek, R. Čaplar, N. Cindro, P. Crochet, A. Devismes, P. Dupieux, M. Dželalija, M. Eskef, C. Finck, Z. Fodor, H. Folger, L. Fraysse, A. Genoux-Lubain, Y. Grigorian, Y. Grishkin, N. Herrmann, K. D. Hildenbrand, J. Kecskemeti, Y. J. Kim, P. Koczon, M. Kirejczyk, M. Korolija, R. Kotte, M. Kowalczyk, T. Kress, R. Kutsche, A. Lebedev, K. S. Lee, V. Manko, H. Merlitz, S. Mohren, D. Moisa, J. Mösner, W. Neubert, A. Nianine, D. Pelte, M. Petrovici, C. Pinkenburg, C. Plettner, W. Reisdorf, J. Ritman, D. Schüll, Z. Seres, B. Sikora, K. S. Sim, V. Simion, K. Siwek-Wilczyńska, A. Somov, M. R. Stockmeier, G. Stoicea, M. Vasiliev, P. Wagner, K. Wiśniewski, D. Wohlfarth, J. T. Yang, I. Yushmanov, A. Zhilin, and (FOPI Collaboration), "Isospin tracing: A probe of nonequilibrium in central heavy-ion collisions," Physical Review Letters **84**, 1120–1123 (Feb. 2000), `http://link.aps.org/doi/10.1103/PhysRevLett.84.1120`

[5] Roy A. Lacey, N. N. Ajitanand, J. M. Alexander, P. Chung, W. G. Holzmann, M. Issah, A. Taranenko, P. Danielewicz, and Horst Stöcker, "Has the QCD critical point been signaled by observations at the BNL relativistic heavy ion collider?." Physical Review Letters **98**, 092301 (Mar. 2007), `http://link.aps.org/doi/10.1103/PhysRevLett.98.092301`

[6] David Brown, "An introduction to source imaging in heavy-ion reactions," Website (May 2002), `https://adg.llnl.gov/Research/source_imaging/intro.html`

[7] Micha A. Kilburn, *Proton-Proton Correlation Functions as a Probe to Reaction Dynamics*, Ph.D., Michigan State University, East Lansing, MI, USA (2011), `http://www.nscl.msu.edu/ourlab/publications/download/Kilburn2011_281.pdf`

[8] P. Danielewicz and G.F. Bertsch, "Production of deuterons and pions in a transport model of energetic heavy-ion reactions," Nuclear Physics A **533**, 712–748 (Nov. 1991), ISSN 0375-9474, `http://www.sciencedirect.com/science/article/pii/037594749190541D`

[9] P. Danielewicz, "Formation of composites emitted at large angles in intermediate and high energy reactions," Nuclear Physics A **545**, 21–34 (Aug. 1992), ISSN 0375-9474, `http://www.sciencedirect.com/science/article/pii/037594749290443N`

[10] Paweł Danielewicz and Qiubao Pan, "Blast of light fragments from central heavy-ion collisions," Physical Review C **46**, 2002 (Nov. 1992), `http://link.aps.org/doi/10.1103/PhysRevC.46.2002`

[11] Qiubao Pan and Paweł Danielewicz, "From sideward flow to nuclear compressibility," Physical Review Letters **70**, 2062–2065 (Apr. 1993), `http://link.aps.org/doi/10.1103/PhysRevLett.70.2062`

[12] P. Danielewicz, "Effects of compression and collective expansion on particle emission from central heavy-ion reactions," Physical Review C **51**, 716–750 (Feb. 1995), `http://link.aps.org/doi/10.1103/PhysRevC.51.716`

[13] P. Danielewicz, Roy A. Lacey, P.-B. Gossiaux, C. Pinkenburg, P. Chung, J. M. Alexander, and R. L. McGrath, "Disappearance of elliptic flow: A new probe for the nuclear equation of state," Physical Review Letters **81**, 2438–2441 (Sep. 1998), `http://link.aps.org/doi/10.1103/PhysRevLett.81.2438`

[14] P. K. Kovtun, D. T. Son, and A. O. Starinets, "Viscosity in strongly interacting quantum field theories from black hole physics," Physical Review Letters **94**, 111601 (Mar. 2005), `http://link.aps.org/doi/10.1103/PhysRevLett.94.111601`

[15] N. Auerbach and S. Shlomo, "η/s ratio in finite nuclei," Physical Review Letters **103**, 172501 (Oct. 2009), http://link.aps.org/doi/10.1103/PhysRevLett.103.172501

[16] Subrata Pal, "Shear viscosity to entropy density ratio in nuclear multifragmentation," Physical Review C **81**, 051601 (May 2010), http://link.aps.org/doi/10.1103/PhysRevC.81.051601

[17] Chenglong Zhou, Yugang Ma, and Deqing Fang, "Shear viscosity to entropy density ratio in Au+Au central collisions," Plasma Science and Technology **14**, 585–587 (Jul. 2012), ISSN 1009-0630, http://iopscience.iop.org/1009-0630/14/7/04

[18] Cai Yanhuang and M. Di Toro, "Semiclassical description of isovector giant multipole resonances," Physical Review C **39**, 105–113 (Jan. 1989), http://link.aps.org/doi/10.1103/PhysRevC.39.105

[19] T. Gaitanos, M. Colonna, M. Di Toro, and H.H. Wolter, "Stopping and isospin equilibration in heavy ion collisions," Physics Letters B **595**, 209–215 (Aug. 2004), ISSN 0370-2693, http://www.sciencedirect.com/science/article/pii/S0370269304008792

[20] V. R. Pandharipande and Steven C. Pieper, "Nuclear transparency to intermediate-energy nucleons from (e,e'p) reactions," Physical Review C **45**, 791–798 (Feb. 1992), http://link.aps.org/doi/10.1103/PhysRevC.45.791

[21] Declan Persram and Charles Gale, "Elliptic flow in intermediate energy heavy ion collisions and in-medium effects," Physical Review C **65**, 064611 (May 2002), http://link.aps.org/doi/10.1103/PhysRevC.65.064611

[22] Bao-An Li and Lie-Wen Chen, "Nucleon-nucleon cross sections in neutron-rich matter and isospin transport in heavy-ion reactions at intermediate energies," Physical Review C **72**, 064611 (Dec. 2005), http://link.aps.org/doi/10.1103/PhysRevC.72.064611

[23] P. Danielewicz, "Hadronic transport models," Acta Physica Polonica B **33**, 45 (2002), acta Phys.Polon. B33 (2002) 45-64, http://arxiv.org/abs/nucl-th/0201032

[24] T. Alm, G. Röpke, and M. Schmidt, "Critical enhancement of the in-medium nucleon-nucleon cross section at low temperatures," Physical Review C **50**, 31–37 (Jul. 1994), http://link.aps.org/doi/10.1103/PhysRevC.50.31

[25] T. Alm, G. Röpke, W. Bauer, F. Daffin, and M. Schmidt, "The in-medium nucleon-nucleon cross section and BUU simulations of heavy-ion reactions," Nuclear Physics A **587**, 815–827 (May 1995), ISSN 0375-9474, http://www.sciencedirect.com/science/article/pii/037594749500026W

116

[26] C. Fuchs, Amand Faessler, and M. El-Shabshiry, "Off-shell behavior of the in-medium nucleon-nucleon cross section," Physical Review C **64**, 024003 (Jul. 2001), `http://link.aps.org/doi/10.1103/PhysRevC.64.024003`

[27] W. J. Nicholson and I. Halpern, "Direct-interaction effects in medium-energy fission of uranium," Physical Review **116**, 175–177 (Oct. 1959), `http://link.aps.org/doi/10.1103/PhysRev.116.175`

[28] Torbjørn Sikkeland, Eldon L. Haines, and Victor E. Viola, "Momentum transfer in heavy-ion-induced fission," Physical Review **125**, 1350–1357 (Feb. 1962), `http://link.aps.org/doi/10.1103/PhysRev.125.1350`

[29] V. E. Viola, B. B. Back, K. L. Wolf, T. C. Awes, C. K. Gelbke, and H. Breuer, "Linear momentum transfer in nonrelativistic nucleus-nucleus collisions," Physical Review C **26**, 178–188 (Jul. 1982), `http://link.aps.org/doi/10.1103/PhysRevC.26.178`

[30] E. Colin, Rulin Sun, N. N. Ajitanand, John M. Alexander, M. A. Barton, P. A. DeYoung, A. Elmaani, C. J. Gelderloos, E. E. Gualtieri, D. Guinet, S. Hannuschke, J. A. Jasma, L. Kowalski, Roy A. Lacey, J. Lauret, E. Norbeck, R. Pak, G. F. Peaslee, M. Stern, N. T. B. Stone, S. D. Sundbeck, A. M. Vander Molen, G. D. Westfall, and J. Yee, "Splintering central collisions: Systematics of momentum and energy deposition for (17–115)A MeV 40 ar," Physical Review C **57**, R1032–R1036 (Mar. 1998), `http://link.aps.org/doi/10.1103/PhysRevC.57.R1032`

[31] W. Reisdorf, M. Stockmeier, A. Andronic, M.L. Benabderrahmane, O.N. Hartmann, N. Herrmann, K.D. Hildenbrand, Y.J. Kim, M. Kiš, P. Koczoń, T. Kress, Y. Leifels, X. Lopez, M. Merschmeyer, A. Schüttauf, V. Barret, Z. Basrak, N. Bastid, R. Čaplar, P. Crochet, P. Dupieux, M. Dželalija, Z. Fodor, Y. Grishkin, B. Hong, T.I. Kang, J. Kecskemeti, M. Kirejczyk, M. Korolija, R. Kotte, A. Lebedev, T. Matulewicz, W. Neubert, M. Petrovici, F. Rami, M.S. Ryu, Z. Seres, B. Sikora, K.S. Sim, V. Simion, K. Siwek-Wilczyńska, V. Smolyankin, G. Stoicea, Z. Tymiński, K. Wiśniewski, D. Wohlfarth, Z.G. Xiao, H.S. Xu, I. Yushmanov, and A. Zhilin, "Systematics of pion emission in heavy ion collisions in the regime," Nuclear Physics A **781**, 459–508 (Jan. 2007), ISSN 0375-9474, `http://www.sciencedirect.com/science/article/pii/S0375947406007676`

[32] Particle Data Group, J. Beringer, J. F. Arguin, R. M. Barnett, K. Copic, O. Dahl, D. E. Groom, C. J. Lin, J. Lys, H. Murayama, C. G. Wohl, W. M. Yao, P. A. Zyla, C. Amsler, M. Antonelli, D. M. Asner, H. Baer, H. R. Band, T. Basaglia, C. W. Bauer, J. J. Beatty, V. I. Belousov, E. Bergren, G. Bernardi, W. Bertl, S. Bethke, H. Bichsel, O. Biebel, E. Blucher, S. Blusk, G. Brooijmans, O. Buchmueller, R. N. Cahn, M. Carena, A. Ceccucci, D. Chakraborty, M. C. Chen, R. S. Chivukula, G. Cowan, G. D'Ambrosio, T. Damour, D. de Florian, A. de Gouvêa, T. DeGrand, P. de Jong,

G. Dissertori, B. Dobrescu, M. Doser, M. Drees, D. A. Edwards, S. Eidelman, J. Erler, V. V. Ezhela, W. Fetscher, B. D. Fields, B. Foster, T. K. Gaisser, L. Garren, H. J. Gerber, G. Gerbier, T. Gherghetta, S. Golwala, M. Goodman, C. Grab, A. V. Gritsan, J. F. Grivaz, M. Grünewald, A. Gurtu, T. Gutsche, H. E. Haber, K. Hagiwara, C. Hagmann, C. Hanhart, S. Hashimoto, K. G. Hayes, M. Heffner, B. Heltsley, J. J. Hernández-Rey, K. Hikasa, A. Höcker, J. Holder, A. Holtkamp, J. Huston, J. D. Jackson, K. F. Johnson, T. Junk, D. Karlen, D. Kirkby, S. R. Klein, E. Klempt, R. V. Kowalewski, F. Krauss, M. Kreps, B. Krusche, Yu. V. Kuyanov, Y. Kwon, O. Lahav, J. Laiho, P. Langacker, A. Liddle, Z. Ligeti, T. M. Liss, L. Littenberg, K. S. Lugovsky, S. B. Lugovsky, T. Mannel, A. V. Manohar, W. J. Marciano, A. D. Martin, A. Masoni, J. Matthews, D. Milstead, R. Miquel, K. Mönig, F. Moortgat, K. Nakamura, M. Narain, P. Nason, S. Navas, M. Neubert, P. Nevski, Y. Nir, K. A. Olive, L. Pape, J. Parsons, C. Patrignani, J. A. Peacock, S. T. Petcov, A. Piepke, A. Pomarol, G. Punzi, A. Quadt, S. Raby, G. Raffelt, B. N. Ratcliff, P. Richardson, S. Roesler, S. Rolli, A. Romaniouk, L. J. Rosenberg, J. L. Rosner, C. T. Sachrajda, Y. Sakai, G. P. Salam, S. Sarkar, F. Sauli, O. Schneider, K. Scholberg, D. Scott, W. G. Seligman, M. H. Shaevitz, S. R. Sharpe, M. Silari, T. Sjöstrand, P. Skands, J. G. Smith, G. F. Smoot, S. Spanier, H. Spieler, A. Stahl, T. Stanev, S. L. Stone, T. Sumiyoshi, M. J. Syphers, F. Takahashi, M. Tanabashi, J. Terning, M. Titov, N. P. Tkachenko, N. A. Törnqvist, D. Tovey, G. Valencia, K. van Bibber, G. Venanzoni, M. G. Vincter, P. Vogel, A. Vogt, W. Walkowiak, C. W. Walter, D. R. Ward, T. Watari, G. Weiglein, E. J. Weinberg, L. R. Wiencke, L. Wolfenstein, J. Womersley, C. L. Woody, R. L. Workman, A. Yamamoto, G. P. Zeller, O. V. Zenin, J. Zhang, R. Y. Zhu, G. Harper, V. S. Lugovsky, and P. Schaffner, "Review of particle physics," Physical Review D **86**, 010001 (Jul. 2012), http://link.aps.org/doi/10.1103/PhysRevD.86.010001

[33] A. Andronic, J. Łukasik, W. Reisdorf, and W. Trautmann, "Systematics of stopping and flow in Au+Au collisions," in *Dynamics and Thermodynamics with Nuclear Degrees of Freedom*, edited by Philippe Chomaz, Francesca Gulminelli, Wolfgang Trautmann, and Sherry J. Yennello (Springer Berlin Heidelberg, 2006) pp. 31–46, ISBN 978-3-540-46496-9, http://www.springerlink.com/content/r254w7472431kn85/abstract/

[34] Paweł Danielewicz, Roy Lacey, and William G. Lynch, "Determination of the equation of state of dense matter," Science **298**, 1592–1596 (Nov. 2002), ISSN 0036-8075, 1095-9203, http://www.sciencemag.org/content/298/5598/1592

[35] J.P. Blaizot, J.F. Berger, J. Dechargé, and M. Girod, "Microscopic and macroscopic determinations of nuclear compressibility," Nuclear Physics A **591**, 435–457 (Aug. 1995), ISSN 0375-9474, http://www.sciencedirect.com/science/article/pii/037594749500294B

[36] W. Reisdorf, A. Andronic, R. Averbeck, M.L. Benabderrahmane, O.N. Hartmann, N. Herrmann, K.D. Hildenbrand, T.I. Kang, Y.J. Kim, M. Kiš, P. Koczoń, T. Kress,

Y. Leifels, M. Merschmeyer, K. Piasecki, A. Schüttauf, M. Stockmeier, V. Barret, Z. Basrak, N. Bastid, R. Čaplar, P. Crochet, P. Dupieux, M. Dželalija, Z. Fodor, P. Gasik, Y. Grishkin, B. Hong, J. Kecskemeti, M. Kirejczyk, M. Korolija, R. Kotte, A. Lebedev, X. Lopez, T. Matulewicz, W. Neubert, M. Petrovici, F. Rami, M.S. Ryu, Z. Seres, B. Sikora, K.S. Sim, V. Simion, K. Siwek-Wilczyńska, V. Smolyankin, G. Stoicea, Z. Tymiński, K. Wiśniewski, D. Wohlfarth, Z.G. Xiao, H.S. Xu, I. Yushmanov, and A. Zhilin, "Systematics of central heavy ion collisions in the 1 a GeV regime," Nuclear Physics A **848**, 366–427 (Dec. 2010), ISSN 0375-9474, `http://www.sciencedirect.com/science/article/pii/S0375947410006810`

[37] C. Hartnack, Rajeev K. Puri, J. Aichelin, J. Konopka, S. A. Bass, H. Stöcker, and W. Greiner, "Modelling the many-body dynamics of heavy ion collisions: Present status and future perspective," The European Physical Journal A - Hadrons and Nuclei **1**, 151–169 (Feb. 1998), ISSN 1434-6001, 1434-601X, `http://link.springer.com/article/10.1007/s100500050045`

[38] Pawel Danielewicz, Brent Barker, and Lijun Shi, "From stopping to viscosity in nuclear reactions," AIP Conference Proceedings **1128**, 104–111 (May 2009), ISSN 0094243X, `http://proceedings.aip.org/resource/2/apcpcs/1128/1/104_1`

[39] Roy A. Lacey, "Is there a sonic boom in the little bang at RHIC?." Nuclear Physics A **785**, 122–127 (Mar. 2007), ISSN 0375-9474, `http://www.sciencedirect.com/science/article/pii/S0375947406009109`

[40] F. Karsch, E. Laermann, and A. Peikert, "Quark mass and flavour dependence of the QCD phase transition," Nuclear Physics B **605**, 579–599 (Jul. 2001), ISSN 0550-3213, `http://www.sciencedirect.com/science/article/pii/S0550321301002000`

[41] R. Hanbury Brown and R.Q. Twiss, "A new type of interferometer for use in radio astronomy," Philosophical Magazine Series 7 **45**, 663–682 (1954), ISSN 1941-5982, `http://www.tandfonline.com/doi/abs/10.1080/14786440708520475`

[42] Gerson Goldhaber, Sulamith Goldhaber, Wonyong Lee, and Abraham Pais, "Influence of bose-einstein statistics on the antiproton-proton annihilation process," Physical Review **120**, 300–312 (Oct. 1960), `http://link.aps.org/doi/10.1103/PhysRev.120.300`

[43] Michael Annan Lisa, Scott Pratt, Ron Soltz, and Urs Wiedemann, "FEMTOSCOPY IN RELATIVISTIC HEAVY ION COLLISIONS: two decades of progress," Annual Review of Nuclear and Particle Science **55**, 357–402 (2005), `http://www.annualreviews.org/doi/abs/10.1146/annurev.nucl.55.090704.151533`

[44] A. Perrin, R. Bücker, S. Manz, T. Betz, C. Koller, T. Plisson, T. Schumm, and J. Schmiedmayer, "Hanbury brown and twiss correlations across the bose-einstein condensation threshold," Nature Physics **8**, 195–198 (2012), ISSN 1745-2473, `http://www.nature.com.proxy1.cl.msu.edu/nphys/journal/v8/n3/full/nphys2212.html`

[45] D. O. Handzy, M. A. Lisa, C. K. Gelbke, W. Bauer, F. C. Daffin, P. Decowski, W. G. Gong, E. Gualtieri, S. Hannuschke, R. Lacey, T. Li, W. G. Lynch, C. M. Mader, G. F. Peaslee, T. Reposeur, S. Pratt, A. M. Vander Molen, G. D. Westfall, J. Yee, and S. J. Yennello, "Two-proton correlation functions for ^{36}ar+^{45}sc at E/A=80 MeV," Physical Review C **50**, 858–870 (Aug. 1994), `http://link.aps.org/doi/10.1103/PhysRevC.50.858`

[46] D. Ardouin, "Recent light particle correlation data from heavy ion collisions at intermediate and low energies," International Journal of Modern Physics E **06**, 391–435 (Sep. 1997), ISSN 0218-3013, 1793-6608, `http://www.worldscientific.com/doi/abs/10.1142/S021830139700024X`

[47] E. De Filippo, F. Amorini, L. Auditore, V. Baran, I. Berceanu, G. Cardella, M. Colonna, E. Geraci, S. Gianì, L. Grassi, A. Grzeszczuk, P. Guazzoni, J. Han, E. La Guidara, G. Lanzalone, I. Lombardo, C. Maiolino, T. Minniti, A. Pagano, M. Papa, E. Piasecki, S. Pirrone, G. Politi, A. Pop, F. Porto, F. Rizzo, P. Russotto, S. Santoro, A. Trifirò, M. Trimarchi, G. Verde, M. Vigilante, J. Wilczyński, and L. Zetta, "Correlations between isospin dynamics and intermediate mass fragments emission time scales: a probe for the symmetry energy in asymmetric nuclear matter," arXiv:1209.6461(Sep. 2012), `http://arxiv.org/abs/1209.6461`

[48] M. A. Lisa, C. K. Gelbke, P. Decowski, W. G. Gong, E. Gualtieri, S. Hannuschke, R. Lacey, T. Li, W. G. Lynch, G. F. Peaslee, S. Pratt, T. Reposeur, A. M. Vander Molen, G. D. Westfall, J. Yee, and S. J. Yennello, "Observation of lifetime effects in two-proton correlations for well-characterized sources," Physical Review Letters **71**, 2863–2866 (Nov. 1993), `http://link.aps.org/doi/10.1103/PhysRevLett.71.2863`

[49] R. Ghetti and J. Helgesson, "Isospin effects in two-particle correlation functions: A probe for the isospin dependence of the nuclear equation of state," Nuclear Physics A **752**, 480–483 (Apr. 2005), ISSN 0375-9474, `http://www.sciencedirect.com/science/article/pii/S0375947405002034`

[50] Steven E. Koonin, "Proton pictures of high-energy nuclear collisions," Physics Letters B **70**, 43–47 (Sep. 1977), ISSN 0370-2693, `http://www.sciencedirect.com/science/article/pii/0370269377903409`

[51] S. Pratt, T. Csörgő, and J. Zimányi, "Detailed predictions for two-pion correlations in ultrarelativistic heavy-ion collisions," Physical Review C **42**, 2646–2652 (Dec. 1990), `http://link.aps.org/doi/10.1103/PhysRevC.42.2646`

[52] D. A. Brown and P. Danielewicz, "Observing non-gaussian sources in heavy-ion reactions," Physical Review C **64**, 014902 (Jun. 2001), `http://link.aps.org/doi/10.1103/PhysRevC.64.014902`

[53] Michael Youngs, personal communication (Nov. 2012)

[54] V. Henzl, M. A. Kilburn, Z. Chajęcki, D. Henzlova, W. G. Lynch, D. Brown, A. Chbihi, D. D. S. Coupland, P. Danielewicz, R. T. deSouza, M. Famiano, C. Herlitzius, S. Hudan, Jenny Lee, S. Lukyanov, A. M. Rogers, A. Sanetullaev, L. G. Sobotka, Z. Y. Sun, M. B. Tsang, A. Vander Molen, G. Verde, M. S. Wallace, and M. Youngs, "Angular dependence in proton-proton correlation functions in central ˆ{40}ca + ˆ{40}ca and ˆ{48}ca + ˆ{48}ca reactions," Physical Review C **85**, 014606 (Jan. 2012), `http://link.aps.org/doi/10.1103/PhysRevC.85.014606`

[55] Paul Chung, "3D pion & kaon source imaging from run4 and run7 200 AGeV Au+Au collisions," (2010), `http://wpcf2010.bitp.kiev.ua/presentations/sept18/Kiev10_Chung_STAR_PionKaonSourceImaging.ppt`

[56] P. Chung, A. Taranenko, R. Lacey, W. Holzmann, J. Alexander, and M. Issah, "Extraction of source images in Au+Au and d+Au collisions at RHIC," Nuclear Physics A **749**, 275–278 (Mar. 2005), ISSN 0375-9474, `http://www.sciencedirect.com/science/article/pii/S0375947404012680`

[57] F. James and M. Roos, "Minuit - a system for function minimization and analysis of the parameter errors and correlations," Computer Physics Communications **10**, 343–367 (Dec. 1975), ISSN 0010-4655, `http://www.sciencedirect.com/science/article/pii/0010465575900399`

[58] P. Danielewicz, "Quantum theory of nonequilibrium processes, i," Annals of Physics (N.Y.) **152**, 239 (1984)

[59] G. Verde, P. Danielewicz, D. A. Brown, W. G. Lynch, C. K. Gelbke, and M. B. Tsang, "Probing transport theories via two-proton source imaging," Physical Review C **67**, 034606 (Mar. 2003), `http://link.aps.org/doi/10.1103/PhysRevC.67.034606`

[60] L. P. Kadanoff and G. Baym, *Quantum Statistical Mechanics* (Benjamin, New York, 1962)

[61] Wim Botermans and Rudi Malfliet, "Quantum transport theory of nuclear matter," Physics Reports **198**, 115–194 (Dec. 1990), ISSN 0370-1573, `http://www.sciencedirect.com/science/article/pii/037015739090174Z`

[62] H. S. Köhler, "Memory and correlation effects in nuclear collisions," Physical Review C **51**, 3232–3239 (Jun. 1995), `http://link.aps.org/doi/10.1103/PhysRevC.51.3232`

[63] N. H. Kwong, M. Bonitz, R. Binder, and H. S. Köhler, "Semiconductor kadanoff-baym equation results for optically excited Electron–Hole plasmas in quantum wells," physica status solidi (b) **206**, 197–203 (1998), ISSN 1521-3951, `http://onlinelibrary.wiley.com/doi/10.1002/(SICI)1521-3951(199803)206:1<197::AID-PSSB197>3.0.CO;2-9/abstract`

[64] Nils Erik Dahlen and Robert van Leeuwen, "Solving the kadanoff-baym equations for inhomogeneous systems: Application to atoms and molecules," Physical Review Letters **98**, 153004 (Apr. 2007), `http://link.aps.org/doi/10.1103/PhysRevLett.98.153004`

[65] K. Balzer, S. Bauch, and M. Bonitz, "Time-dependent second-order born calculations for model atoms and molecules in strong laser fields," Physical Review A **82**, 033427 (Sep. 2010), `http://link.aps.org/doi/10.1103/PhysRevA.82.033427`

[66] K. Balzer, M. Bonitz, R. van Leeuwen, A. Stan, and N. E. Dahlen, "Nonequilibrium green's function approach to strongly correlated few-electron quantum dots," Physical Review B **79**, 245306 (Jun. 2009), `http://link.aps.org/doi/10.1103/PhysRevB.79.245306`

[67] K. Balzer, S. Hermanns, and M. Bonitz, "Electronic double excitations in quantum wells: Solving the two-time kadanoff-baym equations," EPL (Europhysics Letters) **98**, 67002 (Jun. 2012), ISSN 0295-5075, `http://iopscience.iop.org.proxy1.cl.msu.edu/0295-5075/98/6/67002`

[68] N. Säkkinen, M. Manninen, and R. van Leeuwen, "The Kadanoff–Baym approach to double excitations in finite systems," New Journal of Physics **14**, 013032 (Jan. 2012), ISSN 1367-2630, `http://iopscience.iop.org.proxy1.cl.msu.edu/1367-2630/14/1/013032`

[69] T. Gasenzer, "Ultracold gases far from equilibrium," The European Physical Journal Special Topics **168**, 89–148 (Mar. 2009), ISSN 1951-6355, 1951-6401, `http://epjst.epj.org/index.php?option=com_article&access=doi&doi=10.1140/epjst/e2009-00960-5`

[70] Arnau Rios, Brent Barker, Mark Buchler, and Pawel Danielewicz, "Towards a nonequilibrium green's function description of nuclear reactions: One-dimensional mean-field dynamics," Annals of Physics **326**, 1274–1319 (May 2011), ISSN 0003-4916, arXiv:1009.0215, `http://www.sciencedirect.com/science/article/pii/S000349161000223X`

[71] P Danielewicz, "Quantum theory of nonequilibrium processes II. application to nuclear collisions," Annals of Physics **152**, 305–326 (Feb. 1984), ISSN 0003-4916, `http://www.sciencedirect.com/science/article/pii/0003491684900939`

[72] M. Tohyama, "Application of quantum theory of particle collisions to ^{16}o + ^{16}o reactions," Physical Review C **36**, 187–192 (Jul. 1987), `http://link.aps.org/doi/10.1103/PhysRevC.36.187`

[73] J. W. Negele, "The mean-field theory of nuclear structure and dynamics," Reviews of Modern Physics **54**, 913–1015 (Oct. 1982), `http://link.aps.org/doi/10.1103/RevModPhys.54.913`

[74] Cédric Golabek and Cédric Simenel, "Collision dynamics of two ^{238}u atomic nuclei," Physical Review Letters **103**, 042701 (Jul. 2009), `http://link.aps.org/doi/10.1103/PhysRevLett.103.042701`

[75] S.K. Bogner, R.J. Furnstahl, and A. Schwenk, "From low-momentum interactions to nuclear structure," Progress in Particle and Nuclear Physics **65**, 94–147 (Jul. 2010), ISSN 0146-6410, `http://www.sciencedirect.com/science/article/pii/S0146641010000347`

[76] G. Hagen, T. Papenbrock, D. J. Dean, and M. Hjorth-Jensen, "Medium-mass nuclei from chiral nucleon-nucleon interactions," Physical Review Letters **101**, 092502 (Aug. 2008), `http://link.aps.org/doi/10.1103/PhysRevLett.101.092502`

[77] W.H. Dickhoff and C. Barbieri, "Self-consistent green's function method for nuclei and nuclear matter," Progress in Particle and Nuclear Physics **52**, 377–496 (Apr. 2004), ISSN 0146-6410, `http://www.sciencedirect.com/science/article/pii/S0146641004000535`

[78] H.S. Köhler, "TDHF with two-body dissipation," Nuclear Physics A **343**, 315–332 (Jul. 1980), ISSN 0375-9474, `http://www.sciencedirect.com/science/article/pii/0375947480906557`

[79] P. Grangé, J. Richert, G. Wolschin, and H.A. Weidenmüller, "Influence of a collision term on finite-size one-dimensional TDHF," Nuclear Physics A **356**, 260–268

(Mar. 1981), ISSN 0375-9474, `http://www.sciencedirect.com/science/article/pii/0375947481901263`

[80] M. Tohyama, "One-dimensional solution of an extended time-dependent hartree-fock theory," Physics Letters B **163**, 14–20 (Nov. 1985), ISSN 0370-2693, `http://www.sciencedirect.com/science/article/pii/0370269385901820`

[81] H.S. Köhler, N.H. Kwong, and Hashim A. Yousif, "A fortran code for solving the Kadanoff–Baym equations for a homogeneous fermion system," Computer Physics Communications **123**, 123–142 (Dec. 1999), ISSN 0010-4655, `http://www.sciencedirect.com/science/article/pii/S001046559900260X`

[82] M.D Feit, J.A Fleck Jr., and A Steiger, "Solution of the schrödinger equation by a spectral method," Journal of Computational Physics **47**, 412–433 (Sep. 1982), ISSN 0021-9991, `http://www.sciencedirect.com/science/article/pii/0021999182900912`

[83] M. Frigo and S.G. Johnson, "The design and implementation of FFTW3," Proceedings of the IEEE **93**, 216–231 (2005), ISSN 0018-9219

[84] Albert Messiah, *Quantum Mechanics* (Dover, New York, 1999) ISBN 0-486-40924-4

[85] D.J. Thouless and J.G. Valatin, "Time-dependent hartree-fock equations and rotational states of nuclei," Nuclear Physics **31**, 211–230 (Mar. 1962), ISSN 0029-5582, `http://www.sciencedirect.com/science/article/pii/0029558262907411`

[86] P. Bonche, S. Koonin, and J. W. Negele, "One-dimensional nuclear dynamics in the time-dependent hartree-fock approximation," Physical Review C **13**, 1226–1258 (Mar. 1976), `http://link.aps.org/doi/10.1103/PhysRevC.13.1226`

[87] H.S. Köhler and B.S. Nilsson, "Effect of two-body collisions on nuclear dynamics," Nuclear Physics A **417**, 541–563 (Apr. 1984), ISSN 0375-9474, `http://www.sciencedirect.com/science/article/pii/0375947484904123`

[88] Franco Dalfovo, Stefano Giorgini, Lev P. Pitaevskii, and Sandro Stringari, "Theory of bose-einstein condensation in trapped gases," Reviews of Modern Physics **71**, 463–512 (Apr. 1999), `http://link.aps.org/doi/10.1103/RevModPhys.71.463`

[89] A. Muñoz Mateo, V. Delgado, and Boris A. Malomed, "Gap solitons in elongated geometries: The one-dimensional gross-pitaevskii equation and beyond," Physical Review A **83**, 053610 (May 2011), `http://link.aps.org/doi/10.1103/PhysRevA.83.053610`

124

[90] H. Ott, J. Fortagh, G. Schlotterbeck, A. Grossmann, and C. Zimmermann, "Bose-einstein condensation in a surface microtrap," Physical Review Letters **87**, 230401 (Nov. 2001), `http://link.aps.org/doi/10.1103/PhysRevLett.87.230401`

[91] Scott Pratt, *Lecture Notes on Statistical Mechanics* (East Lansing, MI, USA, 2007)